UNIVERSITÀ DEGLI STUDI DI PAVIA

DOTTORATO IN SCIENZE CHIMICHE E FARMACEUTICHE E INNOVAZIONE INDUSTRIALE
(XXXIII Ciclo)
Coordinatore: Chiar.mo Prof. Piersandro Pallavicini

SYNTHESIS AND CHARACTERIZATION OF BULK NANOSTRUCTURED OXIDES FOR FUNCTIONAL APPLICATIONS

Tesi di Dottorato di
Angelica Baldini

AA. AA. 2017/2020

Tutor
Chiar.mo Prof. Umberto Anselmi Tamburini

ABSTRACT

The focus of this thesis is on the study of some oxides for functional applications presenting unique magnetic and transport properties. The work is divided in three parts, representing three different groups of functional materials that have been investigated: magnetic materials, low-temperature protonic conductors, and lithium-ion batteries cathodes. As for the magnetic materials, nanostructured sintered $CoFe_2O_4$ was investigated as a possible alternative to rare earth alloys for applications requiring hard magnets. The magnetic properties have been evaluated in the sintered samples presenting different microstructures, relative densities, and grain size. The low-temperature protonic conductors we investigated were TiO_2, CeO_2, and ZrO_2 doped with sulfur. It has been evidenced in the last few years that these simple oxides can present a significant low-temperature protonic conductivity when produced in bulk nanostructured form. The conductivity has been associated to surface phenomena taking place on the surface of the residual nanopores. In this study we evidenced as the doping with sulfur can enhance considerably the protonic conduction in some of these materials. It has been evidenced that sulfur-doped TiO_2 and ZrO_2 show excellent conductivity values, while instead in CeO_2 the doping with sulfur produce only minor changes in the transport properties. Finally new electrodic materials for Li-ion batteries have been investigated in the form of high-entropy oxides. A large number of compounds presenting the same crystal structure of $LiMn_2O_4$ but with the substitution on the Mn^{III} and Mn^{IV} sites have been produced. Different trivalent and tetravalent cations have been used to enter the spinel structure and lead to an enlargement of the spinel unit cell: Y^{3+}, Fe^{3+}, Al^{3+}, Cr^{3+}, In^{3+}, Ti^{4+}, Zr^{4+}, Tb^{4+}. Some interesting compounds, as $LiFe_{0.6}Ti_{0.6}Mn_{0.8}O_4$, $LiFe_{0.7}Mn_{0.6}Ti_{0.7}O_4$, $LiFe_{0.5}Mn_{0.5}TiO_4$, and $LiFe_{0.5}Ti_{0.5}MnO_4$ were identified and characterized for their electrochemical properties.

Summary

1. Introduction

Oxides are ceramic materials that have been used since antiquity due to their multiple structural and functional properties. Oxide ceramic materials are currently used for many applications, such as in prostheses, as building materials, components of furnaces, and as functional and structural materials for automotive, aeronautics, and aerospace applications[1–4]. These applications take advantage of their high mechanical and chemical stability, high melting point, electric, optical, and magnetic properties[5].

This thesis is focused on the study of some nanostructured oxides developed for functional applications[6].

When materials are in nanometric form, their physical and chemical properties are different when compared to their micrometric counterpart[7,8]. This happens because of the increase in the surface to volume ratio and of the quantum confinement. With the decrease of the particle size, the ratio between their superficial area and their volume increases. When the dimensions are nanometric, this ratio becomes very high. As a result, a substantial part of the atoms results in being near the surface. The atoms on the surface behave differently from the atoms in bulk and present higher energy. In general terms, a nanometric material is less stable than the same material in bulk form because it presents an excess free energy contribution deriving from the surface, which is not negligible.

The quantum confinement effects begin to appear when the nanostructure's dimension is comparable to the intrinsic wavelength λ of the electrons. In this condition, discrete and quantized values of energies emerge. For these reasons in nanometric materials most optical, electrical, and magnetic properties are different than in bulk materials.

The focus of this thesis will be on the transport and magnetics properties of some bulk nanostructured oxides. In fact this project has the goal to study nanostructured oxides with three types of functional properties:

- Magnetic properties

- Protonic conduction properties

- Lithium intercalation properties.

1.1 Magnetic properties of nanomaterials

The magnetism in matters depends in the motion of the charge particles, so the magnetic properties of materials can be attributed to the current produced by the electrons which are inside them; the electrons move around the nucleus with an orbital motion and around themselves with a spin movement. There are also other contributions which are usually negligible, as the one linked to the nuclear magnetic moment due to the movement of protons and neutrons[9].

When a material is immersed in an external magnetic field $\vec{H}$, it can react in different ways, the overall answer of the material can be described with the magnetic induction $\vec{B}$:

$$\vec{B} = \mu_0\left(\vec{H} + \vec{M}\right)$$

this is the formula with the International System unit of measures where $\vec{B}$ is the magnetic induction (T), $\vec{H}$ is the external magnetic field $(\frac{A}{m})$, $\vec{M}$ is the magnetization $(\frac{A}{m})$ which is the sum of all the magnetic moment vectors for unit of volume in the material and μ_0 is the magnetic permeability of vacuum ($4\pi\times10^{-7}$ T m A^{-1}). A material possesses different magnetic properties and a different answer to a magnetic external field, depending on its electronic structure. The type of answer can be evaluated with the values of χ, the magnetic susceptibility, which is a dimensionless constant that indicates the degree of magnetization of a material in response to an

applied magnetic field, and is the derivative of the magnetization in function of the external magnetic field at with zero external magnetic field.

The values of χ defines the classification of materials in diamagnetic, paramagnetic, ferromagnetic, antiferromagnetic and ferrimagnetic.

In diamagnetism and paramagnetism the magnetization is induced by the external magnetic field and it turns off when the external magnetic field is extinguished; in ferromagnetism, antiferromagnetism and ferrimagnetism the magnetization is permanent and remains on the material also when the external magnetic field, used to generated it, is switched off[10].

Diamagnetic materials have all the electrons paired and so have a zero total magnetization; when they are immersed in an external magnetic field, they are weakly rejected from it because inside them a very small magnetic field is generated in the opposite direction. The magnetic susceptibility χ of these materials is negative, with an order of magnitude in the range 10^{-6}-10^{-3} and does not change with the variation of temperature.

Paramagnetic materials contain unpaired electrons, which provokes the generation of magnetic moments not interacting with each other; these magnetic moments are oriented in a disordered way when there is not an external magnetic field, instead when they are immersed in a magnetic field, the magnetic moments orient themselves in the direction of the field, so a no zero magnetization is induced. This one is cancelled in the same moment in which the external field is removed. The magnetic susceptibility χ of these materials is positive, whit a value with an order of magnitude in the range 10^{-6}-10^{-1}, and inversely proportional to the temperature. With the increasing of the temperature the magnetic susceptibility decreases because the thermal motions tend to a disordered orientation of the magnetic moments.

The materials commonly defined "magnetic" are the ones with a permanent magnetization also in the absence of an external magnetic field. These are the materials which have a ferromagnetic,

antiferromagnetic and ferrimagnetic behavior. These properties appear when the magnetic moments inside the matter are not independent from each other but interact.

In antiferromagnetic materials there is an antiparallel alignment of the magnetic moments; there are two sublattices oriented in an opposite direction each other. In absence of an external magnetic field, the values of the magnetic moments are subtracted and the total magnetization is zero. This behavior appears under a critic temperature, called Néel temperature, while at higher temperatures the vibrational motion of the thermal agitations opposes to the alignment of the moments and there is the passage to a paramagnetic regime.

Ferromagnetic materials have unpaired electrons and are characterized by an high and positive value of magnetic susceptibility χ. They present magnetic moments aligned in the same direction; the direction is defined from the external field used to generate the magnetization. When the external field is removed, regions, called Weiss domains are formed. In each of these regions the magnetic moments are oriented in the same direction. When the ferromagnetic material is inserted in a magnetic field, the magnetic moments of the domains align along the direction of the applied field, so a magnetic moment different from zero is formed. A remanent magnetization remains also when the field is removed. The ferromagnetism behavior appears only under a critic temperature, which is typical of each material, called Curie temperature; over this temperature the materials have a paramagnetic behavior.

Ferrimagnetic materials are a particular case of antiferromagnetism, in which the two sublattices oriented in the opposite direction have different values of magnetic moments, one is higher and one smaller, so is present a net magnetic moment, different from zero. This magnetic moment confers to these materials a macroscopic behavior similar to ferromagnetism. Ferrimagnetism, as in ferromagnetic materials, appears under the Curie temperature, over this temperature there is a paramagnetic regime. Ferromagnetic and ferrimagnetic materials have a non-linear trend of

magnetization M in function of the external field H, described for the hysteresis cycle, which characterized magnetic materials[9].

Nanostructured magnetic materials show magnetic properties that are different from the one of the same materials in bulk form[11]. In fact, it is observed that the magnetic moment for one atom and the magnetic anisotropy of the nanoparticles can be significantly different from the values found in the micrometric form. Other magnetic properties are also modified when a material passes in the nanoscale regime, as the Curie and Néel temperature or the coercive field.

In a magnetic material a region in which there is a uniform magnetization is defined "domain". In particular, the term "Weiss domain" indicate a region where the magnetic moments of the atoms are aligned as shown in *Figure 1.* These magnetic domains arise from the balance between different energetic terms: exchange energy, magnetocrystalline anisotropy and magnetostatics dipolar energy. The exchange energy depends on the distance between the atoms and drops exponentially when the distance increase. It can promote both the parallel and antiparallel spin configuration, depending on the parameter **J**, which can be positive (parallel spin) or negative (antiparallel spin). The magnetostatics interaction is a dipolar interaction and decreases with the distance as **r³**, where r is the distance between the two magnetic moments.

The magnetocrystalline anisotropy results from the coupling of the spin and the orbital moment of the electrons. The directional properties of the electronic orbit are linked with the crystal structure, so the easily magnetized axes are in close contact with it. The exchange interaction tries to align the magnetic moments along the same direction, the magnetocrystalline anisotropy tends to direct them along specific direction and the magnetostatics interaction pushes towards the elimination of the magnetization of the material. Inside each domain the magnetic moments are aligned in the same direction providing to the domains a discrete magnetization different from a

domain to another one, so the total magnetization of the material is the sum of each domain magnetization considering the different orientations.

Between different domains there are zones called "domain walls" or "Bloch walls", which can be considered transition zones and have a finite thickness; in these zones the orientation of the magnetization varies gradually from that of one domain to that of the second one, as is shown in *Figure 2*[12]. The domain walls have a thickness in the nanometric range.

When the particles size presents a dimension that comparable or smaller than the size of the magnetic domains the formation of the domains structure is not energetically favored anymore and another regime, called single domain regime, becomes dominant. In this regime each nanoparticle presents a uniform magnetic moment, represented in *Figure 3* with a value corresponding to the sum of all the magnetic moments of the atoms inside it[13]. This happens because the formation energy of the Bloch walls increases when the interfacial areas of the domains rise. Each material has a characteristic critic dimension below which it enters in the single domain regime. For example, for Fe_3O_4 and $CoFe_2O_4$ this dimension is about 128 nm[12]. In the single domain regime the inversion of the magnetic orientation cannot be produced by the spin's rotation in the Bloch walls, but by the coherent rotation of all the magnetic moments inside the nanoparticle.

These nanoparticles can present a superparamagnetic behavior, if the temperature is higher than a particular temperature, called blocking temperature, T_B. In the superparamagnetic state the magnetic moments of the particles float around the axis of easy magnetization, which is the privileged direction that the material orientates in presence of an external magnetic field. The direction of the axis of easy magnetization depends on the magnetic and crystal structure of the material. When a magnetic field is applied the nanoparticles which are in a superparamagnetic state show a very fast response to the field, without showing any residual magnetization and a coercivity. They behave like a single paramagnetic atom, with a very large spin. Below T_B, the thermal agitation

becomes small and cannot cause the fluctuations of the orientations of the nanoparticle's magnetic moments, which remain stationary in a particular orientation.

There are two factors which cause a large coercivity in the nanoparticles: the spins rotation instead of the movement of the domain walls and the shape anisotropy. The bigger is the latter the higher is the coercivity. In a spherical particle the coercivity results to be small. The shape anisotropy is important in the determination of the critic dimension below which there is the single domain regime; spherical particles have a critic diameter smaller than the particles with an anisotropic shape.

The magnetic applications in which nanoparticles can lead some advantages, such as magnetic storage, optical devices[14] and medical applications, requires to have bulk materials which possess nanoscaled properties[15]. So bulk nanostructured materials are studied in this work, this type of material have to be magnetically evaluated in a different way than nanoparticles. Nanoparticles are noninteracting systems and derive their unique magnetic properties strictly from the reduced size of the components, with no contribution from interparticle interactions. In the other hand bulk materials with nanoscale structure are materials in which a significant fraction of the sample volume is composed of grain boundaries and interfaces, so the magnetic properties in this case are dominated by interactions. The length scale of the interactions can have a width of many grains and is critically dependent on the character of the interphase[11,16].

1.2 Ionic transport properties of nanomaterials

The nanostructure can also produce significant modifications in the transport properties of ionic materials[17–23]. In fact, the transport properties of the polycrystalline ionic materials depend strongly on the density of grain boundary. In ionic materials the grain boundaries present a net charge, as in the external surfaces. This charge can interact with the charged material's point defects and modify

their distribution. As a result, the grain boundaries of ionic materials are characterized by the presence of a particular region, called space-charge region (SCR) that has a width between 5 and 10 nm, that is characterized by a different concentration of ions than in the bulk. When the grains size of a particle is similar to the SCR extensions, two different adjacent SCR regions can even overlap[19].

In the case of the protonic conductors we have been studying, the transport of protons does not involve the bulk of the particles but is confined to its surface. The adsorbed water partially dissociates and the protons can move from a water molecule to another. In this situation the observed protonic conductivity is associated to the presence of open nanoporosity in the material[24,25].

Nanostructure can also influence the transport properties of the materials used as cathodes in lithium batteries. Recently the interest towards the substitution of bulk materials with the nanomaterials in Li-ion cathodes has grown considerably in the attempt of improving the performance of lithium rechargeable batteries[26–28]. Nanosized materials can provide large Li-ion exchange area and short Li-diffusion paths. The reduction of the diffusion paths permits to facilitate a fast lithium insertion and extraction reactions, this results in an enhancement in the battery's performance. Moreover, some studies have demonstrated that nanosized materials can also increase the cyclic stability of the batteries electrodes[29–32]. This is due to different reasons. Small particles can better arrange the structural changes that occurs when the lithium ions are inserted and extracted from the electrodes during the cycling process. Furthermore, smaller particles presenting larger specific surface can better accommodate the charge that accumulate at the surface or in a region very near the surface, increasing the charge and discharge rate of the electrodes.

The thesis is divided in three parts according to the three principal arguments of the work:

- Magnetic oxides

- Protonic conductors

- High-entropy oxides.

2. Techniques and apparatuses

2.1 Planetary mill

The ball miller used in this project is a FRITSCH Premium line P7.

The planetary milling, or ball milling, is a technique that allows the grinding, the disaggregation, and the homogeneity of a powder; It can be also used to break the grains and to make a solid-state reaction. The functioning of the miller is based on the vigorous transfer of energy through collisions caused by the double rotation of the container (grinding jar) in which the powder is inserted, around itself and on an orbit around the center of the instruments, as exemplified in *Figure 4*. In the jar there are spheres, which through these rotations bump into the sample and transfer to it their energy. This process allows to break the grains or to mix the powders leading to homogeneity and favoring the contact of the surfaces.

The jars and the spheres are usually made of hard material, in this work were used two type of materials, WC and YSZ.

The instrument allows to choose the rotation speed (rpm), the time of the grinding (min), the number of cycles and the duration of the pause between the cycles (min).

In the mill two identical jars must been inserted on the rotating disk in diametrically opposite position. In one jar is placed the sample, on the other an equal quantity of silicon dioxide powder. The spheres must be inserted into the jars in equal quantity. Generally the ratio of weights between the sample and the spheres lays between 1:10 and 1:20 (weight of the sample/ weight of the spheres). At the end of the treatment is necessary to do one or more cleaning cycles, using SiO_2 in all the two jars, in order to eliminate the sample's residue.

2.2 HP-FAST

Sintering is an heat treatment that turn a powder material into a solid one. It is an ancient technique used to create solid object of both ceramic and metallic materials for thousands of years. Traditionally, ceramic powders are sintered by means of long thermal treatments carried out at high temperatures. Operatively the powder is initially inserted into a mold, then pressed and transferred in an oven; in this way the grains of the powder enter in contact each other and the material densify, diminishing its porosity through the diffusion promoted by the temperature, as exemplified in *Figure 5.* In *Figure 6* the sintering steps are represented, initially the separated particles enter in contact among each other across the grain boundaries, then these merge thanks to the diffusion of the ions on the surface and create necks between the different grains, these remains compacted and irreversibly united. This kind of approach is not suitable for the realization of bulk nanostructured materials as the diffusion mechanisms and the high temperature needed for sintering lead also to a significant grain growth, that often result in the loss of the nanostructure. An effective strategy for maintaining the nanostructure even in high density materials has been the use of a technique called High Pressure-Field Assisted Sintering (*HP-FAST*), also referred as Spark Plasma Sintering. HP-FAST permit to maintain the nanostructure of the powder thanks to the high heating rates (up to 1000 $\frac{°C}{min}$), and to very high uniaxial pressure (up to GPa); these features permit to perform the sintering process in few minutes and at lower temperature than in the classical methods. The fast warming-up promotes the diffusion mechanisms and allows to obtain the densification retaining the nanometric grains of the starting nanopowder[33].

The sample container (die) used in this type of instrumentation are in graphite that are warmed-up by joule effect through the passage in the graphite of a current at very high intensity (up to 5000 A).

This technique is also known as Spark Plasma Sintering, this denomination is due to an initial theory according to which the mechanism at the base of the process involves the formation of sparks and electrical discharges, forming a plasma, between the point of contact of the powder's grains. This theory has never been confirmed. Other possible mechanism have been proposed, that consider phenomena like electromigration, diffusion induced by the presence of an electric field, temperature gradients, high heating rates, pressures gradient, stress and modification in the concentrations of defects[33].

The *Figure 7* shows a typical set-up for a HP-FAST apparatus, consisting of an uniaxial vertical press inserted in a vacuum chamber and connected to two electrodes, which provide the passage of the current. When a high-pressure densification is required, the sample is placed into a graphite double-stage die. In this case the two punches of the high-pressure section of the die are made by SiC. The samples realized are cylinders of different diameters (5 mm, 10 mm, 15 mm). The double-stage press is inserted into the vacuum chamber between two cylinders of graphite, which are in direct contact with the copper electrodes. Into the chamber must be created a vacuum of ~1 torr and then the uniaxial pressure is applied, and the warm-up is started. The chamber is linked to a water-cooling system.

During the sintering process an acquisition system, USB 2048 of Measurement and Computing, monitors allow to monitor pressure, temperature, voltage, current intensity, and the displacement of the pistons. The software presents the trend of these quantities in graphs in function of the time. In *Figure 8* there are these graphs of a typical sintering process.

The temperature is measured through a K-type thermocouple inserted in a hole in the lateral wall of the graphite die.

2.3 Density measurements

The relative and the absolute densities of the samples was calculated using the Archimedes' method. The measure is performed by weighing a sintered sample both in air and immersed into a solvent of known density, in this case the solvent is EtOH. *Figure 9* shows the instrumental apparatus used for these measurements. The bulk density of the samples could be calculated according to the following equations:

$$\rho_{A=\frac{m_D \cdot \rho_S}{m_D - m_W}} \qquad\qquad\qquad (2\text{-}1)$$

$$\rho_{R=\frac{\rho_A \cdot 100}{\rho_T}} \qquad\qquad\qquad (2\text{-}2)$$

where ρ_A is the absolute density of the sample, ρ_R is the relative density, m_D is the weight of the sample in absent of solvent (air), m_W is the weight of the sample immersed in the solvent, ρ_T the theoretical density of the compound and ρ_S the density of the solvent. The difference between the dry and the wet masses is equal to the mass of the solvent displaced from the sample, so the volume of the sample can be obtained using this mass and the density of the solvent (ρ_S=0.789 g/cm^3). Then the absolute density can be calculated by dividing the dry mass for the volume, while the relative density can be obtained from the ratio between the absolute density and the theoretical density of the material.

2.4 X-Ray Diffraction

The crystallographic composition of the samples was analyzed by powder X-ray diffraction.

The technique is based on the interaction between X-ray and the sample, in particular on the interference of the reflected rays of the crystallographic plane's families. X-rays possess

wavelengths with the same order of magnitude of the interplanar distances of the crystals, so they can interact with them and give information regarding the crystal structure of the analyzed material. The interactions between radiation and matter exploited in this case is the coherent scattering.

The diffraction phenomenon is based on the Bragg's law; when a X-rays beam hit with an incident angle θ on a crystallographic planes family, it is elastically scattered with a reflection angle equal to the incident angle θ, this is graphically explicated in the *Figure 10*. The X-rays reflected both by the different planes and in different point of the same plane interfere between themselves; the interference can be of two type, constructive or destructive; the waves sum up each other if there is constructive interference, and this happens if the difference between the optical paths of the different rays is equal to a multiple of the wavelengths of the rays. The difference between two optical paths of two parallel rays, which hit on two parallel planes of the same family, is equal to the sin of the incident angle multiplied by the double distance between the planes, from here derives the Bragg's law, reported in the following equation:

$$n\lambda = 2dsen\theta \qquad (2\text{-}3)$$

where **n** is the interference order, **λ** the X-rays wavelengths used, **d** is the interplanar distance and **θ** the incident angle.

The profile of diffraction is a graph with the intensity of the reflected rays on the ordinate axis and 2θ (°) on the abscissa axis. Is possible to calculate the interplanar distances d of the different planes' family from the positions of the peaks, knowing the wavelength, which is monochromatic and depends on the source used. With the different interplanar distances calculated is possible to obtain all the planes family and then the crystal structure of the sample. The intensity of the peaks is due also to the structure factor, that depends on a lot of parameters, as the scattering factor of

the atoms in the elementary cell, and this is linked to their atomic number. Also the lattice constants and the crystallite size can be obtained from the diffraction profile.

The diffractometer used in this work is a Bruker D8, with a Bragg-Brentano geometry; the source and the detector are positioned at the same angle with respect to the sample, and during all the measure they move of the same angle. The source, the detector and the sample are on the same circumference, Rowland circle. The measure is made, taking all the diffracted rays at the same incident angle with the variation of the angle. The source is a Coolidge tube with a copper cathode, which emit x-rays with λ equal to the K_α of Cu (1.54 Å) and the detector is a scintillation one. After the source there is a monochromator and a slit to narrow the beam, a slit is also inserted before the detector.

The diffraction patterns of the sample were analyzed with the software High Score Plus (PANanalytical). The crystallite size of the samples was calculated trough the full width at half maximum, FMWH, using the Scherrer's equation:

$$d \; = \frac{k\lambda}{\beta_{corr}cos\theta}$$

(2-4)

where d is the dimension of grains, k is a geometrical factor (equal to 0.89 for the spherical particles), λ is the wavelength of the incident radiation, β_{corr} is the full width at half maximum corrected with the instrumental widening and θ is the incident angle in radians.

2.5 Scanning electron microscopy

The scanning electron microscopy (SEM) was used to evaluate the microstructure of the samples and their composition through energy dispersion spectroscopy (EDS).

The SEM is based on the interaction of a primary high energy electron beam with the surface of a solid. The signals evaluated are secondary electrons, which give an image of the microstructure of the sample, the backscattered electrons, which provide an electron density map of the elements in the materials, and X-rays, which give a qualitative and quantitative information of the composition of the sample. When the electrons hit the sample, they interact and can be elastically diffused (backscattered electrons) or can let out the electrons in the external orbitals of the hit atoms (secondary electrons). Both signals can be used to produce an image.

Using the secondary electrons it is possible to obtain an image with high resolution and great depth of field. Fluorescence X-rays are produced because the electron beam can remove electrons from the core atomic levels. The energy of the core levels is characteristic of each element, so analyzing the energy of the x-rays emitted by the sample is possible to evaluate its composition, in qualitative e quantitative way. The X-ray can be detected in two different modes: the EDS, energy dispersive spectroscopy, or WDS, wavelength dispersive spectroscopy.

The SEM characterization was conducted at the "Centro Interdipartimentale di Studi e Ricerche per la Conservazione del Patrimonio Culturale (CISRiC)" in Pavia, using a SEM TESCAN Mira 3 XMU, which is showed in *Figure 11*; this microscope has a field emission source with LaB_6 point.

The sample have been prepared in different ways; the powders have been positioned directly on the stubs using a graphite adhesive tape. The sintered samples have been analyzed on fracture surface or on polished sections. In the last case the samples have been first incorporated in epoxy resin and then grinded and polished using abrasive papers with decreasing granulometry (from P320 to P4000) with a polishing machine Buehler Phoenix Alpha with a rotor shaft allowing the polishing of four samples at the same time. All the samples have been coated with a conductive layer of C using a Sputter Cressington Coater HE 208 at CISRiC; the graphite is deposited with a technique of

direct evaporation in vacuum. The grain sizes of the samples were determined using the software imageJ.

2.6 Magnetic measurements

In order to measure the magnetic properties of a material is necessary to evaluate its magnetic response when inserted in an external magnetic field. This response can be determined using different techniques. The instruments allowing measure the magnetic properties of a material (magnetometers) and can be classified as AC type or DC type. The AC magnetometer are based on field which vary rapidly in time, instead DC magnetometer are based on static field.

The instrument used for the magnetic characterization of our samples is a Physical Property Measurement System (PPMS) of Quantum Design Inc. The measurements have been performed at the Laboratory of Molecular Magnetism LAMM of the Chemistry Department "Ugo Schiff" at University of Florence. This instrument work under direct current[34]. The PPMS is an automated cryomagnetic system allowing the characterization of several properties of the materials, such as susceptibility, magnetization, thermal and electric transport. For the magnetization measurements a vibrating sample magnetometer (VSM) has been set on the PPMS in order to give it a DC magnetometer function. The instrument's functioning is based on the Faraday's law principle, which states that in a closed circuit, under a flux of an oscillating magnetic field, a current flow is generated.

To perform the measure the sample has been placed in an homogeneous magnetic field, which is produced by superconducting coils. When the material is inserted in the field, a magnetic field flux is induced, which is proportional to the magnetic moment of the sample. This flux can be measured from the current induced in a detection coil.

In a common magnetometer the sample is inserted in a liquid helium cryostat. The measure chamber and the helium bath are linked by a thin capillary. Near the sample there is a heating element and the temperature is controlled during the measure. It is possible to perform

measurements in a range of temperature between 1.9K and room temperature. The helium bath

has also the function to maintain the superconducting magnets and measuring device at the right

temperature. The temperature is monitored by two GaAs diode sensors, one near the sample and

another near the heating element. These sensors allow to measure temperature variations of 0.001

K. With this instrument is possible to perform two types of measurements:

- The dependence of magnetization from temperature M(T),

- The dependence of magnetization from the field intensity, in order to obtain the
  hysteresis loop M(H);

To perform the measures of M(H) the sample is brought at the desired temperature, then is

magnetically saturated with a positive magnetic field (50 kOe). The magnetization is measured while

the field decreases until the negative opposite saturation (-50 kOe). At this point the magnetization

is measured again with the increasing of the magnetic field in the positive sense. This process can

be done at room temperature and at lower temperatures. From the shape and dimension of the

hysteresis loop is then possible to obtain the magnetic properties of the analyzed samples, as the

coercive field H_c, the remanent magnetization M_r and the saturation magnetization M_s. In these

experiments the magnetic moment of the sample is measured in **emu**, so the magnetization in $\frac{emu}{g}$

is obtained dividing this number for the sample mass. The values are then corrected using a factor

which depends on the shape of the examined sample. The value that is corrected is the external

field H_{ext}, at which is subtracted the demagnetization field produced by the sample during the

measures. This field varies during the measure and with the dimension of the sample. The equation

for the correction is:

$$H_{corr} = H_{ext} - 4\pi 0.68M \qquad\qquad (2\text{-}5)$$

Where **M** is the magnetic moment for volume unit ($\frac{emu}{cm^3}$) and **0.68** is the demagnetization factor associated to a cylinder of 5 mm of diameter and 1 mm of height[35], which are the dimension of the sintered samples on that the measure have been made. In the hysteresis cycles reported in the thesis the values of field H are corrected using this equation.

2.7 Electrical measurments

2.7.1 Impedance spectroscopy

The electrical conductivities, σ, of the sintered samples were determined by means of impedance spectroscopy using a Frequency Response Analyzer Solartron Schlumberger 1255.

Impedance spectroscopy allows to investigate different conduction processes and measures the response of an electrochemical system when it is subjected to the application of a low-intensity alternate signal (a current or a potential) in the range of frequencies between 0.1 and 10^6 Hz. The measured quantity is the impedance Z, which is the alternate current equivalent of the electrical resistance and, analogously to the Ohm's law for direct current circuits, it is defined by the ratio between the time-dependent voltage, *V(t)*, and current, *I(t)*:

$$Z = \frac{V(t)}{I(t)} \qquad\qquad (2\text{-}6)$$

The impedance is a complex number with a real and a complex part: $Z = Z' + Z'' = R + iX$

$$Z = Z' + Z'' = R + iX \qquad\qquad (2\text{-}7)$$

where **Z'** is the real and **Z"** the complex contribution to the total impedance; **Z'** corresponds to the resistance **R** and **Z"** to *i* times the admittance **X**. For electrochemical applications the impedance data are generally reported as in *Figure 12*, plotting the total impedance in a **Z'** vs **Z"** chart at different frequencies. This type of graph is called Nyquist plot. The response of the electrochemical systems can be modeled using equivalent electrical circuits, including different discrete elements, such as resistances, capacitors and inductances. A circuit including a resistance **R** with a capacitors **C** in parallel presents a Nyquist plot characterized by a single semicircle. The intercept of the semicircle with the X-axes correspond to the values of the resistance **R** and from the maximum of the graphs the value of the capacity **C** can be obtained with the formula:

$$C = \frac{1}{\omega_{max} \cdot R} \qquad\qquad (2\text{-}8)$$

where ω_{max} is the frequency corresponding to the maximum of the graph.

There are also other types of presentations, which can be obtained with the data deriving from the impedance measure. One of the most common is represented by the so-called Bode plots, that present two chart with the frequency **ω (Hz)** on the abscissa and the impedance module $|Z|$ and phase angle **θ** on ordinate. The Nyquist graphs have been used in this work in order to obtain the values of resistance **R** of the samples. As mentioned before, this is obtained from the high intercept of the semi-circular fit with the abscissa of the graph. From the resistance **R** it is possible to calculate the conductivity **σ** $(\frac{S}{cm})$ using the following equations:

$$\sigma = \frac{1}{\rho} \qquad\qquad\qquad (2\text{-}9)$$

$$\rho = \frac{R}{k} \qquad\qquad\qquad (2\text{-}10)$$

$$k = \frac{l}{A} \qquad\qquad\qquad (2\text{-}11)$$

where **k** is the cell constant, **A** the superficial area of the sample, l the height of the sample, and **ρ** the resistivity. The measures are made on sintered samples, which are previously sputtered on the two faces with platinum using a sputter coater from W.Pabish SpA.

The samples of the chapter Protonic Conductors (section 4) are then placed between two mesh platinum electrodes in the cell schematized in *Figure 13.* The cell includes a thermocouple to measure the sample temperature. The cell is inserted in an apparatus (Fuel Cell Testing Stand described in the following section 2.7.2) that allows to do perform conductivity measurements in an atmosphere of controlled relative humidity at different temperatures. The measurements are made using a voltage of 100 mV in a range of frequency between 0.1 and 10^6 Hz and of relative humidity between 10 and 100 % at 80 °C.

The samples of the chapter High-entropy oxides (section 5) are measured in a two electrodes cell, with platinum electrodes, that can be inserted in a furnace in order to do measurement at different temperature values. The samples are measured between 25 °C and 300 °C using a voltage of 150 mV in a range of frequency between 0.01 and $5 \cdot 10^5$ Hz.

2.7.2 Fuel Cell Testing Stand

The instrument allows to perform electrochemical measurements at different values of temperature and relative humidity. The electrochemical cell is placed between two graphite plates which allow the heating of the cell. The cell is pressed between the two plates and allowing a

nitrogen flux that, before to enter in the cell, passes in a water saturator. The container is heated in order to obtain controlled values of relative humidity. These values are calculated from the software, which controls the instrument, on the base of the difference of temperature between the water saturator and the internal of the cell. A schematic illustration of the instruments is represented in *Figure 14*.

3.   Magnetic oxides

3.1 Introduction

Hard magnetic materials are a key component in a large number of relevant technological applications. The best hard magnetic properties are presented by Fe-based alloys, such as ALNICO[36], or rare earth alloys containing neodymium or samarium[37–39]. However, the limited availability and the rising cost of rare earth metals[40], together with their chemical instability and low resistance to corrosion, has recently fueled the interest towards alternative magnetic materials. Ceramic oxides represent an attractive alternative, as they do not suffer from oxidation or corrosion, are widely available, inexpensive, and environmentally friendly. However, the magnetic properties in magnetic oxides are still substantially inferior to that of magnetic alloys. On the other hand, it has been recently shown that the nanostructure can alter significantly the magnetic properties of these oxides[6,7,41,42]. Magnetization, magnetic anisotropy, Curie, Néel temperatures and the coercive field can be drastically modified in nanostructured material[10,43]. The unusual magnetic properties exhibited by ferrites nanoparticles (NP) have spurred a large scientific interest over the last few years[44,45]. Ferrites are compounds with a spinel crystal structure and general formula AB_2O_4 , with *A* being a divalent cation and *B Fe(III)*[46,47]. If compared to their micrometric counterpart, nanometric ferrites possess unusual saturation magnetization and higher coercive field[48,49]. Nanometric ferrites may also exhibit superparamagnetic behavior[43]. The modifications of the magnetic properties associated to the nanostructure have been well characterized in nanoparticles or nanocrystals[50–57]. However, most technological applications require materials in bulk form. For this reason, the production of materials deriving from the sintering of nanopowders and retaining their magnetic properties would be highly desirable. Despite that, the number of reports on ferrite bulk nanostructured materials are still quite limited[58–62]. The main challenge for the realization of these

materials is represented by the control of grain growth during the sintering process. However, the recent introduction of innovative fast sintering methods, such as Field Assisted Sintering (FAST) or Spark Plasma Sintering (SPS), allowing rapid sintering cycles, offered a possible solution[33,63,64]. In particular, the use of high pressures (up to 1 GPa) coupled with fast sintering cycles have demonstrated to be particularly effective in obtaining the densification of nanopowders, even when they are strongly agglomerated[65]. This last point is particularly relevant for the production of bulk magnetic oxides. Most of the methods used for the synthesis of ferrite nanomaterials are designed to produce high-quality, monodisperse nanopowders[50,66,67]. These methods, however, are generally expensive, time consuming and present very low yield. As such they do not represent an ideal source of nanopowders for the realization of materials in bulk form. On the other hand, simpler and high-yield methods, such as the Pechini method, produce badly agglomerated nanopowder that are generally considered not ideal for sintering.

The aim of this part of the thesis was to explore the possibility to prepare bulk nanostructured $CoFe_2O_4$ by high-pressure field assisted sintering (HP-FAST) starting from nanopowders produced using a simple, low-cost approach based on a modified Pechini synthesis and to characterize its magnetic properties. Different experimental conditions have been taken into consideration for the preparation of nanoparticles and the following densification. The magnetic properties of the produced materials have been evaluated and compared. Moreover, in order to study better the variation of the magnetic parameters with the relative density and the dependance from the microstructure, composites samples of cobalt ferrite with a diamagnetic material have been produces. The diamagnetic materials chosen is YSZ in form of nanopowder.

3.1.1 Cobalt ferrite

Ferrites has been discovered hundreds of years ago, the first compass contained the most famous ferrite: the magnetite, Fe_3O_4 [10]. Their general formula is MFe_2O_4, where M is a bivalent cation such as Fe^{2+}, Zn^{2+}, Co^{2+}, Mn^{2+}, Ni^{2+}, Mg^{2+}.

In the particular case of magnetite M is represented by Fe^{2+}, while in the cobalt ferrite M is Co^{2+}. Ferrites show the spinel crystal structure, that belongs to the *Fd-3m* space group. The unit cell is face-centered cubic and contains 56 atoms: 32 oxide anions distributed in a face-centered cubic structure, 24 cations distributed on 8 of the 64 available tetrahedral sites and 16 of the 32 available octahedral sites. The octahedral sites are larger than the tetrahedral ones. The lattice constant a is almost *8.4 Å* and varies with cation M [10,46]. When all the divalent cation stays on the tetrahedral sites and all the trivalent cation on the octahedral sites the structure is called direct spinel. This structured is represented in *Figure 15*. On the other hand, when all the divalent cations stay on the octahedral sites, while half of the trivalent cation stay on the tetrahedral sites and the other half on the octahedral sites, the structure is called inverse spinel, indicated by the formula $(B)[AB]O_4$. An intermediate situation is also observed, called partially inverse spinel, generally indicated using the following formula:

$$(M^{II}_{1-x}Fe^{III}_{x})[M^{II}_{x}Fe^{III}_{2-x}]O_4$$
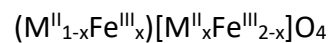
Where x is the degree of inversion of the spinel and represents the quantity of Fe^{3+} which stay on the tetrahedral sites. If x=1 the structure is an inverse spinel, if x=0 the structure is a direct spinel.

In general, in the ferrite structure the bivalent cations Fe^{2+}, Co^{2+}, Mn^{2+}, Ni^{2+}, Mg^{2+} prefer to occupy the octahedral sites because they are larger, while Zn^{2+} prefers the smaller tetragonal. In the ferrite structure all the cations on the octahedral sites have the magnetics moments oriented in the same

25

direction. The same happens on the tetrahedral sites but with an orientation that is antiparallel to that of the octahedral ones. The net magnetization of the spinel derives from the difference between the magnetic moments of the cations on the octahedral sites and the cations on the tetrahedral sites. All these cations possess magnetic moments because they are transition metals. The magnetic moment of a transition metal is mostly due to the magnetic moment of the spin of their 3d unpair electrons. In *Figure 16* the electronic disposition of the 3d electrons of the cations present in ferrites are reported. The exchange interaction between the cations on the two cationic sublattices has different values. Usually the exchange interaction between the sublattice A (divalent cation) and the sublattice B (trivalent cation) is larger (AB interaction) and is transferred through the anions which separate them. The interaction between the cations A (AA interactions) and between the cations B (BB interaction) is usually weaker [10].

$CoFe_2O_4$ is a partially inverse spinel with an inversion degree x=0.8, so the 80 % of the Co^{2+} cations are on the octahedral sites. Its unit cell is reported in *Figure 17* and its lattice parameters are reported in *Table 1*. $CoFe_2O_4$ is a material with a ferrimagnetic behavior. The ferrimagnets, like ferromagnets, present a net magnetization also without an external magnetic field but, unlike ferromagnets, have an alignment of the magnetic moments antiparallel not compensated; this happens because the antiparallel moments have different intensity and so there is a net spontaneous magnetization[68].

Cobalt ferrite is characterized by a high magneto-crystalline anisotropy, a high coercivity, a moderate residual magnetization, a good chemical stability, and a good mechanical resistance. These properties make cobalt ferrite a material useful for applications as magnetic memories, optical devices and medical instrumentations[59].

The magnetic properties of this material are due to the presence of Co^{2+} and Fe^{3+} in octahedral and tetrahedral sites. This disposition result in having the 3d orbitals with unpair electrons

producing magnetic moments on the corresponding atoms. In literature are reported a large number of studies dealing with the magnetic properties on $CoFe_2O_4$ nanoparticles. One of these studies, concerning nanoparticles on *15 mm* synthesized with *sol-gel* method, reports values of coercive field of *1215 Oe* at room temperature e *10.2 kOe* at *77 K*, with a remanent magnetization of 30.2 $\frac{emu}{g}$ at room temperature and 35 $\frac{emu}{g}$ at *77 K* [69]. Another study, based on nanoparticles of cobalt ferrite synthesized by co-precipitation with a grain size of *20 nm*, shows values of coercive field of *1205 Oe* and a remanent magnetization of 31.7 $\frac{emu}{g}$ at room temperature and *≈11 kOe* and

34.4 $\frac{emu}{g}$ at *77K.* [70].

In sintered samples the properties can change considerably because of the intimate contact between the nanoparticles. The effect of this interaction has been not much studied for the difficulty to obtain massive materials with an high relative density and a nanometric dimension of grains.

3.2 Experimental

3.2.1 Synthesis

Cobalt ferrite nanopowders have been synthesized using a modified sol-gel Pechini method. Soluble salts of the cations present in the final oxide have been used as precursors: $Fe(NO_3)_3 \cdot 9H_2O$ (Sigma-Aldrich ACS reagent Ph eur), $Co(NO_3)_2 \cdot 6H_2O$ (Sigma-Aldrich ACS reagent, ≥ 98 %) with cationic stoichiometry 2:1 and citric acid (Sigma-Aldrich 99%), with a molar ratio equal to 1.1 in respect to the sum of the cations, were dissolved in 60 mL of distilled water. Citric acid is added as cation complexant and gelification agent. The solution was kept under stirring at 80°C for 16 h, in order to allow for water to evaporation. A brown gel was formed. This gel was dried in a furnace at 120°C for 2 h, in order to eliminate the residual water and to start to degradation of the nitrates. Then, the gel was transferred into an alumina crucible and calcined at 600 °C for 1 h. During this calcination the nitrates and the organic components are degraded and the oxide is formed. The product is

represented by a strongly agglomerated black powder. The agglomeration is typical of this type of synthesis. In order to disaggregate this powder in some cases a mild milling treatment was performed using a FRITSCH Premium line P7 ball-miller with *WC* jars and balls. The jars were previously cleaned by milling 7 mL of SiO_2 powder at 400 rpm for 30 min.

3.2.1.1 Composites CoFe$_2$O$_4$-ZrO$_2$

To prepare composite between $CoFe_2O_4$ and the diamagnetic YSZ, the cobalt ferrite nanopowder synthesized as described in the section above, and commercial zirconium oxide nanopowder (TOSOH-ZIRCONIA TZ-3Y) have been mixed. The YSZ contains a 3% of Yttrium oxide and presents a tetragonal crystal structure and a grain size of 50 nm. In order to provide for a homogeneous mixing the two powders have been ball milled together at 400 rpm for 30 min with a ratio of 1:10 between the sample and the spheres of the miller. Different mixtures have been prepared, presenting a YSZ content between 1 and 10% (mol/mol) of YSZ:

- 1.5 % (mol/mol) YSZ/CoFe$_2$O$_4$

- 2 % (mol/mol) YSZ/CoFe$_2$O$_4$

- 5 % (mol/mol) YSZ/CoFe$_2$O$_4$

- 10 % (mol/mol) YSZ/CoFe$_2$O$_4$

3.2.2 Sintering

Bulk samples had been obtained sintering the nanopowders with an home-made high-pressure field assisted (HP-FAST) apparatus, showed in *Figure 7*. In order to achieve uniaxial pressures up to 1 GPa two-stage dies have been used[71]. In this setup an external die, where most of the current flows and the heat is generated, is made out of high-density graphite and include a second, internal high-pressure die, made out of *SiC* or *WC*. The combination of high pressures and high heating rates (*200*

$\frac{°C}{min}$) allows to achieve a high level of densification with a minimum of the grain growth. In a typical experiment *0.150 g* of nanopowders were placed in the double stage die with an internal diameter of 5 mm. The die was inserted in the HP-FAST apparatus and connected to a K-type thermocouple placed in its lateral wall. The HP-FAST chamber was evacuated to a pressure of *10 Pa*. Two different experimental procedure have been followed. In one case a moderate uniaxial pressure (*200 MPa*) was initially applied to the sample, the temperature was increased linearly with a heating rate of *200* $\frac{°C}{min}$ until the sample reached the designated temperature and the pressure was then rapidly increased to the final value (*400-600 MPa*). The sample was kept under these conditions for 5 min and the pressure was then quickly released, and the power turned off. The samples obtained using this procedure will be indicated in the following with the label SPS_1. In the second procedure all the pressure was applied at the beginning of the process and maintained throughout the sintering cycle. These samples will be indicated by the label SPS_2. Samples obtained through the procedure SPS_1 using milled powders will be indicated by the label SPS_1-m. In all cases the sintered samples were represented by discs of 5 mm in diameter and 1 mm thick.

3.2.2.1 Composites CoFe$_2$O4-ZrO$_2$

The composite powders prepared mixing cobalt ferrite with YSZ have been sintered at 575 °C and 600 MPa using the procedure SPS_1 in the 5 mm die.

3.3 Results

3.3.1 CoFe$_2$O$_4$ nanopowders

The nanopowders synthetized using the Pechini method were analyzed by X-ray diffraction and resulted always to be single phase CoFe$_2$O$_4$, as evidenced by the XRD reported in *Figure 19* which presents the typical peaks of the spinel structure. The particles size, as calculated from the XRD

patterns, were between 30 and 40 nm. This grain size was confirmed by SEM analysis. An image relative of these nanopowders are reported in *Figure 20*. The low-magnification SEM image of *Figure 20-b* evidences an extensive agglomeration. The level of agglomeration decreased considerably after ball milling, although the grain size and the phase composition remained unchanged, a comparation of the SEM images of the nanopowder before and after the milling process is reported in *Figure 21*.

The magnetic hysteresis loop relative to these nanopowders, as measured at room temperature, is reported in *Figure 24*, while a summary of their magnetic properties is reported in *Table 2*. The values are comparable to the one reported in literature for cobalt ferrite nanopowders obtained using various synthesis methods[61,69].

The $CoFe_2O_4$-YSZ composite nanopowders have been analyzed by SEM-EDS in order to control the effective content of YSZ in the cobalt ferrite. These results are reported in *Table 3*.

3.3.2 $CoFe_2O_4$ sintered samples

Sintered samples had been prepared using different combinations of temperature and pressures on nanopowders that underwent different milling treatments. The sintering process did not produce modifications in the phase composition of the material, that remained in all cases single phase cobalt ferrites, as shown in *Figure 19*. The dependence of the relative density from the sintering temperature is reported in *Figure 26*, when an uniaxial pressure of 500 MPa is used. In the case of unmilled nanopowders all samples sintered at *T >600 °C* present a relative density above *95 %*, reaching a maximum of *98 %* at *700 °C*. The density of samples sintered at higher temperatures could not be measured due to their brittleness. It must be noted that an uniaxial pressure of 500 MPa used for this material is well above the typical values used in SPS or FAST processes, but it is essential in order to obtain high relative density values, while maintaining the sintering temperature

low enough to avoid significant grain growth. The data in *Figure 27* confirms that even using very short sintering times (5 min) the grain size of the material increases rapidly with the sintering temperature. Milled nanopowders, presenting a reduced agglomeration, can be densified more efficiently, as shown by *Figure 26* , as full density can be achieved at temperatures just above 600°C using a pressure of 500 MPa. The optimal sintering conditions was identified to be at *T=575 °C* and *P=650 MPa*. Using these conditions the samples showed a high relative density (97%), while the grain size was still around 60 nm.

The microstructure of the sintered materials resulted to be quite complex and strongly dependent on the milling treatment and on the sintering experimental conditions. Bulk samples obtained from unmilled nanopowder using the procedure SPS_1 (two stages pressure cycle) presented a quite inhomogeneous microstructure. SEM-BS images of polished cross-sections show how the agglomeration present in the starting powder were retained in the sintered material (*Figure 28*). The images, in fact, show the presence of fully dense areas, micrometric in size, surrounded by regions presenting some residual nanoporosity. No macro or mesoporosity is observed. The introduction of a mild milling treatment improved considerably the microstructural homogeneity, as is possible to observe in *Figure 29*. The largest agglomerates are not present anymore, although higher magnifications images show the evidence of a residual agglomeration, sub-micrometric in size, together with some nanoporosity. Notably, the samples that underwent milling treatment always showed the presence of contamination from *WC,* deriving from the milling medium. Such contamination, evidenced as very bright spots in the SEM-BS images of *Figure 29*, could be reduced by decreasing time and energy associated to the milling treatment, but it could never be completely removed.

A more uniform microstructure could be obtained using the densification procedure SPS_2. In this case the maximum uniaxial pressure is applied at the beginning and is maintained throughout

the entire sintering cycle. In this way the agglomerates appeared to be drastically reduced, as they were effectively crushed in the early stages of the process, where plastic deformation was not possible. The microstructure of these samples is showed in *Figure 30*.

The magnetic properties of the more significative sintered samples of cobalt ferrite produced during this investigation are summarized in *Table 2*, while Figure 25 Hysteresis loop of the cobalt ferrite sintered samples SPS_1_575°C, SPS_2_575°C and SPS_1-m_575°C *Figure 25* shows the corresponding hysteresis loop measured at room temperature.

3.3.2.1 Composites CoFe$_2$O4-ZrO$_2$

All the sintered samples of CoFe$_2$O$_4$-YSZ present the cobalt ferrite phase in the XRD patterns (*Figure 22*). A small peak at about 50 ° (2θ), which belong to the ZrO$_2$ tetragonal crystal structure can be observed in the samples presenting the higher content of YSZ. The peak at about 30 ° (2θ), which is the most intense for the tetragonal zirconia phase it is not distinguishable because it falls al the same angle of a peak of cobalt ferrite. In the samples containing 1.5 % and 2 % of YSZ the peak at about 50 ° (2θ) is not visible because the quantity of this phase is too low to be detectable. The sintered sample's values of relative density are reported in Table 4. The relative density in this case is calculated as the density of cobalt ferrite in the sintering sample, subtracting the quantity of ZrO$_2$ present. As is possible to see from the data in Table 4 the relative density (%) decreases with the increasing of the quantity of ZrO$_2$, because the ZrO$_2$ particles occupy part of the sintering sample's volume.

From the SEM analysis of the samples is possible to calculate the grain size of cobalt ferrite nanograins, which result to be 50 (10) nm for all the samples. As an example, is reported a SEM image of one of the samples in *Figure 23*.

The magnetic properties of these composite samples are reported in Table 4.

3.4 Discussion

It must be first noted that all the sintered samples present hard ferromagnetic properties close to the one of the cobalt ferrite nanopowder. The hysteresis loops of the nanopowders and of a sintered samples are quite similar, as is possible see in *Figure 24* and *Figure 25*. In fact, the value of the saturation magnetization at 300 K for the powder was 71 $\frac{emu}{g}$, while for the sintered samples varied between 70 and 86 $\frac{emu}{g}$. The remanent magnetization for the nanopowder was 33,3 $\frac{emu}{g}$, and in the range 18-39 $\frac{emu}{g}$, for the sintered samples; while the coercive field at 300 K for the powder was 2134 Oe, while for the sintered samples was between 750 and 2150 Oe. Finally, the maximum energy product at 300 K for the powders was 6,0 $\frac{kJ}{m^3}$ and for the sintered varied in a range 3,7-8,2 $\frac{kJ}{m^3}$. It must also be noted that the values of the magnetic parameters we observed in our sintered samples were in most cases superior then the values reported in the literature for densified ferrite materials[26–30,37,42,43]. A comparation between the sample produced in this work and the ones reported in the literature is summarized in

Table 5. Particularly relevant is the considerable higher values in coercive field we observed in our case.

However, samples with different microstructures present significant differences in magnetic properties. Surprisingly, a uniform microstructure does not seem to be very relevant from this point of view. In fact, samples obtained using the procedure SPS_2 (see *Table 2*), that are characterized by a very homogeneous microstructure, present values of the magnetic properties that are similar to the one presented by the sample SPS_1, presenting a comparable relative density and grain size, but showing a very inhomogeneous microstructure, characterized by the presence of large agglomerates. The sample SPS_1-m shows the best magnetic properties, particularly regarding the coercive field, although the material presents a significant agglomeration and also contains some

contamination from the milling media. Evidently the materials obtained using the procedure SPS_1-m present an optimal microstructure, presenting an ideal combination of grain size, relative density and separation between the grains[44,45]. Some further indication about the role of microstructure in defining the magnetic properties of these oxides can obtained from the data in *Figure 31*. In these figures the trend of coercive field and saturation magnetizations for the material presenting the best overall combination of magnetic properties (SPS_1-m) are reported as a function of the sintering temperature in the range 550-700 °C. It is evident as the coercive field and the magnetization present an opposite behavior. The coercive field, in fact, shows a significant decrease, and reduces its value to almost half when the sintering temperature goes from 550 to 700°C. The magnetization, on the other hand, shows a slight increase in the same temperature range. It must be noted that the increase in the sintering temperature produce an increase in both grain size and in the relative density of the materials, as shown previously in *Figure 26* and *Figure 27*.

In order to understand better the role exerted by the microstructure in the definition of the magnetic properties of the composites materials $CoFe_2O_4$-YSZ have been characterized. In *Figure 32* and *Figure 33* are reported the trend of the saturation magnetization M_s and coercive field H_c in function of the YSZ/$CoFe_2O_4$ ratio. It is possible to see that while the saturation magnetization shows a decreasing trend with the increase of the YSZ content, the coercive field increases with the YSZ content. The increase in the YSZ/$CoFe_2O_4$ ratio reduces the amount of cobalt ferrite present in the samples, but also the magnetic interaction between the grains.

In order to clarify the contributions deriving from the grain size and the relative density in the sintered samples, the dependence of coercive field and magnetization from these two parameters have been reported in the tridimensional graphs of *Figure 34* for all the sintered samples produced in this investigation, regardless the status of agglomeration of the starting powders. Despite some spreading in the data it appears quite evident as the extent of the coercive field

depends largely on the relative density, as already evidence in *Figure 34*, but shows a limited dependence from the grain size, at least within the range of values considered in this investigation. In particular, the coercive field is higher when the relative density has lower values. In facts it shows the maximum values for not fully dense samples but when the density is in the range 80-90%. The coercive filed is higher also with lower values of grain size. The behavior of the magnetization appears to be more complex. Fully dense materials, in fact, present the highest values for this parameter, but a significant dependence from the grain size is also observed.

3.5 Conclusions

High-pressure field assisted sintering allows obtaining almost fully dense nanostructured cobalt ferrite even when the starting nanopowders are obtained by solution chemistry and present a significant level of agglomeration. The use of very high uniaxial pressures, up to 600 MPa, produces a significant plastic deformation of the agglomerates, removing all macro and mesoporosity even using relatively low sintering temperatures and sintering times reduced to few minutes. The magnetic properties presented by the starting nanopowders are almost completely retained in the bulk samples when a mild milling treatment is used. Although it is confirmed, in agreement with previous findings, that the presence of large agglomerates reduces the magnetic properties of the bulk material, it resulted also evident that some level of heterogeneity in the microstructure seem to help maintaining these magnetic properties of the starting nanopowders. The results also evidenced a significant dependence of the magnetic properties from the relative density of the bulk material. This dependence appears to be particularly relevant for the coercive field, that increase drastically reducing the relative density of the material. It is well known that the densification process introduces a strong interaction between the grains, that is largely absent in the individual NP. However, the understanding of the role of these interactions in defining the magnetic

characteristics of the sintered material is still largely a work in progress [26–30], particularly in the case of materials present complex microstructures deriving from agglomerated nanopowders.

4. Protonic conductors

4.1 Introduction

Protonic conductors are solid materials that present the ability to transport of protons behaving like electrolytes in which the cation H^+ can move. They are generally polymers or oxides.

Low-temperature protonic conductors represent a key component in electrochemical applications such as fuel cells and water electrolyzers. These devices play an important role in the development of sustainable way for the production of energy. Fuel cells allow the production of electric power through the reaction between H_2 as fuel and O_2/air as oxidizing, producing only water as the only by-product. In fuel cells at the anode is realized the oxidation of hydrogen, according to the reaction:

$$H_2 \rightarrow 2H^+ + 2e^- \qquad (4-1)$$

while at the cathode compartment there is the reduction of oxygen:

$$O_2 + 4e^- + 4H^+ \rightarrow 2H_2O \qquad (4-2)$$

There are different types of fuel cells: Protonic-exchange Membrane (PEM), Solid Oxides (SOFC), Alkaline Anion Exchange Membranes (AAEMFC) and so on. In this work we concentrated on Protonic Fuel Cells, which are represented graphically in *Figure 18*. In these devices the proton is transported from the anode to the cathode trough a protonic conductor. The protonic conductors can be polymeric or ceramic. Low-temperature devices are based on polymeric membranes.

Aim of this work is to develop a ceramic materials alternative to polymeric membranes. Several bulk nanostructured oxides have been investigated on this purpose.

Low temperature protonic conductivity in nanograined bulk simple oxides has been receiving significant attention in the last few years because they might represent a potential excellent

alternative to polymers for low-temperature proton exchange membrane fuel cells (PEMFCs). Polymers have been investigated for decades as electrolytes for this application. Perfluorinated polymers, such as Nafion[72], or PBI are generally used. These materials, however, present a number of drawbacks, such as the inability to operate efficiently at temperature above 100 °C, due to their low water retention and thermal instability, a poor mechanical stability, the environmental impact and the high costs. In the last few years it has been reported the possibility to obtain significant low-temperature protonic conductivity in nanostructured bulk binary oxides[57,73–84]. In these oxides water molecules adsorbed on the surface can dissociate easily producing a superficial conductivity through a Grotthuss mechanism[85,86]. In materials deriving from the rapid densification of nanopowders using SPS or FAST methods, a nanometric residual open porosity allow for this superficial mechanism to allow for conduction across the sample even in the case of materials high values of relative density. The binary oxides in which the phenomenon has been observed are TiO_2[75,77], ZrO_2[57,73,81,83,87] and CeO_2[79,84]. In these studies it has been observed an increase in conductivity of several orders of magnitude in presence of humidity at temperature below 50 °C when the grain size is under 50 nm[81,85,86,88–91]. In these materials the water adsorbed on the surface of the nanopores creating a layer of high acidity with an enhanced mobility of protons[85,86]. The observed values of proton conductivity observed in these materials are significantly higher than the values reported for any other inorganic materials at low temperature, but in order to compete with the polymeric conductors it is important to reach conductivity values that the same conductivities.

4.1.1 Aim

In this work we have been investigating the possibility to further increase the surface conductivity in bulk nanostructured oxides through doping with sulfur. In particular we have been studying the influence of sulfur doping on the protonic conductivity of **TiO_2 ZrO_2** and **CeO_2**.

4.1.2 Titanium oxide

TiO_2 is a simple oxide that find large applications as white pigment or as an additive. Titanium oxide presents different polyforms. At room temperature it is generally found in form of Rutile, which belong to the tetragonal system. Anatase represents another polymorph, which is also tetragonal, but with a different unit cell, together with the Brookite, that is characterized by an orthorhombic form. In *Figure 35* are represented the Rutile and Anatase unit cells, while in *Table 6* are reported the lattice parameters of the two structures. Nanocrystalline TiO_2 presents generally the Anatase structure.

4.1.3 Cerium oxide

CeO_2 is a simple oxide which presents the typical crystal structure of fluorite. In *Figure 36* is represented the CeO_2 unit cell, while in *Table 7* are reported the lattice parameters of its crystal structure.

4.1.4 Zirconium oxide

ZrO_2 is a simple oxide in which zirconium is a tetravalent cation, Zr^{4+}. It is an oxide used in a large number of technological applications as structural of functional material. Zirconium oxide presents different polyforms; at room conditions it is in monoclinic form, while at higher temperatures it became first tetragonal and then cubic. In *Figure 37* are represented the unit cells of the three different polymorphs, while in *Table 8* are reported the lattice parameters of the three crystal structures. When zirconia is doped with yttrium oxide or when it is in nanostructured form, the relative stability of the polymorphs is modified and the tetragonal form became more stable at room temperature.

4.2 Experimental

4.2.1 Titanium oxide

4.2.1.1 Synthesis

Titanium oxide nanoparticles were synthesized using a precipitation technique, through the hydrolysis of titanium tetra-isopropoxide (TTIP of Sigma-Aldrich) in water. 15 mL of TTIP (97%) were added dropwise under vigorous stirring to distilled water (185 mL), previously acidified with HNO_3 (1.3 mL, ≥69%). After 2 hours, the solution was heated to 85 °C and evaporated. The resulting powder were calcined in a furnace for 1h at 400 °C (heating rate: $5\frac{°C}{min}$).

S-doped TiO_2 was synthesized using a similar approach but adding thiourea and sulphuric acid as sulfur source. In order to achieve the maximum content of sulfur it was necessary to use a ratio of 4:1 between sulfur in thiourea and Ti in TTiP, and 1:1 between sulfur in H_2SO_4 and Ti in TTIP. In this case 2 g of thiourea are dissolved in EtOH (absolute Sigma-Aldrich), then 1.950 mL of TTIP and 0.350 mL of H_2SO_4 (95-98% Sigma-Aldrich) are added to the solution. The solution is then evaporated at 85 °C until complete drying, the remaining powder is annealed in a furnace at 500 °C for 2 hours with $1\frac{°C}{min}$ in order to remove the organic residue.

A commercial nanopowder of titanium oxide in anatase form (AK1 Tronox) was also used for the study, since it presented a significant sulfur content, probably deriving from the industrial production process.

Some sintered samples of the commercial anatase were immersed in solutions of sulphuric acid at different concentrations, in the attempt to increase the amount of sulfur present on the surface of the samples. Each sintered sample was immersed in an amount of solutions enough to cover the sample. Four different concentration of H_2SO_4 were tested: 0.5 M, 1 M, 2 M, and 4 M. The samples were immersed for 1h, then dried in an oven at 160 °C for 16h and then annealed at 450 °C for 2h.

4.2.1.2 Sintering

Most of the sintered samples of the titanium oxide have been obtained in the shape of small cylinders of 5 mm of diameter. These samples are sintered in the FAST/SPS apparatus at 500-550 °C using an uniaxial pressure of 650 MPa and an heating rate of 200 $\frac{°C}{min}$. At the end of the sintering process the samples presented a discoloration, probably due to some oxygen substoichiometry. In order to restore the full oxygen stoichiometry the samples have been treated in a furnace at 450 °C for 4-5 h (10 $\frac{°C}{min}$.) in air.

Using the commercial anatase nanopowder we also produced some larger samples of 10 mm and 15 mm in diameter. The sample of 10 mm of diameter were sintered at 500 °C and 150 MPa (heating rate 200 $\frac{°C}{min}$), while the sample of 15 mm of diameter were made at 750 °C and 70 MPa.

4.2.1.3 Characterization

The samples have been characterized by XRD analysis in order to evaluate the phase composition, the lattice parameters, and the crystallite size. Both analysis have been performed using the software High-Score Plus PANalytical. The sintered samples of the protonic conduction oxides were characterized in density (section 2.3) using the theoretical densities of the oxides calculated from the crystallographic data[92]. For the sulfur doped samples, the same theoretical densities were used. SEM analysis were performed on the samples for the grain size of the sintered samples and for the evaluation of the sulfur content with EDS.

The measures of impedance spectroscopy were made with an amplitude voltage of 100 mV in a range of frequency of 0.1-10^6 Hz. The measures have been made at different values of relative humidity (10-100 %) at 80°C.

4.2.2 Cerium oxide

4.2.2.1 Synthesis

Cerium oxide nanopowder have been obtained by a precipitation technique using a solution of Ce(NO$_3$)$_3$·6H$_2$O (99 % Sigma-Aldrich) as a precursor. The salt (1,3360 g) was dissolved in 55 mL of distilled water, then 5 mL of NH$_4$OH (33%) have been added to the solution which become opaque and brown; the mixture was heated at 85 °C until complete evaporation of water. Gradually the mixture become darker and grey, then purple and at the end light yellow. When all the solvent was evaporated a yellow powder is obtained, which was annealed at 500 °C for 1h (5 $\frac{°C}{min}$).

Cerium oxide nanopowder doped with sulfur was synthesized with a synthesis analogous to that described above, with the addition of thiourea as source of sulfur. Thiourea was dissolved in 30 mL of distilled water and added to the solution of cerium salt and ammonia. After the complete evaporation an inhomogeneous powder was obtained. This powder was annealed at 500 °C for 1h (5 $\frac{°C}{min}$).

4.2.2.2 Sintering

The cerium oxide nanopowder were sintered at 600-700 °C using a pressure of 600 MPa. At the end of the sintering process the samples have been annealed in air at 500 °C for 5h (10 $\frac{°C}{min}$) in order to restore the full oxygen stoichiometry.

4.2.2.3 Characterization

The samples have been characterized by XRD analysis in order to evaluate the phase composition and the crystallite size. Both analysis have been performed using the software High-Score Plus PANalytical. The sintered samples of the protonic conduction oxides were characterized in density (section 2.3) using the theoretical densities of the oxides calculated from the crystallographic data[92].

For the sulfur doped samples, the same theoretical densities were used. SEM analysis were performed on the samples for the grain size of the sintered samples and for the evaluation of the sulfur content with EDS.

The measures of impedance spectroscopy were made with an amplitude voltage of 100 mV in a range of frequency of $0.1\text{-}10^6$ Hz. The measures have been made at different values of relative humidity (10-100 %) at 80°C.

4.2.3 Zirconium oxide

4.2.3.1 Synthesis

The samples of zirconium oxide have been obtained using either YSZ (TOSOH-ZIRCONIA TZ-3Y) and sulfur-doped zirconia without any stabilizer. This last material was obtained using a solvent-free synthesis[82]. $ZrO(NO_3)_2*2H_2O$ (99 % Sigma-Aldrich) was reacted with $(NH_4)_2SO_4$ (A.C.S. Reagent 99+ % Sigma-Aldrich) with a weight ratio of 29% of $ZrO(NO_3)_2*2H_2O$ on the total weight. The two reactants have been grinded separately in a mortar for 10 minutes and then mixed and grinded again for 10 more minutes. The mixture was then placed in a Falcon container and is left to rest overnight at room temperature. The powder is then annealed in an oven at 600°C for 5h (ramp rate $5\frac{°C}{min}$).

4.2.3.2 Sintering

The YSZ and sulfur-doped samples were sintered using a HP-FAST/SPS apparatus at 600-900 °C using a pressure of 600 MPa for 5 min.

4.2.3.3 Characterization

The samples have been characterized by XRD analysis in order to evaluate the phase composition, the lattice parameters, and the crystallite size. Both analysis have been performed using the

software High-Score Plus PANalytical. The sintered samples of the protonic conduction oxides were characterized in density (section 2.3) using the theoretical densities of the oxides calculated from the crystallographic data[92]. For the sulfur doped samples, the same theoretical densities were used. SEM analysis were performed on the samples for the grain size of the sintered samples and for the evaluation of the sulfur content with EDS.

The measures of impedance spectroscopy were made with an amplitude voltage of 100 mV in a range of frequency of $0.1\text{-}10^6$ Hz. The measures have been made at different values of relative humidity (10-100 %) at 80°C.

4.3 Results

4.3.1 TiO$_2$

4.3.1.1 Synthesis and sintering

The synthesized nanopowders of TiO$_2$ and S-TiO$_2$ showed an anatase crystal structure and a nanometric crystallite size, the crystallite size calculated from the patterns with the Scherrer equation is 10 nm for the TiO$_2$ powder and 20 nm for S-TiO$_2$. The AK1 commercial powder presented also an anatase structure and a nanometric crystallite size of 20 nm. The XRD patterns of the powders are reported in *Figure 38*. The lattice parameter of the powders calculate from the patterns are reported in *Table 10*, as is possible to see there is not a significant difference between the undoped and the doped powders. It can be noted that the XRD of the undoped TiO$_2$ shows a small peak at about 30°, which belongs to the brookite crystal structure. This peak was absent in the commercial TiO$_2$ AK1 and in the S-TiO$_2$, suggesting that the presence of sulfur has a stabilizing effect on the anatase crystal structure.

The amount of sulfur present in S-TiO$_2$ is 7.2 at. %, while in TiO$_2$ AK1 1.7 at %. These values have been estimated using EDS spectroscopy.

The sintered samples deriving from the TiO_2 nanopowders were dense and compact and present a nanometric grain size, as it is possible to see from the XRD patterns in *Figure 39* and from the SEM images in *Figure 41*. The XRD patterns show also that the sintered TiO_2 AK1 and S-TiO_2 samples maintained a single phase anatase crystal structure, while instead the TiO_2 undoped sintered sample shows the presence of anatase, rutile and a small amount of brookite. This is a further evidence that the presence of sulfur results in the stabilization of the anatase structure.

The samples sintered starting from AK1 powder and immersed in H_2SO_4 at different concentrations maintain the same structure of the sintered sample before the immersion as evidenced in *Figure 40*.

The grain size of the sintered samples, calculated from the SEM images, resulted 27(5) nm for TiO_2, 30(10) nm for TiO_2 AK1 and 35(5) nm for S-TiO_2.

4.3.1.2 Electrochemical results

The sintered samples of TiO_2 deriving from the different powders have been characterized for their conductivity using impedance spectroscopy. In *Figure 42*, *Figure 43,* and *Figure 44*, are reported, as an example, the impedance plot of sintered TiO_2 samples obtained using undoped, AK1, and S-TiO_2 nanopowders, registered at the same temperature and at the same relative humidity. The sample with the higher value of resistivity presents a plot that is composed by a complete semicircle. The samples presenting the lower resistivity values show only a partial semicircle. In *Figure 45* are reported the impedance plot relative to TiO_2 undoped sintered exposed at different values of relative humidity. It is possible to observe a drastic reduction in the dimension of the semicircle, and of the sample resistivity, with the increase of relative humidity. For this sample a rise of the relative humidity from 10 to 100 % produces an increase the conductivity ($\frac{S}{cm}$) from $3 \cdot 10^{-10}$ to $4 \cdot 10^{-7}$ as is reported in *Figure 46*.

The commercial AK1 and the S-doped samples, both containing sulfur, although in different amounts, also presented an increase in conductivity with the increase in RH%, but in this case the values of conductivity are higher and increase with the sulfur content. For AK1 sample the conductivity increases from $2 \cdot 10^{-6} \frac{S}{cm}$ (RH=10%) to $5 \cdot 10^{-3} \frac{S}{cm}$ (RH=100%), while for S-TiO$_2$ from $6 \cdot 10^{-5} \frac{S}{cm}$ (RH=10%) to $7 \cdot 10^{-2} \frac{S}{cm}$ (RH=100%). The trend of conductivity vs. RH% in logarithmic scale is compared for the three samples in *Figure 47*.

The AK1 sintered samples immersed in H$_2$SO$_4$ at different concentration, shows an increase in their conductivity in humid atmosphere deriving from the treatment with the acid, that increases with its concentration. The values of the conductivity these samples are reported and compared in *Figure 48*. The conductivity of the sample immersed in H$_2$SO$_4$ 0.5 M passes from $3 \cdot 10^{-5} \frac{S}{cm}$ (RH=10 %) to $8 \cdot 10^{-3} \frac{S}{cm}$ (RH=100%), those of the sample immersed in the 1M acid passes from $4 \cdot 10^{-5} \frac{S}{cm}$ (RH=10 %) to $9 \cdot 10^{-3} \frac{S}{cm}$ (RH=100%).

Sintered samples of AK1 powder presenting diameters shows the same dependence of conductivity from their relative humidity. The samples of 5 and 10 mm show very similar values of conductivity. The conductivity of the 5 mm sample increases from $2 \cdot 10^{-6} \frac{S}{cm}$ (RH=10 %) to $5 \cdot 10^{-3} \frac{S}{cm}$ (RH=100%), for the 10 mm sample from $1 \cdot 10^{-6} \frac{S}{cm}$ (RH=10 %) to $1 \cdot 10^{-2} \frac{S}{cm}$ (RH=100%), while for the 15 mm samples the conductivity passes from $8 \cdot 10^{-7} \frac{S}{cm}$ (RH=10 %) to $1 \cdot 10^{-3} \frac{S}{cm}$ (RH=100%) for the same temperature. The values of 15 mm samples are lower. This sample also presents a lower relative density because it was densified using a lower pressure. These trends are reported and compared in *Figure 49*.

4.3.2 CeO$_2$

4.3.2.1 Synthesis and sintering

The powder of CeO$_2$ and S-CeO$_2$ shows at the XRD a single phase fluoritic structure, as shown in

Figure 50. From the XRD patterns and from the SEM images in *Figure 52* it is possible to see that the

crystallite size is nanometric, from the Scherrer equation it results to be 20 nm for both the powders.

The lattice parameter of the powders calculate from the patterns are reported in *Table 10*, as is

possible to see there is not a significant difference between the undoped and the doped powders.

The amount of sulfur in S-CeO$_2$ nanopowder has been estimated to be around 13 at. % from the EDS

analysis.

The sintered samples obtained using these nanopowders are not very dense, the density range

of values is reported in *Table 9*. They are composed of a single phase, the fluorite crystal structure

and present a nanometric gran size, as is possible to see in *Figure 51*.

4.3.2.2 Electrochemical results

The undoped CeO$_2$ sintered sample doesn't present any evident variation in the conductivity with

the relative humidity, as shown in *Figure 53*. The conductivity, in fact, varies between of $1.5 \cdot 10^{-9}$ -

$7 \cdot 10^{-9} \frac{S}{cm}$ The S-CeO$_2$ presents a different behavior. In this material the conductivity rises with the

increase in relative humidity with values that vary from $8 \cdot 10^{-10} \frac{S}{cm}$ at 10 % of RH and then arrive at

$1 \cdot 10^{-5} \frac{S}{cm}$ at 100 % of RH. The full set of data are reported in *Figure 53* .

4.3.3 ZrO$_2$

4.3.3.1 Synthesis and sintering

S-ZrO$_2$ nanopowder at XRD shows an amorphous pattern, as can be seen in *Figure 55*. In order to

produce some crystallization the thermal treatment at 600 °C have been extended from 5h to 18 h.

As *Figure 56* shows as the longer annealing produced a crystallization in the S-ZrO$_2$, resulting in a phase presenting a tetragonal crystal structure and a nanometric crystallite size (5 nm). This last point is confirmed also from the SEM images in *Figure 59*. The EDS analysis estimated a sulfur content of about 12 at. %.

The sintered samples of YSZ commercial powders are monophasic and characterized by a tetragonal crystal structure, while the starting powder presented a mix of tetragonal and monoclinic phases (*Figure 54* and *Figure 57*). The sintered samples of S-ZrO$_2$ presented a mixture of tetragonal and the monoclinic crystal structures. As shown in *Figure 58* the quantity of monoclinic phase increases when the sintering temperature increases from 700 °C to 900 °C. The microstructure of S-ZrO$_2$ samples sintered at 700 °C and 800 °C are showed in the SEM images in *Figure 60*. The images evidence the presence of a nanometric grain size.

The relative densities of the sintered samples obtained from the different kind of nanopowders are summarized in *Table 9*.

The grain size of the S-TiO$_2$ sintered samples, calculated from the SEM images, resulted 55(10) nm for the sample sintered at 700 °C and 65(10) nm for the sample sintered at 800 °C.

4.3.3.2 Electrochemical results

The undoped YSZ sintered samples of zirconia shows an increase in conductivity with the rise of the relative humidity, which passes from $4 \cdot 10^{-10} \frac{S}{cm}$ (RH=10 %) to $5 \cdot 10^{-6} \frac{S}{cm}$ (RH=100%). The doping with sulfur produces a drastic increase in the conductivity with values that growth from $2 \cdot 10^{-8} \frac{S}{cm}$ (RH=10 %) to $2 \cdot 10^{-1} \frac{S}{cm}$ (RH=100%).

The conductivity values of the two type of samples are reported in function of the relative humidity in *Figure 61*.

4.4 Discussion

The presented experimental data evidence as the doping with sulfur, on all the oxide we investigated, leads to a significant enhancement in the protonic conduction. This result derives probably from the increase in surface acidity produced from this treatment. Although the sulfur is included in the bulk of the material it is its influence on the surface properties to be particularly relevant, as the protonic transport in these materials has been demonstrated to be associated to a superficial process. The increase in surface acidity produces a stronger dissociation in the water molecules adsorbed on the surface of the nanopores, producing a more efficient the transport of protons[85]. The doping with sulfur in nanocrystalline zirconium oxide has been demonstrated to produce a superacid solid, S-ZrO$_2$, that presents a Hammett acid strength <−14, which varies depending on the preparation method[93–97]; the Hammett acid strength is a measure of acidity that is used for very concentrated solutions of strong acids, it can replace pH in concentrated solutions. This characteristics has been largely exploited in catalysis[93,94,96,97] and more recently in protonic conduction applications[82,89,90]. The superacid nature of this material explain the high values of proton conductivity. A similar behavior has been observed also in the other two investigated oxides. It must be noted, however, that the sintered samples reach such high level of protonic conduction thanks to their nanostructure. The open nanoporosity present in these materials represent, in fact, a large portion of their surface. It is in the water layers on the pore walls that mostly happens the protonic conduction phenomenon[85].

Cerium oxide did not show a significant increase in protonic conductivity with the doping of sulfur. Although the sulfur doping an increase in conductivity the observed values do not appear to be high enough to be exploited for the realization of solid protonic conductor electrolyte. It must also be noted that the undoped ceria present a proton conductivity that has a very low dependence from the relative humidity.

In the TiO_2 AK1 sample the treatment with H_2SO_4 show an increase the values of conductivity, although not particularly relevant. Comparing the conductivities of the samples at 100% of RH% it is possible to observe that the treatment with acid increase the conductivity from $5 \cdot 10^{-3} \frac{S}{cm}$, to $8 \cdot 10^{-3} \frac{S}{cm}$ in the case of H_2SO_4 0.5M to $9 \cdot 10^{-3} \frac{S}{cm}$ in the case of treatment with H_2SO_4 1M. In particular the increase produced by the increase in concentration of H_2SO_4 is very modest.

In the case of zirconia the conductivity values resulted to be promising despite the samples being bi-phasic.

The sintered samples of both $S\text{-}TiO_2$ and $S\text{-}ZrO_2$ reach very good values of protonic conductivity at high values of relative humidity, values comparable with that of perfluorinated polymers[72,98], which present a conductivities in the range of $0.01\text{-}0.1 \frac{S}{cm}$ at high values of relative humidity. $S\text{-}TiO_2$ and $S\text{-}ZrO_2$, in fact, present conductivity values at 100% of RH that are $7 \cdot 10^{-2} \frac{S}{cm}$ and $2 \cdot 10^{-1} \frac{S}{cm}$ respectively. These materials appear to be promising alternative to polymeric electrolytes. The two sulfur doped oxides have two different graphs of conductivity vs. RH%, in fact the two interpolating straight lines of the logarithmic value of conductivity in function of RH% have a different slope; the ZrO_2 has an higher slope than TiO_2, this involves that they have two different activation energy for the protonic transport. The $S\text{-}ZrO_2$ starts to conductivity values lower than $S\text{-}TiO_2$ at low relative humidity, but at the highest values of RH% the first oxide reaches the second one.

4.5 Conclusions

The doping of sulfur in the sintered samples of the simple oxides studied, TiO_2, CeO_2 and ZrO_2, lead to an increment of the low-temperature protonic conduction values in all the three ceramic samples. Despite this $S\text{-}CeO_2$ does not reach optimal values for the PEMFC applications, instead $S\text{-}TiO_2$ and $S\text{-}ZrO_2$ show conductivities as high to be a good option as solid-state proton exchange membrane.

5. High-entropy oxides

5.1 Introduction

5.1.1 Lithium batteries

In batteries the electrochemical energy is generated through oxidation and reduction reactions that take place at the electrodes. Commercial batteries are composed by a number of electrochemical cells, connected in series or in parallel, which together can produce the required voltage and capacity[99–101]. Two type of batteries exist: primary and secondary. In the primary batteries, the chemical energy is converted in electrical energy and cannot be repristinated; the most common primary batteries are zinc-carbon[102] and the alkaline-manganese ones[103]. In the secondary batteries the electrochemical processes are reversible and the battery can be recharged using an external electrical energy source. The most common types of secondary batteries are lead-acid batteries[100], nickel-cadmium[104], nickel-metal hydride[105], and li-ion batteries[27,28,106]. Recently new type of batteries, derived from li-ion ones, were studied, such as Na-ion[107] and K-ion batteries[108].

The constituent elements of a rechargeable battery are:

- positive electrode, or cathode,

- negative electrode, or anode,

- electrolyte,

- current collector.

The positive and the negative electrodes are connected through the electrolyte, which allows the transport of the ion involved in the redox process. In lithium batteries during the discharge the anode provides electrons to the external circuit deriving from the oxidation of lithium, while the Li^+ ions migrate through the electrolyte towards the positive electrode:

$$Li \rightarrow Li^+ + e^- \qquad\qquad (5\text{-}1)$$

The cathode accepts electrons from the external circuit and the Li^+ ions are reduced through the reaction:

$$Li^+ + e^- \rightarrow Li \qquad\qquad (5\text{-}2)$$

The electrolyte is an ionic conductor but an electronic insulator. It has the function of keeping the two electrodes separated, while allowing the transfer of ions between them. During the charge process the previous processes are reversed: the oxidation process takes place at the cathode, the Li^+ ions flow through the electrolyte to be reduced at the anode, while the electrons run in the external circuit[106]. A schematic representation of a lithium-ion battery is reported in *Figure 63*.

The lithium-ion rechargeable batteries have found a rapidly increasing application in several technological area such as automotive, telecommunications and computing due to their high density energy, and long life and low weight (*Figure 64*[109]).

A typical lithium battery includes an anode, typically made of graphite, Li_xC_6, or metallic Li, a cathode, made of a complex oxide containing lithium and a transition metal, such as $LiCoO_2$, and a lithium-ion conducting electrolyte. The electrolyte is usually made dissolving a lithium salt in an organic solvent[106,110,111]. During the charge cycle, lithium is extracted from the cathode and inserted in the anode, while during the discharge, the lithium ions are released by the anode and inserted in the cathode.

Extensive studies have been dedicated in the last few decades to the develop of new materials for lithium-ion batteries in order to improve their properties. These studies have been focused on all the components: anodes, cathodes and electrolytes. In this work the study has been concentrated on materials for the cathodes. The active cathode of a lithium-ion battery requires a

material in which lithium ions can enter and be extracted in a reversibly way for a large number of cycles[110]. An ideal cathode material should satisfy several requirements. The transition metal present in the insertion compound must present a large work function in order to maximize the cell voltage. It should allow the insertion/extraction of a large amount of lithium ions in order to maximize the cell capacity. The lithium insertion/extraction process must be reversible with no or minimal changes in the host structure. Finally, it should present good electronic and Li^+ conductivities to minimize cell polarizations. A large number of materials have been investigated, such as metal oxides, metal sulfides, conducting polymers and poly(sulfides). However, so far transition metal oxides have been the most successful materials, thanks to their chemical and structural stability, high lithium ion capacity and optimal electrical properties. The transition metal oxides that are more used in lithium-ion batteries are $LiCoO_2$, $LiNiO_2$, $LiMnO_2$, LiV_2O_5 and $LiMn_2O_4$.

In the last years there has been significant work with the objective of optimizing the performance of the spinel $LiMn_2O_4$ through the substitution of cations. Different cations, such as Li, B, Mg, Al, Fe, Co, Ni and Zn have been investigated as possible dopants[110,112–117].

This work was based on the synthesis of new cathode materials with the crystal structure of $LiMn_2O_4$, in which the sites of Mn(III) and Mn (IV) are partially substituted with different cations.

5.1.2   High-entropy oxides

High-entropy oxides represent a new class of materials that has been emerging recently as a promising new area of interest in materials science. A rapidly growing number of studies have been focused on these materials for various application[118–128].

The interest towards high entropy systems was originally focused on metallic systems. High-entropy alloys have been investigated for more than a decade. The central idea was to maximize the configurational entropy of an alloy introducing a large number of component in equimolar or near equimolar quantities[123]. A similar approach has been recently extended also to oxides and

other ceramic phases. The synthesis of high-entropy ceramics is based on the concept that configurational disorder can contribute to the stability of complex oxides leading to the formation of novel phases characterized by unusual cationic coordinations[124].

High entropy oxides (HEOs) are complex oxides that contain five or more different metal cations in equimolar ratios. One or more of the involved cations present an oxide characterized by a crystal structure different from the one of the HEO. The resulting structure is not stabilized by an enthalpic contribution, that would favor the formation of a multiphasic system, but from a configurational entropic contribution. The entropic contribution becomes more relevant with the temperature. In fact, these oxides present a stability that decrease with temperature and must be quenched in order to be obtained in single phase form at room temperature. The first high-entropy oxide prepared was reported by Rost et al[124], and has the formula $Cu_{0.2}Co_{0.2}Mg_{0.2}Ni_{0.2}Zn_{0.2}O$ and a rock salt crystal structure. The remarkable aspect of this oxide is represented by the fact that Cu and Zn oxides do not present a rock salt crystal structure and show minimal low-temperature solubility with the other three oxides. Other high-entropy oxides, presenting fluoritic[121], spinel[119], and perowskyte[122] crystal structures have been obtained afterwards.

5.2 Aim

The aim of this part of the thesis is to synthesize lithium-containing high-entropy oxides in nanometric form that can be used as cathode materials in lithium-ion batteries. $LiMn_2O_4$ has been chosen as base material. The goal is to partially substitute the Mn(III) and Mn(IV) sites with different combinations of other cations in order to obtain oxides with the same crystal structure of $LiMn_2O_4$ but with a larger unit cells in order to favor the intercalations and extraction of lithium and to characterize their electrochemical properties.

5.2.1 Structure of the work

The initial scope was to obtain an increase in the lattice constant of $LiMn_2O_4$ through the insertion of rare-earth cations in the structure. The rare earth-metal ions investigated were Y^{3+}, In^{3+} and Tb^{4+}. It must be noted that none of these cations can dissolve in a significant amount in $LiMn_2O_4$ due to the large difference in ionic radius. In order to obtain the insertion other ions, characterized by an ionic radius closer to that of Mn^{3+} and Mn^{4+}, were also included in the oxide in order to obtain an increase in the solubility of the rare-earth ions due to a general expansion in the lattice and to a significant configurational entropy contribution. The transition ions used to this purpose were Fe^{3+}, Cr^{3+}, Al^{3+}, Ti^{4+}, and Zr^{4+}. The choice of these ions was made on the basis of their ionic radius and cost. A summary of the ionic radius of some trivalent and tetravalent cations is reported in *Table 12*.

5.3 $LiMn_2O_4$ structure

$LiMn_2O_4$ is an oxide with a spinel crystal structure belonging to the space group Fd-3m. In this structure lithium is a monovalent cation, while manganese is present as either Mn^{3+} and Mn^{4+}. The Li^+ ions occupies the tetrahedral sites of the spinel structure, Mn^{3+} and Mn^{4+} occupy the octahedral sites[129]. The manganese ions do not occupy all the octahedral sites of the structure, but there are some sites that are vacant. The Li^+ ions can move in the structure between adjacent tetrahedral positions passing through a vacant octahedral site. The structure is schematized in *Figure 65,* while the lattice parameters are reported in *Table 11*.

5.4 Experimental

Different compounds, with different stoichiometry have been synthesized in this work. All the formulas are reported in *Table 13*. For almost all the compounds the stoichiometry follows this general formula:

$$Li(Mn^{III}_{1-x-z}A^{III}_xB^{III}_z)(Mn^{IV}_{1-y-n}C^{IV}_yD^{IV}_n)O_4 \qquad \textit{(5-3)}$$

whit $x=z=\dfrac{1}{\textit{number of trivalent cations}}$ and $y=n=\dfrac{1}{\textit{number of tetravalent cations}}$, where x, z, y and n are approximated to the second figure after the decimal point. Some of the obtained compounds present a stoichiometry that does not follow the *equation 5.3*.

5.4.1 Synthesis

All the compounds were synthesized using a modified sol-gel synthesis, with the Pechini approach[130]. The cations were used as water soluble salts. The salt of lithium used in all the synthesis was lithium acetate ($CH_3COOLi \cdot 2H_2O$ Sigma-Aldrich reagent grade); Ti^{4+} was added as Ti(IV) isopropoxide (Sigma-Aldrich 97%), Zr^{4+} as Zirconium(IV) oxynitrate hydrate ($ZrO(NO_3)_2 \cdot XH_2O$ Sigma-Aldrich 99 %); all the other cations are used in form of nitrates:

- Mn^{3+}, Mn^{4+}, $Mn(NO_3)_2 \cdot 4H_2O$ (Sigma-Aldrich 97 %)

- Fe^{3+}, $Fe(NO_3)_3 \cdot 9H_2O$ (Sigma-Aldrich ACS reagent Ph eur)

- Cr^{3+}, $Cr(NO_3)_3 \cdot 9H_2O$ (Alfa-Aesar 98.5 %)

- Al^{3+}, $Al(NO_3)_3 \cdot 9H_2O$ (Sigma-Aldrich 98 %)

- Y^{3+}, $Y(NO_3)_3 \cdot 6H_2O$ (Sigma-Aldrich 99.9 %)

- In^{3+}, $In(NO_3)_3 \cdot XH_2O$ (Sigma-Aldrich 99.9 %)

- Tb^{3+}, $Tb(NO_3)_3 \cdot 5H_2O$ (Sigma-Aldrich 99.9 %)

The synthesis was started dissolving the salts of the cations in the right stoichiometric ratio in water. Citric acid (Sigma-Aldrich 99 %) was then added to the solution, as complexing and gelling agent. The molar quantity of citric acid is equal to the sum of the moles of all the cations present in the

solution with a 10 % excess. When titanium was used the Ti isopropoxide was first dissolved in acetylacetone (Sigma-Aldrich 99 %) before adding it to the water solution containing the other cations. In this case the procedure we followed was to mix in a glass vial the right amount of titanium isopropoxide (with a 10% excess) with acetylacetone and then to pour this solution the water. When all the salts and the citric acid were dissolved in water the solution was heated at 80°C overnight, in order to obtain the evaporation of the water. The formed gel was then treated at 120°C for 2h in order to eliminate the residual water and start the degradation of the nitrates. The gel was then transferred into an alumina boat and annealed in a furnace in order to decompose the nitrated and the organic components. The oxides were formed as a brown powder. Different temperatures and times have been investigated in order to obtain the oxides with the required spinel structure. The range of temperatures considered was between 300 °C and 1000 °C.

As an example, in order to synthesize 0.5 g of $LiAl_{0.33}Fe_{0.33}Ti_{0.5}Mn_{0.84}O_4$, was necessary to use 0.3030 g of $CH_3COOLi \cdot 2H_2O$, 0.3088 g of $Al(NO_3)_3 \cdot 9H_2O$, 0.6262 g of $Mn(NO_3)_2 \cdot 4H_2O$, 0.3960 g of $Fe(NO_3)_3 \cdot 9H_2O$, 0.456 mL of Ti isopropoxide dissolved in 0.169 mL of acac and 1.8490 g of citric acid in about 100 mL of water.

5.4.1.1 $LiMn_2O_4$

The $LiMn_2O_4$ oxide was synthesized using the procedure described above. In order to obtain 0.5 g of product, 0.4750g of $CH_3COOLi \cdot 2H_2O$, 1.1687 g of $Mn(NO_3)_2 \cdot 4H_2O$ and 1.7532 g of citric acid were added to about 100 mL of H_2O. The powder, after being dried, was calcinated at 300 °C for 10 h.

5.4.1.2 $LiYMnO_4$

The first rare-earth compound we investigated was *LiYMnO₄.* In this case in order to obtain 0.5 g of product, 0.2375 g of $CH_3COOLi \cdot 2H_2O$, 0.5843 g of $Mn(NO_3)_2 \cdot 4H_2O$, 0.8916 g of $Y(NO_3)_3 \cdot 6H_2O$ and

1.4756 g of citric acid were added to about 100 mL of H_2O. The powder, after being dried, was calcinated using different thermal treatments: 300 °C for 10h, 400 °C for 10 h, 500 °C for 5h, 750 °C for 2h, 750 °C for 4h, and 900 °C for 2h.

5.4.1.3 LiFe$_{0.5}$Ti$_{0.5}$MnO$_4$

LiFe$_{0.5}$Ti$_{0.5}$MnO$_4$ was one of the few compounds we synthesized without any rare-earth cation in it. In this case, in order to obtain 0.5 g of product, 0.2870 g of $CH_3COOLi·2H_2O$, 0.7062 g of $Mn(NO_3)_2·4H_2O$, 0.5683 g of $Fe(NO_3)_3·9H_2O$, 0.432 mL of Ti isopropoxide, 0.160 mL of acac and 1.7837 g of citric acid were added to about 100 mL of H_2O. The powder, after being dried, was calcinated using different thermal treatments: 400 °C for 10 h, 500 °C for 5h, 600 °C for 3h, 600 °C for 2h, and 800 °C for 2h.

5.4.1.4 Other compounds

All the other compounds were synthesized using procedures similar to the ones described above. The thermal treatment used for each compound are summarized in *Table 14*.

5.4.2 Sintering

LiFe$_{0.5}$Ti$_{0.5}$MnO$_4$, LiFe$_{0.6}$Ti$_{0.6}$Mn$_{0.8}$O$_4$, LiFe$_{0.7}$Mn$_{0.6}$Ti$_{0.7}$O$_4$ and LiFe$_{0.5}$Mn$_{0.5}$TiO$_4$, that are the four more interesting powder compounds obtained, were sintered in a 5 mm sintered sample with HP-FAST in order to obtain samples for the electrochemical impedance analysis. The nanopowders were sintered at 700 °C, with a ramp rate of 130 $\frac{°C}{min}$ using a pressure of 200 MPa for 15 min.

5.4.3 Characterization

The materials we synthesized have been characterized by XRD analysis in order to evaluate the phase composition and the lattice parameters of the spinel phase. Both analysis have been

performed using the software High-Score Plus PANalytical. Only on few samples, the ones considered the more promising for the electrochemical application, impedance measures have been performed. The impedance spectra were made on the sintered samples of these compounds between 25 °C and 300 °C using a voltage of 150 mV in a range of frequency between 0.01 and $5\cdot10^5$ Hz.

5.5 Results

5.5.1 Synthesis

5.5.1.1 LiMn$_2$O$_4$

The LiMn$_2$O$_4$ synthesized with the Pechini synthesis and calcinated at 300 °C for 10 h resulted to be a single-phase material with the spinel crystal structure, as can be seen in *Figure 66*. The XRD pattern show broad peaks, which are indication of a nanometric grain size. From the Scherrer analysis the dimension of the crystallites resulted to be about 20 nm. The lattice parameter of the spinel phase has been obtained using Rietveld refinement and resulted to be 8.173(1) Å as is reported in *Table 15* Lattice parameters a=b=c of the spinel crystal phase in the composition obtained as pure single phase.

5.5.1.2 LiYMnO$_4$

The compound LiYMnO$_4$ was the first produced including the Yttrium ion. The synthesis followed by annealing at different temperature did not allowed to obtain a single-phase product. In all cases a polyphasic material was obtained , as it is possible to see in *Figure 67*.

   The powder calcined at 300 °C resulted to be amorphous. Between 300 °C and 500 °C the product was still partially amorphous with the crystalline fraction being a mixture of Y$_2$O$_3$ and Li$_2$MnO$_4$. The powders calcined at temperatures between 750 °C and 900 °C are fully crystalline and the peaks present in their XRD patterns evidence the presence of the phases Y$_2$O$_3$ and LiMn$_2$O$_4$.

5.5.1.3 LiFe$_{0.5}$Ti$_{0.5}$MnO$_4$

The compound LiFe$_{0.5}$Ti$_{0.5}$MnO$_4$ have been synthesized with the Pechini method and calcinated at different temperatures. In all the cases a single phase product was obtained with a spinel structure, as shown in *Figure 68*. In the XRD of the powder calcinated at 400 °C there was still some amorphous material which was converted to a fully crystalline with the increase in the annealing temperature. The XRD of the powders calcinated at 400 °C, 500 °C and 600 °C show broad peaks, an indication of nanometric grain size, while the powder calcinated at 800 °C shows narrow peaks. The lattice parameter of the compound has been calculated from the XRD pattern of the powder treated at 800 °C and resulted to be 8.2753(6) Å as reported in *Table 15* Lattice parameters a=b=c of the spinel crystal phase in the composition obtained as pure single phase.

5.5.1.4 Other compounds

The second compound containing Y that has been produced corresponded to the composition **LiY$_{0.33}$Fe$_{0.33}$Mn$_{1.34}$O$_4$**. The powder obtained from the sol-gel synthesis has been calcinated at different temperatures, as reported in *Table 14*. As shown in *Figure 69* the powders after the annealing at 400 °C, 500 °C and 600 °C show the presence of the peaks of the LiMn$_2$O$_4$ spinel crystal structure, but also of an amorphous phase. In *Figure 69* it is reported the XRD pattern of the powders calcinated at 800 °C. The material is not amorphous anymore, but it presents two crystalline phases: one with LiMn$_2$O$_4$ spinel structure, and one with Mn$_2$O$_5$Y orthorhombic structure. The lattice parameter of the LiMn$_2$O$_4$ spinel phase of **LiY$_{0.33}$Fe$_{0.33}$Mn$_{1.34}$O$_4$** calculated from the XRD pattern of the powders annealed at 800 °C was 8.241(3) Å, as reported in *Table 15 Lattice parameters a=b=c of the spinel crystal* phase in the composition obtained as pure single phase.

Other Yttrium containing compounds that have been investigated are **LiFe$_{0.33}$Y$_{0.33}$Ti$_{0.5}$Mn$_{0.84}$O$_4$**, **LiY$_{0.25}$Al$_{0.25}$Fe$_{0.25}$Ti$_{0.5}$Mn$_{0.75}$O$_4$** and **LiY$_{0.25}$Fe$_{0.25}$Cr$_{0.25}$Ti$_{0.5}$Mn$_{0.75}$O$_4$**. In these compounds some cations

with an ionic radius intermediate between that of Mn^{III}/Mn^{IV} and Y^{3+} (the ionic radius of all the cations used are reported in *Table 12*) have been added in order to increase the configurational entropic contributions and stabilize the formation of a single phase. Also in this case the thermal treatment at 600 °C for 3h led to the formation of a partially amorphous material, so we report only the XRD patterns made on the powders treated at 800 °C. In these patterns, reported in *Figure 73*, it is possible to observe the presence of a majority phase, presenting a spinel crystal structure, but also small peaks related to other phases, that we could not identify. This happened also for the **$LiFe_{0.5}Ti_{0.33}Zr_{0.33}Mn_{0.84}O_4$** compound. For all these compounds we have been able to calculate the lattice parameters of the spinel phase, that are reported are in *Table 16.*

The compounds **$LiAl_{0.33}Fe_{0.33}Ti_{0.5}Mn_{0.84}O_4$** and **$LiFe_{0.33}Cr_{0.33}Ti_{0.5}Mn_{0.84}O_4$**, as in the case of $LiFe_{0.5}Ti_{0.5}MnO_4$, have been obtained as a single phase material with a spinel crystal structure using both 600 °C and 800 °C as annealing temperatures. In *Figure 70* we reported the XRD patterns of the compounds annealed at 600 °C for 3h, which are more interesting of that calcinated at 800 °C because they are in nanometric form. The lattice parameters calculated from the patterns are 8.206(3) Å for $LiAl_{0.33}Fe_{0.33}Ti_{0.5}Mn_{0.84}O_4$ and 8.251(2) Å for $LiFe_{0.33}Cr_{0.33}Ti_{0.5}Mn_{0.84}O_4$ (*Table 14*).

$LiFe_{0.5}Ti_{0.5}MnO_4$ is the phase presenting the largest lattice parameter between the compounds obtained as a single phase, so modification of the basic stoichiometry has been investigated in the attempt to obtain an even further expansion of the lattice. The following stoichiometries have been considered: **$LiFe_{0.6}Ti_{0.6}Mn_{0.8}O_4$**, **$LiFe_{0.7}Mn_{0.6}Ti_{0.7}O_4$**, **$LiFe_{0.5}Mn_{0.5}TiO_4$**, **$LiMnTiO_4$** and **$LiFeTiO_4$**. The XRD patterns of $LiFe_{0.6}Ti_{0.6}Mn_{0.8}O_4$, $LiFe_{0.7}Mn_{0.6}Ti_{0.7}O_4$, $LiFe_{0.5}Mn_{0.5}TiO_4$ treated at 600 °C are reported in *Figure 71* in comparison with $LiFe_{0.5}Ti_{0.5}MnO_4$. All three materials present a single-phase composition with a spinel structure similar to the one of $LiFe_{0.5}Ti_{0.5}MnO_4$. They also present a broadening of the peaks, typical of a nanometric grain size. The lattice parameters, calculated from the XRD patterns, are 8.2908(8) Å for $LiFe_{0.6}Ti_{0.6}Mn_{0.8}O_4$, 8.3129(9) Å for $LiFe_{0.7}Mn_{0.6}Ti_{0.7}O_4$, 8.293(1)

Å for $LiFe_{0.5}Mn_{0.5}TiO_4$. The XRD patterns of $LiMnTiO_4$ and $LiFeTiO_4$ treated at 800 °C are reported in *Figure 72*, these compounds we calcinated only at 800 °C. The lattice parameters resulted to be 8.335(1) Å for $LiMnTiO_4$ and 8.369(2) Å for $LiFeTiO_4$. Both compounds are single-phase are single-phase and present a spinel crystal structure. In $LiFeTiO_4$ there is a little peak at 25.7° (2θ) that could not be identified and is probably associated to a contamination.

The compounds **$LiY_{0.1}Fe_{0.4}Ti_{0.5}MnO_4$, $LiY_{0.05}Fe_{0.45}Ti_{0.5}MnO_4$, $LiY_{0.1}Mn_{0.9}TiO_4$** and **$LiY_{0.1}Fe_{0.9}TiO_4$** were synthesized in order to investigate the possibility to include some Yttrium in the $LiMn_2O_4$ base structure, although in a small amount. The XRD patterns of these compositions calcinated at 800 °C are reported in *Figure 74*. They show the presence of a majority phase presenting a spinel structure, but there are other small peaks related to one or more other phases, that could not be identified. The lattice parameters of the main phase are reported in *Table 16*.

The compounds **$LiY_{0.1}Fe_{0.4}Tb_{0.1}Ti_{0.4}MnO_4$** and **$LiY_{0.33}Fe_{0.33}Tb_{0.33}Ti_{0.33}Mn_{0.68}O_4$** are synthesized with the intent to include both the trivalent cation (Y^{+3}) and a rare-earth tetravalent cation (Tb^{4+}), to see if the intercalation of this big cations can enhance the incorporation of Yttrium. The XRD of the two compositions annealed at 800 °C are reported in *Figure 75.* Also in this case it is can be noted the presence of a majority phase with a spinel structure but also peaks belonging to other phases that could not be identified. The same happened also in the case of the compositions **$LiTb_{0.2}Fe_{0.4}Ti_{0.4}MnO_4$, $LiIn_{0.1}Mn_{0.9}TiO_4$, $LiIn_{0.1}Fe_{0.9}TiO_4$** and **$LiIn_{0.1}Mn_{0.1}Fe_{0.8}TiO_4$**. The lattice parameters for the spinel phase calculated from the XRD patterns of all these compounds are reported in *Table 16*.

In conclusion, the compounds **$LiFe_{0.6}Ti_{0.6}Mn_{0.8}O_4$, $LiFe_{0.7}Mn_{0.6}Ti_{0.7}O_4$, $LiFe_{0.5}Mn_{0.5}TiO_4$** and **$LiFe_{0.5}Ti_{0.5}MnO_4$** annealed at 600 °C resulted to be to most interesting outcome of this investigation. They have been obtained as single-phase and nanometric and are characterized by a significantly enlarged lattice parameters lattice parameters is respect to the parent compound $LiMn_2O_4$.

5.5.2 Electrochemical characterization

The sintered samples of **LiFe$_{0.5}$Ti$_{0.5}$MnO$_4$, LiFe$_{0.5}$Mn$_{0.5}$TiO$_4$, LiFe$_{0.6}$Ti$_{0.6}$Mn$_{0.8}$O$_4$, LiFe$_{0.7}$Mn$_{0.6}$Ti$_{0.7}$O$_4$** and

LiFe$_{0.5}$Mn$_{0.5}$TiO$_4$ were characterized for their electrical conductivity using impedance analysis. The

electrical conductivity of **LiFe$_{0.5}$Ti$_{0.5}$MnO$_4$** at room temperature resulted to be $1.43 \cdot 10^{-6} \frac{S}{cm}$, that

increases to 0.081 $\frac{S}{cm}$ at 300 °C. The values of electrical conductivity in logarithmic scale are

reported in function of the temperature in *Figure 76.* **LiFe$_{0.5}$Mn$_{0.5}$TiO$_4$** showed an electrical

conductivity of $4.32 \cdot 10^{-6} \frac{S}{cm}$ at room temperature, which increases to 0.089 $\frac{S}{cm}$ at 300 °C, as shown

in Figure 77. The electrical conductivity of **LiFe$_{0.6}$Ti$_{0.6}$Mn$_{0.8}$O$_4$** at room temperature resulted to be

$2.54 \cdot 10^{-6} \frac{S}{cm}$, that increases to 0.067 $\frac{S}{cm}$ at 300 °C (Figure 78). Finally, the electrical conductivity of

LiFe$_{0.7}$Mn$_{0.6}$Ti$_{0.7}$O$_4$ increases from $5.76 \cdot 10^{-7} \frac{S}{cm}$ to 0.020 $\frac{S}{cm}$ when the temperature increases from

room temperature to 300 ° (*Figure 79*).

From the impedance spectra at room temperature was possible to separate the ionic and

electronic contributions to the resistance, so the ionic conductivity ($\frac{S}{cm}$) were calculated for the four

compounds and reported in *Table 17*.

5.6 Discussion

All the compositions that have been investigated including Yttrium, Terbium, Indium and also

Zirconium did not produce a single-phase material, as it is possible to deduce from the results

described above. This is probably the results of the large difference in ionic radius between some of

these cations, in particular Y^{3+} (0.90 Å), Tb^{4+} (0.76 Å) and In^{3+} (0.80 Å) have the ionic radius

significantly of Mn^{3+} (0.58 Å) and Mn^{4+} (0.53 Å). These cations could not be included in the parent

LiMn$_2$O$_4$ crystal structure, even when it was enlarged by the presence of Fe^{3+}, Ti^{4+} or Cr^{3+}.

Furthermore, the contribution of configurational entropy deriving from the presence of all these cations was not enough to stabilize the structure.

In all the compounds containing Y the calcination treatments at low temperatures (400 °C, 500 °C and 600 °C) lead to a product that was always partially amorphous. In all the compounds synthesized in this work the lattice parameter of the spinel structure in larger than in the base compound $LiMn_2O_4$. In this compound the lattice parameter is 8.173(1) Å. The two compounds synthesized in pure form with the highest lattice parameters are $LiFeTiO_4$ (8.369(2) Å) and $LiMnTiO_4$ (8.335(1) Å). They contain Ti^{4+} which has an ionic radius (0.61 Å) that is bigger than that of Mn^{4+} but it is small enough to be inserted in the $LiMn_2O_4$ structure without the formation of a secondary phase. Between the compounds with more than two cations synthesized and obtained as a pure phase, the ones with the highest values of lattice parameters are $LiFe_{0.6}Ti_{0.6}Mn_{0.8}O_4$ with a value of 8.2908(8) Å, $LiFe_{0.7}Mn_{0.6}Ti_{0.7}O_4$ with a value of 8.3129(9) Å and $LiFe_{0.5}Mn_{0.5}TiO_4$ with a value of 8.293(1) Å.

The compound $LiFe_{0.5}Ti_{0.5}MnO_4$ shows a lattice parameter value of 8.2753(6) Å, the compounds with the same cations but with the addition of Y^{3+}, $LiY_{0.33}Fe_{0.33}Ti_{0.5}Mn_{0.84}O_4$ (8.294(3) Å), $LiY_{0.1}Fe_{0.4}Ti_{0.5}MnO_4$ (8.2859(9) Å) and $LiY_{0.05}Fe_{0.45}Ti_{0.5}MnO_4$ (8.2696(7) Å) have in the first two cases a lattice parameter higher than that of $LiFe_{0.5}Ti_{0.5}MnO_4$ and in the last case a lattice parameter slightly smaller than that of $LiFe_{0.5}Ti_{0.5}MnO_4$.

In conclusion the compounds **$LiFe_{0.6}Ti_{0.6}Mn_{0.8}O_4$**, **$LiFe_{0.7}Mn_{0.6}Ti_{0.7}O_4$**, **$LiFe_{0.5}Mn_{0.5}TiO_4$** and **$LiFe_{0.5}Ti_{0.5}MnO_4$** annealed at 600 °C resulted to be the more promising compounds obtained from this investigation, because these are single-phase, nanometric form and with an enlarged lattice parameters. So these compounds have started to be investigated in their electrochemical properties, the values of the electrical conductivity of all the four samples in function of the temperature is reported for comparation in *Figure 80*; in the graphs is possible to see that all the

four compounds have the same trend: the electrical conductivity increases with the rising of the temperature in almost the same way, this is the typical behavior of a semiconductor. The compounds which show the highest values of electrical conductivity are $LiFe_{0.5}Mn_{0.5}TiO_4$ and $LiFe_{0.6}Ti_{0.6}Mn_{0.8}O_4$. The ionic conductivity of the compounds is reported in *Table 17*, from these values is possible to say that all the samples seems to have almost the same ionic conductivity at room temperature and the compound $LiFe_{0.5}Ti_{0.5}MnO_4$ shows the highest value. The ionic values of conductivity can be extrapolated only from the impedance spectra recorded at room temperature, because at higher temperatures the values of the electrical conductivity are predominant and the ionic one became negligible.

The electrochemical studies made on the best compounds obtained are only a first part of a deeper study that will be done, the next step would be the investigation of their electrochemical properties as cathodes for lithium-ion batteries. This work is still under course and will be completed in the next future.

5.7 Conclusions

In conclusions a set of spinel oxides derived from the basic $LiMn_2O_4$ compound substituted with different cations, have been investigated. The insertion of rare-earth metals in this spinel structure did not result in single phase materials. In fact all the compositions containing Y^{3+}, Tb^{3+} and In^{3+} failed to produce a single-phase material. Despite this, some interesting compounds have been synthesized in single-phase spinel structure: $LiFe_{0.5}Ti_{0.5}MnO_4$, $LiAl_{0.33}Fe_{0.33}Ti_{0.5}Mn_{0.84}O_4$, $LiFe_{0.33}Cr_{0.33}Ti_{0.5}Mn_{0.84}O_4$, $LiFe_{0.6}Ti_{0.6}Mn_{0.8}O_4$, $LiMnTiO_4$, $LiFe_{0.5}Mn_{0.5}TiO_4$, $LiFe_{0.7}Mn_{0.6}Ti_{0.7}O_4$ and $LiFeTiO_4$. The more interesting of these were obtained also in nanometric form and their electrochemical characteristics will be investigated in a deeper way in the next future.

6. Tables

Table 1 Lattice parameters of cobalt ferrite.

Crystal system	Cubic
Space group	Fd-3m
Space group number	227
a (Å)	8.3860
b (Å)	8.3860
c (Å)	8.3860
α (°)	90.0000
β (°)	90.0000
γ (°)	90.0000
Calculated density ($\frac{g}{cm^3}$)	5.2900

Table 2 Structural and magnetic properties of the investigated samples: H_C, M_S, M_r recorded at room temperature and BH_{max}, grain size evaluated by SEM images and relative density.

	H_c (Oe)	M_s (emu·g^{-1})	M_r (emu·g^{-1})	BH_{max} (kJ·m^{-3})	Grain size SEM (nm)	Relative density (%)
Powder	2134	71	33	6.0	30	
SPS_1	1040	77	48	5.5	65	90
SPS_2	1000	73	42	3.8	55	96
SPS_1-m	2150	77	44	8.2	60	96

Table 3 EDS results for the Cobalt ferrite/ZrO$_2$ composite nanopowders.

ZrO$_2$/CoFe$_2$O$_4$ (mol/mol %) theoric	ZrO$_2$/CoFe$_2$O$_4$ (mol/mol %) EDS
1.5	1.7
2	1.9
5	4.2
10	8.2

Table 4 Relative density and magnetic parameters values of CoFe$_2$O$_4$-ZrO$_2$ sintered samples.

ZrO$_2$/CoFe$_2$O$_4$ (mol/mol %) theoric	Relative density (%)	H$_c$ (Oe)	M$_s$ (emu·g^{-1})	M$_r$ (emu·g^{-1})	BH$_{max}$ (kJ·m^{-3})
1.5	98	750	76	29	3.1
2	92	1400	75	32	2.8
5	86	1400	76	35	4.9
10	82	1850	69	32	4.6

Table 5 Comparison of the magnetic properties of the investigated samples with literature.

	H$_c$ (Oe)	M$_s$ (emu·g^{-1})	Grain size (nm)	Relative density (%)
This study	750-2150	70-86	45-150	88-100
[60]	239	78.9	120	97
[60]	666	70.0	100	97
[58]	222	83	71	97
[61]	640	79	28	91
[15]	580	51	10	92
[15]	525	69	12-15	93
[15]	660	70	40-50	93
[62]	826	82	<200	/

Table 6 Lattice parameters of Rutile and Anatase[131,132].

	Rutile	**Anatase**
Crystal system	Tetragonal	Tetragonal
Space group	P 4_2/mnm	I 4_1/amd
Space group number	136	141
a (Å)	4.5660	3.7770
b (Å)	4.5660	3.7770
c (Å)	2.9480	9.5010
α (°)	90.0000	90.0000
β (°)	90.0000	90.0000
γ (°)	90.0000	90.0000
Calculated density ($\frac{g}{cm^3}$)	4.32	3.91

Table 7 Lattice parameters of CeO$_2$[133].

Crystal system	Cubic
Space group	Fm-3m
Space group number	225
a (Å)	5.4050
b (Å)	5.4050
c (Å)	5.4050
α (°)	90.0000
β (°)	90.0000
γ (°)	90.0000
Calculated density ($\frac{g}{cm^3}$)	7.24

Table 8 Lattice parameters of the crystal form of Zirconia polymorphs[134–136].

	Polymorph 1	Polymorph 2	Polymorph 3
Crystal system	Cubic	Tetragonal	Monoclinic
Space group	Fm-3m	P 4_2/nmc	P 12_1/c1
Space group number	225	137	14
a (Å)	4.9250	3.6020	5.1460
b (Å)	4.9250	3.6020	5.2050
c (Å)	4.9250	5.1760	5.3130
α (°)	90.0000	90.0000	90.0000
β (°)	90.0000	90.0000	99.1000
γ (°)	90.0000	90.0000	90.0000
Calculated density ($\frac{g}{cm^3}$)	6.85	6.09	5.82

Table 9 Sintering conditions and relative density of the sintered samples of TiO_2, CeO_2 and ZrO_2 obtained.

5 mm samples	T (°C)	P (MPa)	r.d. (%)
TiO_2	500-550	650	80-90
CeO_2	600-700	600	60-80
ZrO_2	600-900	600	90

Table 10 Lattice parameter of the Anatase in TiO_2 powders and of the fluorite phase in CeO_2 powders.

Powder	a (Å), c (Å)
TiO_2	a=3.776(9), c=9.46(2)
S-TiO_2	a=3.786(3), c=9.497(9)
TiO_2 AK1	a=3.785(2), c=9.509(4)
CeO_2	a=5.411(9)
S-CeO_2	a=5.412(5)

Table 11 Lattice parameters of LiMn$_2$O$_4$[137].

Crystal system	Cubic
Space group	Fd-3m
Space group number	227
a (Å)	8.2480
b (Å)	8.2480
c (Å)	8.2480
α (°)	90.0000
β (°)	90.0000
γ (°)	90.0000
Calculated density ($\frac{g}{cm^3}$)	4.28

Table 12 Ionic radius of some trivalent and tetravalent cations in octahedral coordination [138]*.*

Trivalent cations	i.r. (Å)	Tetravalent cations	i.r. (Å)
Mn^{3+}	0.58	Mn^{4+}	0.53
Y^{3+}	0.90	Ti^{4+}	0.61
Fe^{3+}	0.55	V^{4+}	0.58
Ni^{3+}	0.56	Zr^{4+}	0.72
Al^{3+}	0.54	Tb^{4+}	0.76
Co^{3+}	0.55	Ni^{4+}	0.48
Cu^{3+}	0.54	Ta^{4+}	0.68
Cr^{3+}	0.62	Sn^{4+}	0.69
Nb^{3+}	0.72	Se^{4+}	0.50
Mo^{3+}	0.69	Ru^{4+}	0.62
Ta^{3+}	0.72	Rh^{4+}	0.60
Tl^{3+}	0.75	Re^{4+}	0.63
Ti^{3+}	0.67	Pb^{4+}	0.78
V^{3+}	0.64	Nb^{4+}	0.68
In^{3+}	0.80	Mo^{4+}	0.65
		Ir^{4+}	0.63
		Hf^{4+}	0.71
		Fe^{4+}	0.55
		Co^{4+}	0.53
		Cr^{4+}	0.55
		Tb^{4+}	0.76

Table 13 List of all the composition investigated.

	Composition	Pure single phase
1	$LiMn_2O_4$	X
2	$LiMnYO4$	
3	$LiY_{0.33}Fe_{0.33}Mn_{1.34}O_4$	
4	$LiFe_{0.5}Ti_{0.5}MnO_4$	X
5	$LiFe_{0.33}Y_{0.33}Ti_{0.5}Mn_{0.84}O_4$	
6	$LiFe_{0.5}Ti_{0.33}Zr_{0.33}Mn_{0.84}O_4$	
7	$LiAl_{0.33}Fe_{0.33}Ti_{0.5}Mn_{0.84}O_4$	X
8	$LiY_{0.25}Al_{0.25}Fe_{0.25}Ti_{0.5}Mn_{0.75}O_4$	
9	$LiFe_{0.33}Cr_{0.33}Ti_{0.5}Mn_{0.84}O_4$	X
10	$LiY_{0.25}Fe_{0.25}Cr_{0.25}Ti_{0.5}Mn_{0.75}O_4$	
11	$LiY_{0.1}Fe_{0.4}Ti_{0.5}MnO_4$	
12	$LiY_{0.05}Fe_{0.45}Ti_{0.5}MnO_4$	
13	$LiTb_{0.2}Fe_{0.4}Ti_{0.4}MnO_4$	
14	$LiY_{0.33}Fe_{0.33}Tb_{0.33}Ti_{0.33}Mn_{0.68}O_4$	
15	$LiY_{0.1}Fe_{0.4}Tb_{0.1}Ti_{0.4}MnO_4$	
16	$LiFe_{0.6}Ti_{0.6}Mn_{0.8}O_4$	X
17	$LiMnTiO_4$	X
18	$LiFe_{0.5}Mn_{0.5}TiO_4$	X
19	$LiFe_{0.7}Mn_{0.6}Ti_{0.7}O_4$	X
20	$LiY_{0.1}Mn_{0.9}TiO_4$	
21	$LiFeTiO_4$	X
22	$LiIn_{0.1}Mn_{0.9}TiO_4$	
23	$LiY_{0.1}Fe_{0.9}TiO_4$	
24	$LiIn_{0.1}Fe_{0.9}TiO_4$	
25	$LiIn_{0.1}Mn_{0.1}Fe_{0.8}TiO_4$	

Table 14 Thermal treatment of the calcination step tried on each compound.

	Composition	Thermal treatments
1	$LiMn_2O_4$	300 °C 10 h, 800 °C 2h
2	LiMnYO4	300 °C 10h, 400 °C 10 h, 500 °C 5h, 750 °C 2h, 750 °C 4h, 900 °C 2h
3	$LiY_{0.33}Fe_{0.33}Mn_{1.84}O_4$	400 °C 10h, 500 °C 5h, 600 °C 3h, 800 °C 2h
4	$LiFe_{0.5}Ti_{0.5}MnO_4$	400 °C 10 h, 500 °C 5h, 600 °C 3h, 600 °C 2h, 800 °C 2h
5	$LiFe_{0.33}Y_{0.33}Ti_{0.5}Mn_{0.84}O_4$	600 °C 3h, 800 °C 2h, 1000 °C 2h
6	$LiFe_{0.5}Ti_{0.33}Zr_{0.33}Mn_{0.84}O_4$	600 °C 3h, 800 °C 2h
7	$LiAl_{0.33}Fe_{0.33}Ti_{0.5}Mn_{0.84}O_4$	600 °C 3h, 800 °C 2h
8	$LiY_{0.25}Al_{0.25}Fe_{0.25}Ti_{0.5}Mn_{0.75}O_4$	600 °C 3h, 800 °C 2h
9	$LiFe_{0.33}Cr_{0.33}Ti_{0.5}Mn_{0.84}O_4$	600 °C 3h, 800 °C 2h
10	$LiY_{0.25}Fe_{0.25}Cr_{0.25}Ti_{0.5}Mn_{0.75}O_4$	600 °C 3h, 800 °C 2h
11	$LiY_{0.1}Fe_{0.4}Ti_{0.5}MnO_4$	600 °C 3h. 800 °C 2h
12	$LiY_{0.05}Fe_{0.45}Ti_{0.5}MnO_4$	800 °C 2h
13	$LiTb_{0.2}Fe_{0.4}Ti_{0.4}MnO_4$	600 °C 3h. 800 °C 2h
14	$LiY_{0.33}Fe_{0.33}Tb_{0.33}Ti_{0.33}Mn_{0.68}O_4$	800 °C 2h
15	$LiY_{0.1}Fe_{0.4}Tb_{0.1}Ti_{0.4}MnO_4$	800 °C 2h
16	$LiFe_{0.6}Ti_{0.6}Mn_{0.8}O_4$	600 °C 3h, 800 °C 2h
17	$LiMnTiO_4$	800 °C 2h
18	$LiFe_{0.5}Mn_{0.5}TiO_4$	600 °C 3h, 800 °C 2h
19	$LiFe_{0.7}Mn_{0.6}Ti_{0.7}O_4$	600 °C 3h, 800 °C 2h
20	$LiY_{0.1}Mn_{0.9}TiO_4$	800 °C 2h
21	$LiFeTiO_4$	800 °C 2h
22	$LiIn_{0.1}Mn_{0.9}TiO_4$	800 °C 2h
23	$LiY_{0.1}Fe_{0.9}TiO_4$	800 °C 2h
24	$LiIn_{0.1}Fe_{0.9}TiO_4$	800 °C 2h
25	$LiIn_{0.1}Mn_{0.1}Fe_{0.8}TiO_4$	800 °C 2h

Table 15 Lattice parameters a=b=c of the spinel crystal phase in the composition obtained as pure single phase.

Composition	a=b=c (Å)
$LiMn_2O_4$	8.173(1)
$LiFe_{0.5}Ti_{0.5}MnO_4$	8.2753(6)
$LiAl_{0.33}Fe_{0.33}Ti_{0.5}Mn_{0.84}O_4$	8.206(3)
$LiFe_{0.33}Cr_{0.33}Ti_{0.5}Mn_{0.84}O_4$	8.251(2)
$LiFe_{0.6}Ti_{0.6}Mn_{0.8}O_4$	8.2908(8)
$LiMnTiO_4$	8.335(1)
$LiFe_{0.5}Mn_{0.5}TiO_4$	8.293(1)
$LiFe_{0.7}Mn_{0.6}Ti_{0.7}O_4$	8.3129(9)
$LiFeTiO_4$	8.369(2)

Table 16 Lattice parameters a=b=c of the spinel crystal phase in the composition obtained as multiphase.

Composition	a=b=c (Å)
$LiMnYO4$	/
$LiY_{0.33}Fe_{0.33}Mn_{1.84}O_4$	8.241(3)
$LiFe_{0.33}Y_{0.33}Ti_{0.5}Mn_{0.84}O_4$	8.294(3)
$LiFe_{0.5}Ti_{0.33}Zr_{0.33}Mn_{0.84}O_4$	8.265(4)
$LiY_{0.25}Al_{0.25}Fe_{0.25}Ti_{0.5}Mn_{0.75}O_4$	8.216(3)
$LiY_{0.25}Fe_{0.25}Cr_{0.25}Ti_{0.5}Mn_{0.75}O_4$	8.2363(1)
$LiY_{0.1}Fe_{0.4}Ti_{0.5}MnO_4$	8.2859(9)
$LiY_{0.05}Fe_{0.45}Ti_{0.5}MnO_4$	8.2696(7)
$LiTb_{0.2}Fe_{0.4}Ti_{0.4}MnO_4$	8.255(1)
$LiY_{0.33}Fe_{0.33}Tb_{0.33}Ti_{0.33}Mn_{0.68}O_4$	8.192(6)
$LiY_{0.1}Fe_{0.4}Tb_{0.1}Ti_{0.4}MnO_4$	8.268(1)
$LiY_{0.1}Mn_{0.9}TiO_4$	8.318(1)
$LiIn_{0.1}Mn_{0.9}TiO_4$	8.3072(9)
$LiY_{0.1}Fe_{0.9}TiO_4$	8.355(7)
$LiIn_{0.1}Fe_{0.9}TiO_4$	8.373(2)
$LiIn_{0.1}Mn_{0.1}Fe_{0.8}TiO_4$	8.372(4)

Table 17 Ionic conductivity ($\frac{S}{cm}$) of $LiFe_{0.5}Ti_{0.5}MnO_4$, $LiFe_{0.5}Mn_{0.5}TiO_4$, $LiFe_{0.6}Ti_{0.6}Mn_{0.8}O_4$ and $LiFe_{0.7}Mn_{0.6}Ti_{0.7}O_4$ measured at 25 °C.

Composition	σ_{ion} ($\frac{S}{cm}$)
$LiFe_{0.5}Ti_{0.5}MnO_4$	$2.84 \cdot 10^{-5}$
$LiFe_{0.5}Mn_{0.5}TiO_4$	$5.74 \cdot 10^{-6}$
$LiFe_{0.6}Ti_{0.6}Mn_{0.8}O_4$	$2.43 \cdot 10^{-5}$
$LiFe_{0.7}Mn_{0.6}Ti_{0.7}O_4$	$8.73 \cdot 10^{-6}$

7. Figures
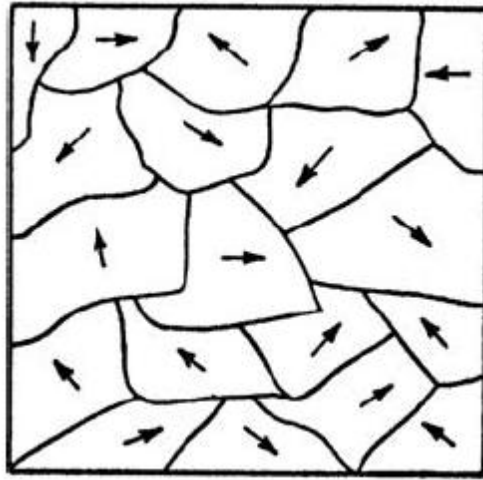
Figure 1 Magnetic domain in a polycrystalline material[139].

Figure 2 Gradual rotation of 180 ° of the Bloch walls.

Figure 3 Single magnetic domain.
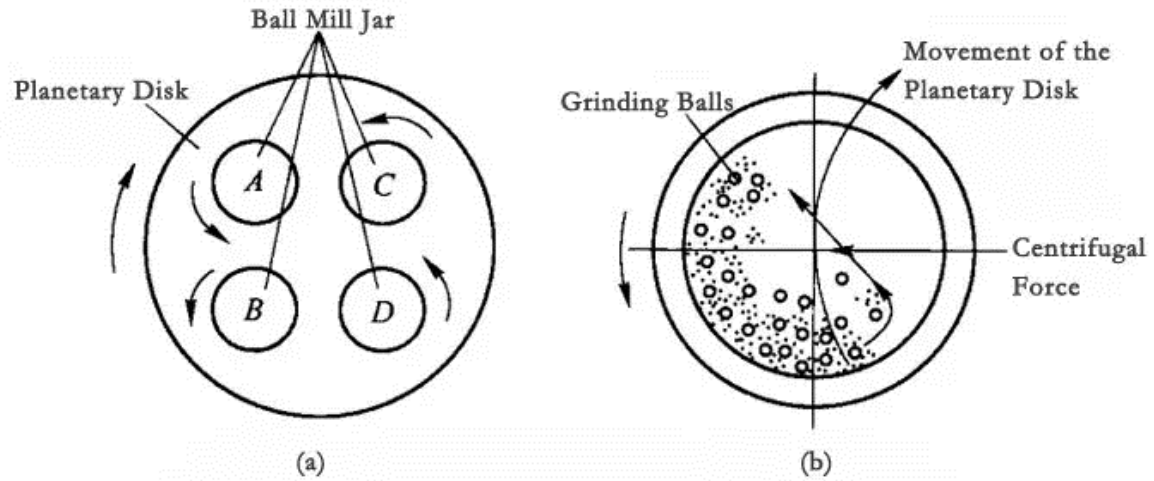
Figure 4 Schematic illustration of the working principle of the planetary ball mill. The disk and the grinding jars rotate in opposite direction.
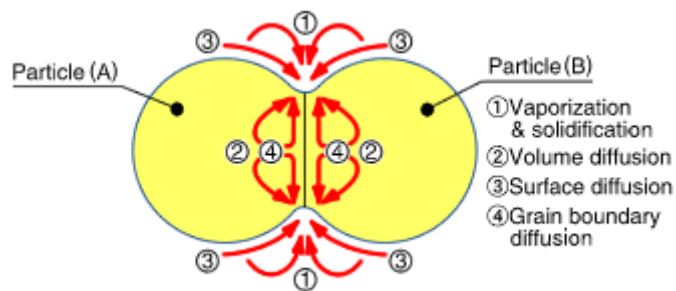
Figure 5 Scheme of the diffusion phenomena during the sintering process [140].
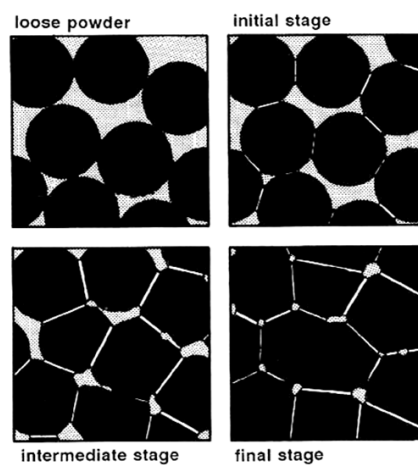
Figure 6 Schematic illustration of the particles densification during the sintering process[140].
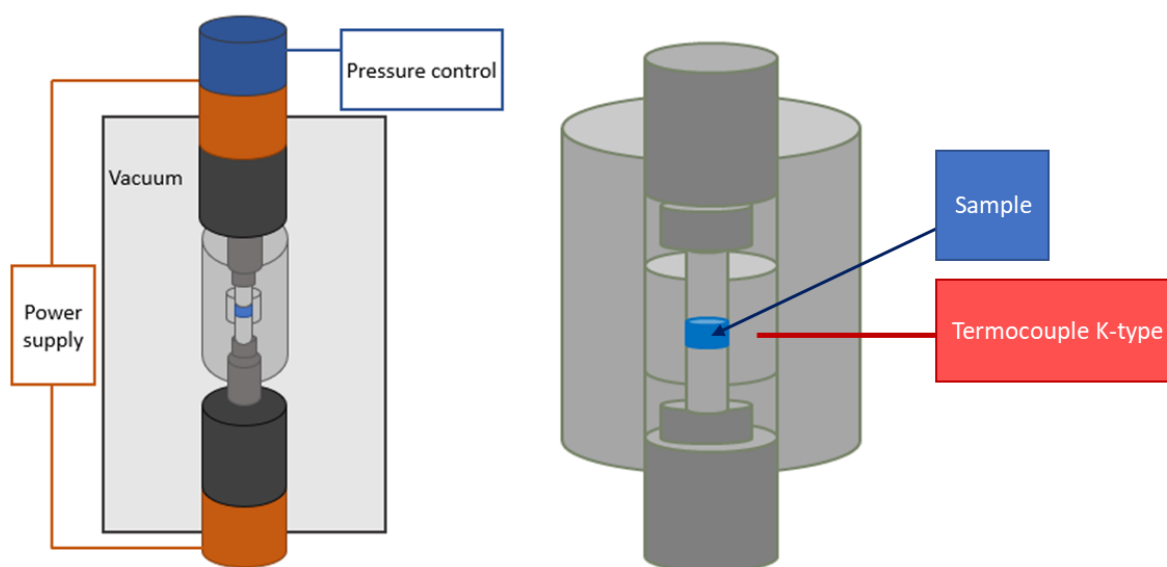
Figure 7 Schematic illustration of the HP-FAST apparatus.
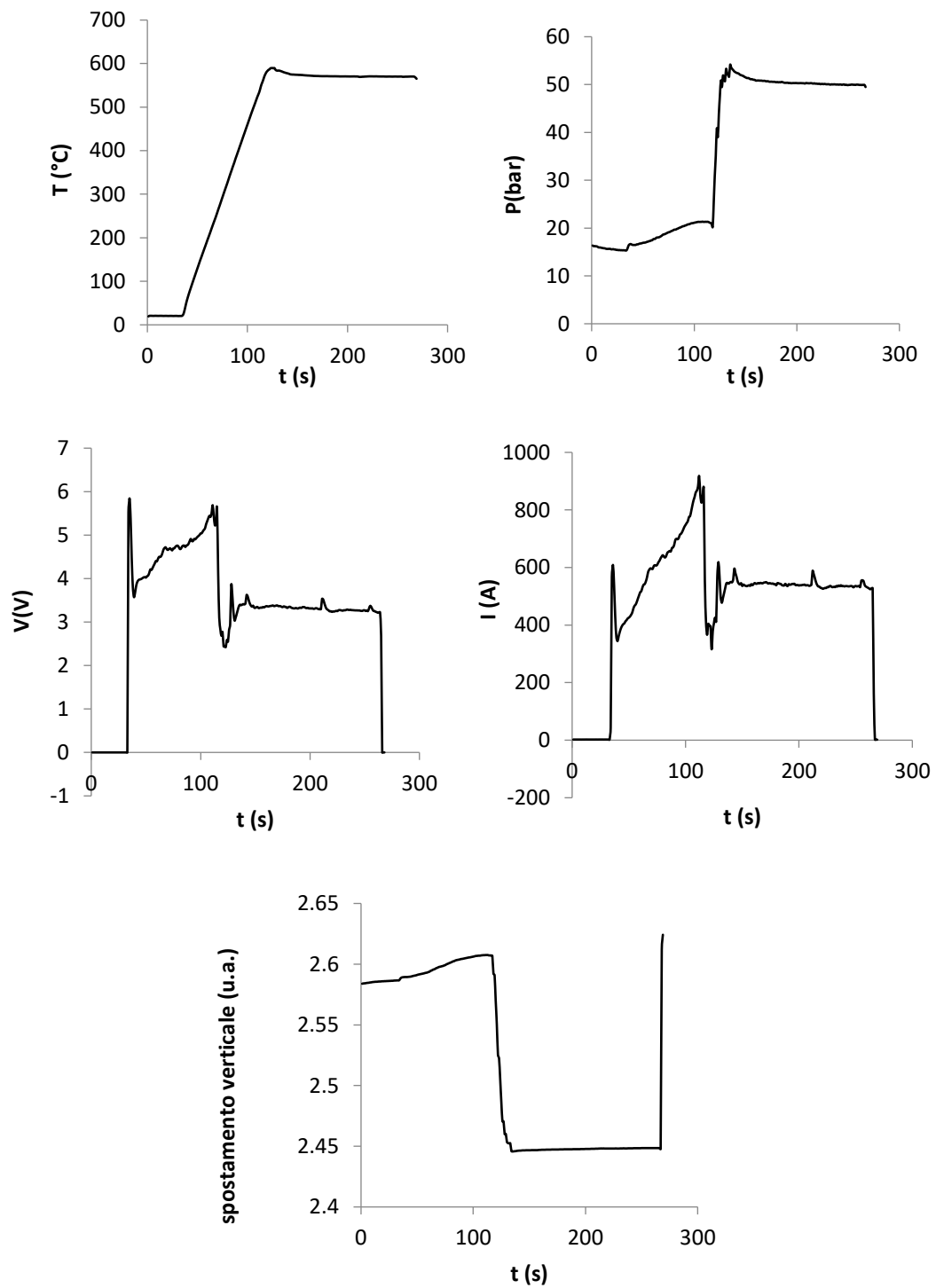
Figure 8 Trend of the temperature, pressure, applied voltage, current intensity and displacement during a typical sintering process.

Figure 9 Instrumental apparatus for the density measurements.
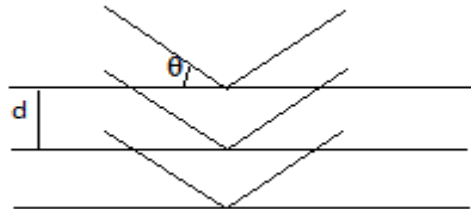
Figure 10 Representation of a parallel planes' family hit by a parallel X-ray beam.
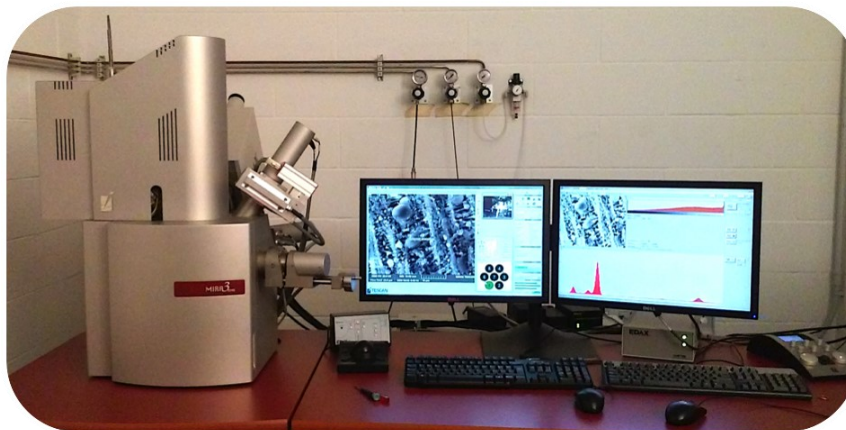
Figure 11 Microscope TESCAN Mira 3 XMU of CISRiC laboratory in Pavia[141].
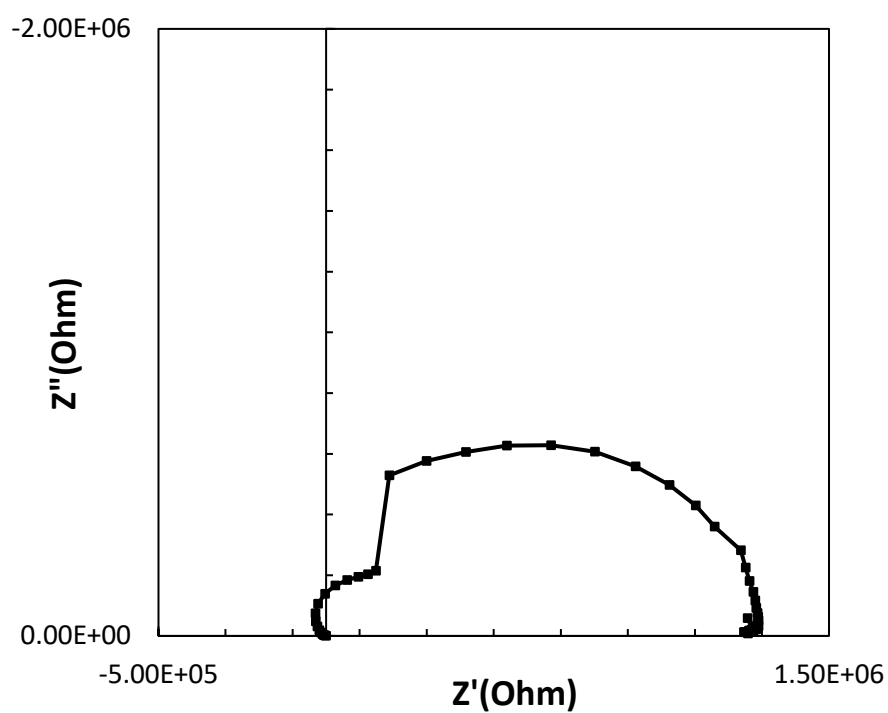
Figure 12 Example of a Z'' vs. Z' graph on an impedance spectroscopy measure.
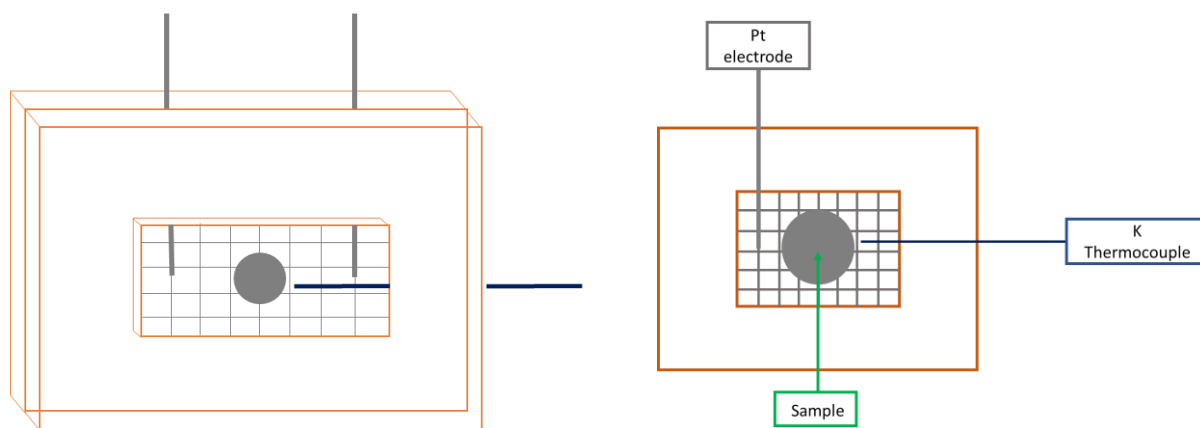
Figure 13 Set-up of the electrochemical measure cell.
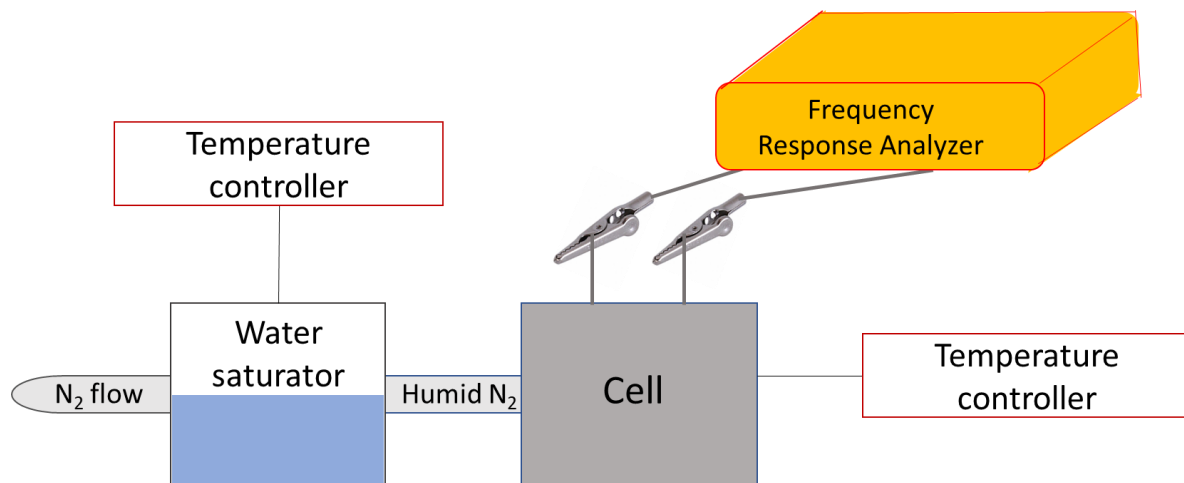
Figure 14 Schematic representation of the Test-Stand.
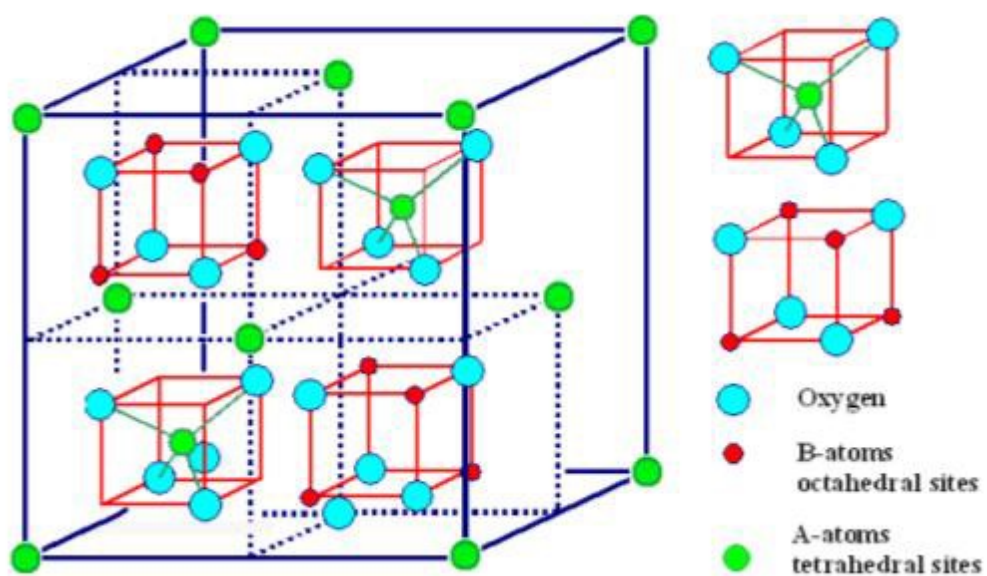
Figure 15 Crystal structure of the direct spinel AB$_2$O$_4$, the red cubes are contained also in the remanent middle of the unit cell [10].

Ione	Numero di elettroni	Configurazione elettronica degli orbitali $3d$					Momento magnetico ionico (magnetoni di Bohr)
Fe^{3+}	23	↑	↑	↑	↑	↑	5
Mn^{2+}	23	↑	↑	↑	↑	↑	5
Fe^{2+}	24	↑↓	↑	↑	↑	↑	4
Co^{2+}	25	↑↓	↑↓	↑	↑	↑	3
Ni^{2+}	26	↑↓	↑↓	↑↓	↑	↑	2
Cu^{2+}	27	↑↓	↑↓	↑↓	↑↓	↑	1
Zn^{2+}	28	↑↓	↑↓	↑↓	↑↓	↑↓	0

Figure 16 Electronic disposition of the 3d orbitals of the cations in ferrites [139].
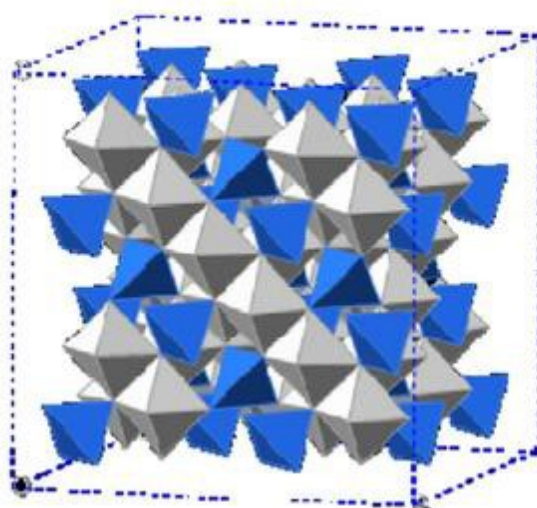
Figure 17 CoFe$_2$O$_4$ crystal structure.
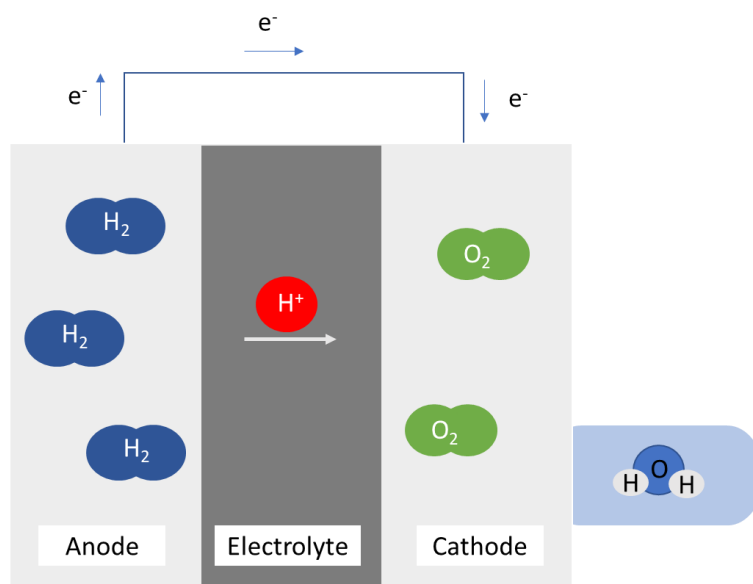
Figure 18 Scheme of a Protonic fuel cell.
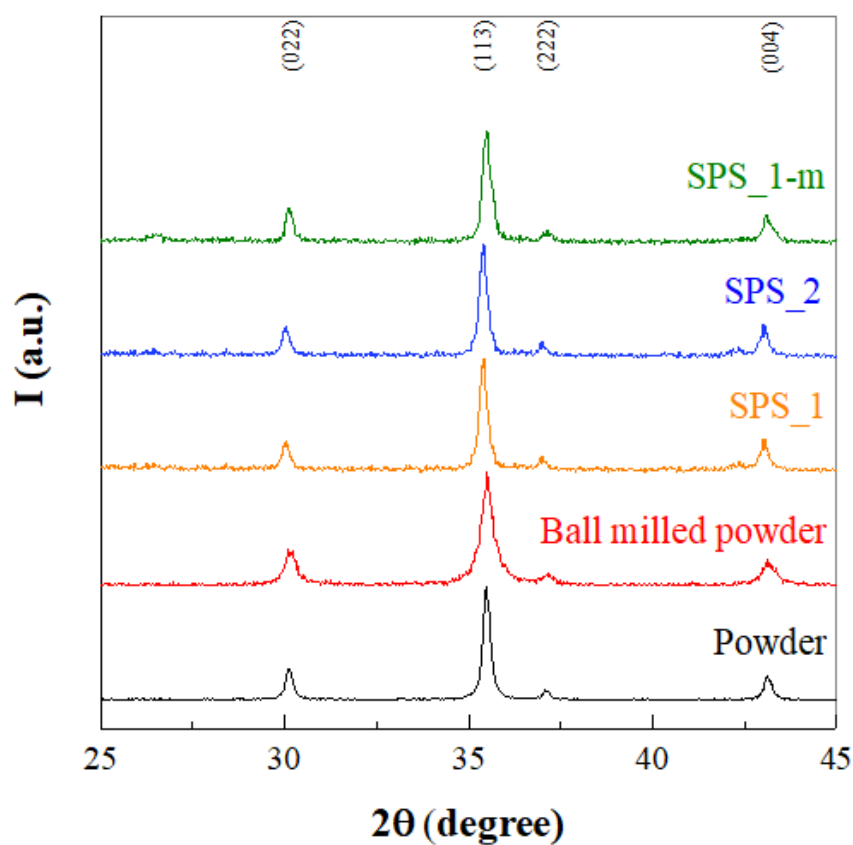
Figure 19 XRD patterns of the cobalt ferrite nanopowders and sintered samples.
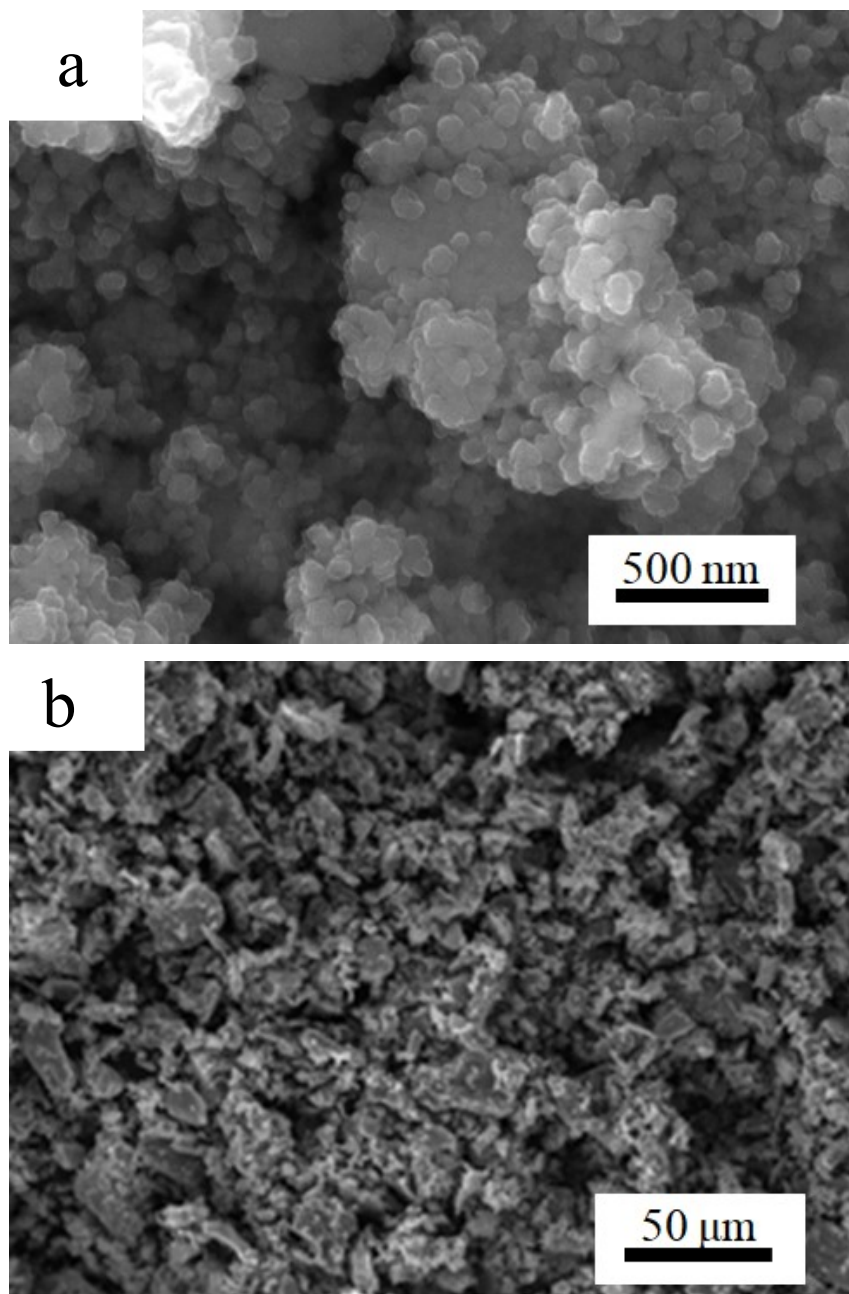
Figure 20 *SEM images (a-magnetization 100 kx b-magnetization 1kx) of the cobalt ferrite nanopowder.*

c

10 µm

d

10 µm
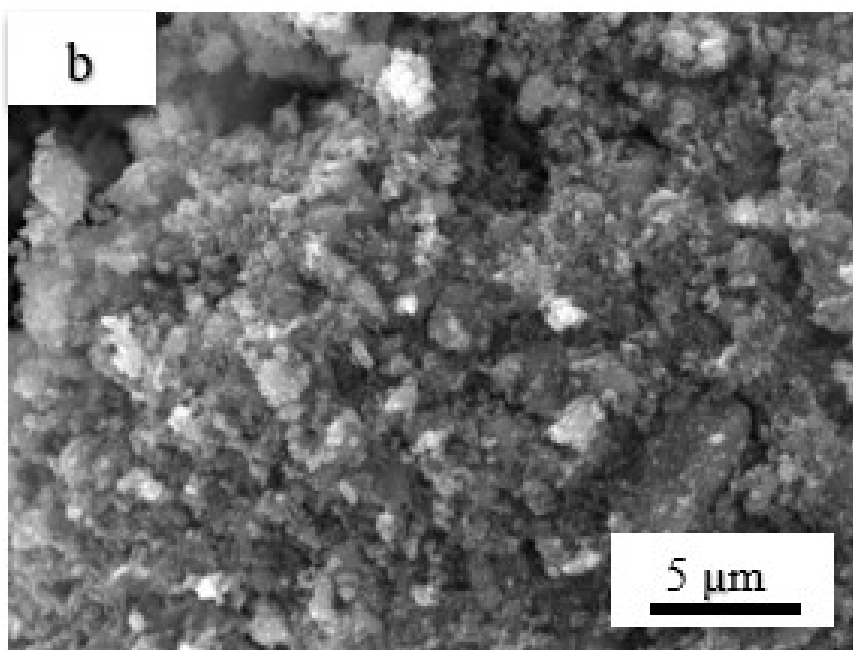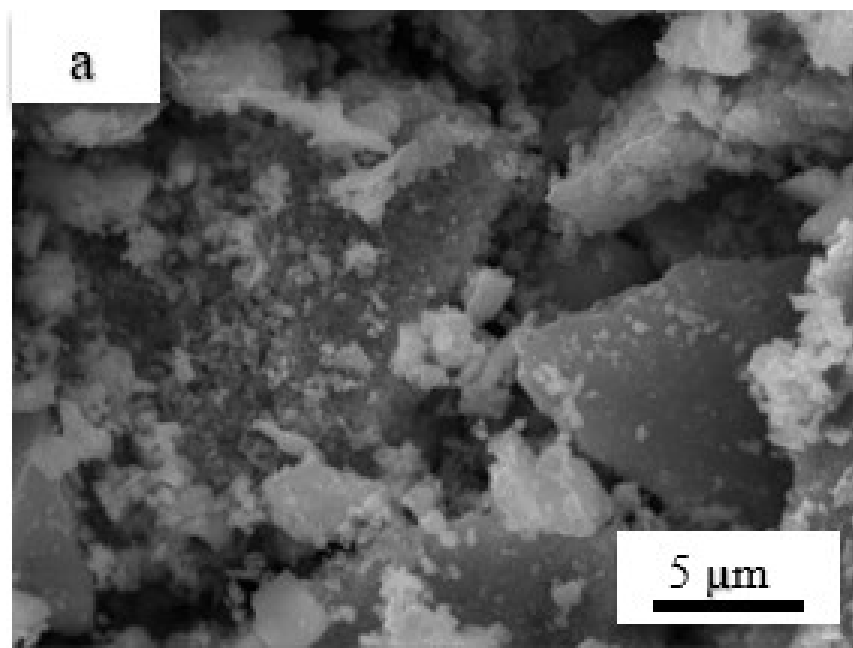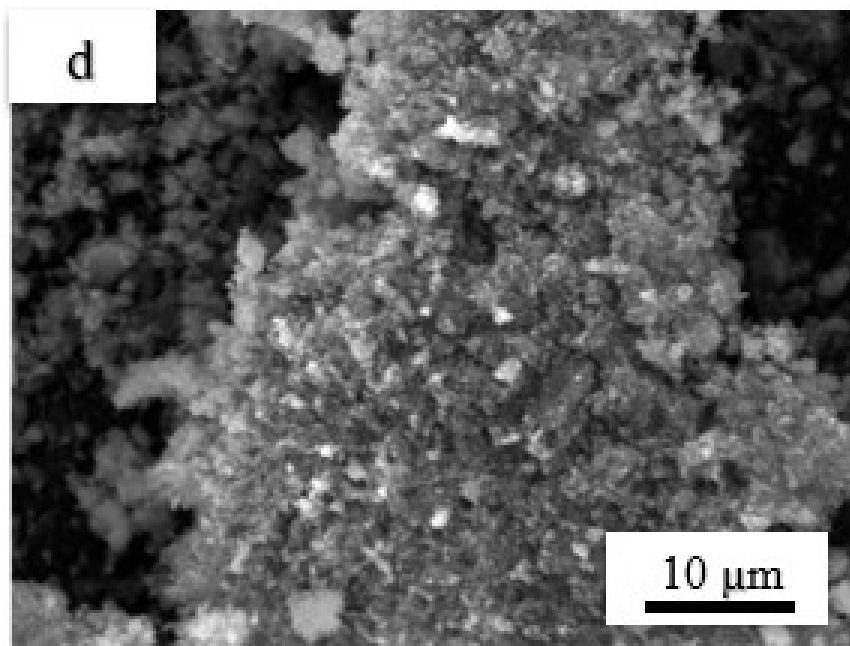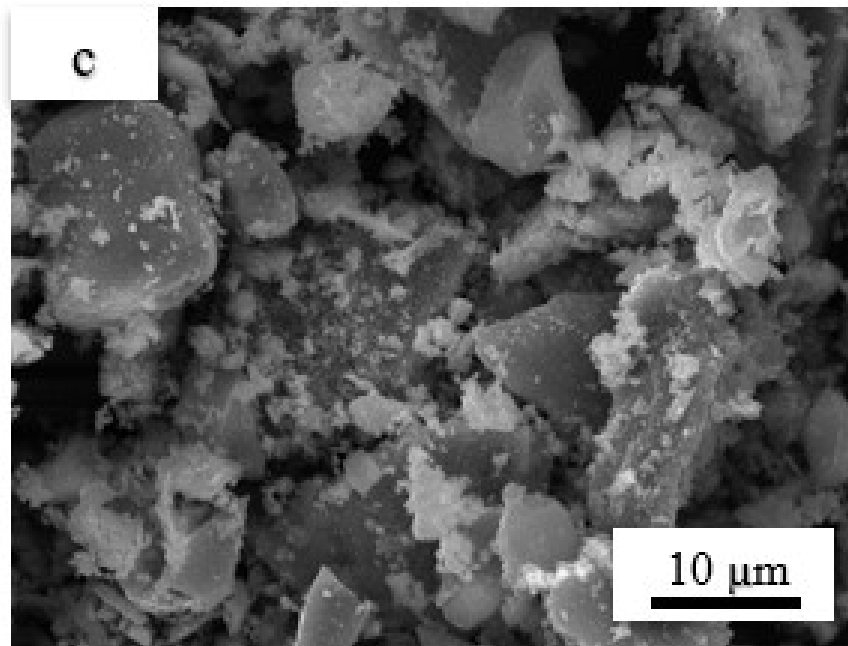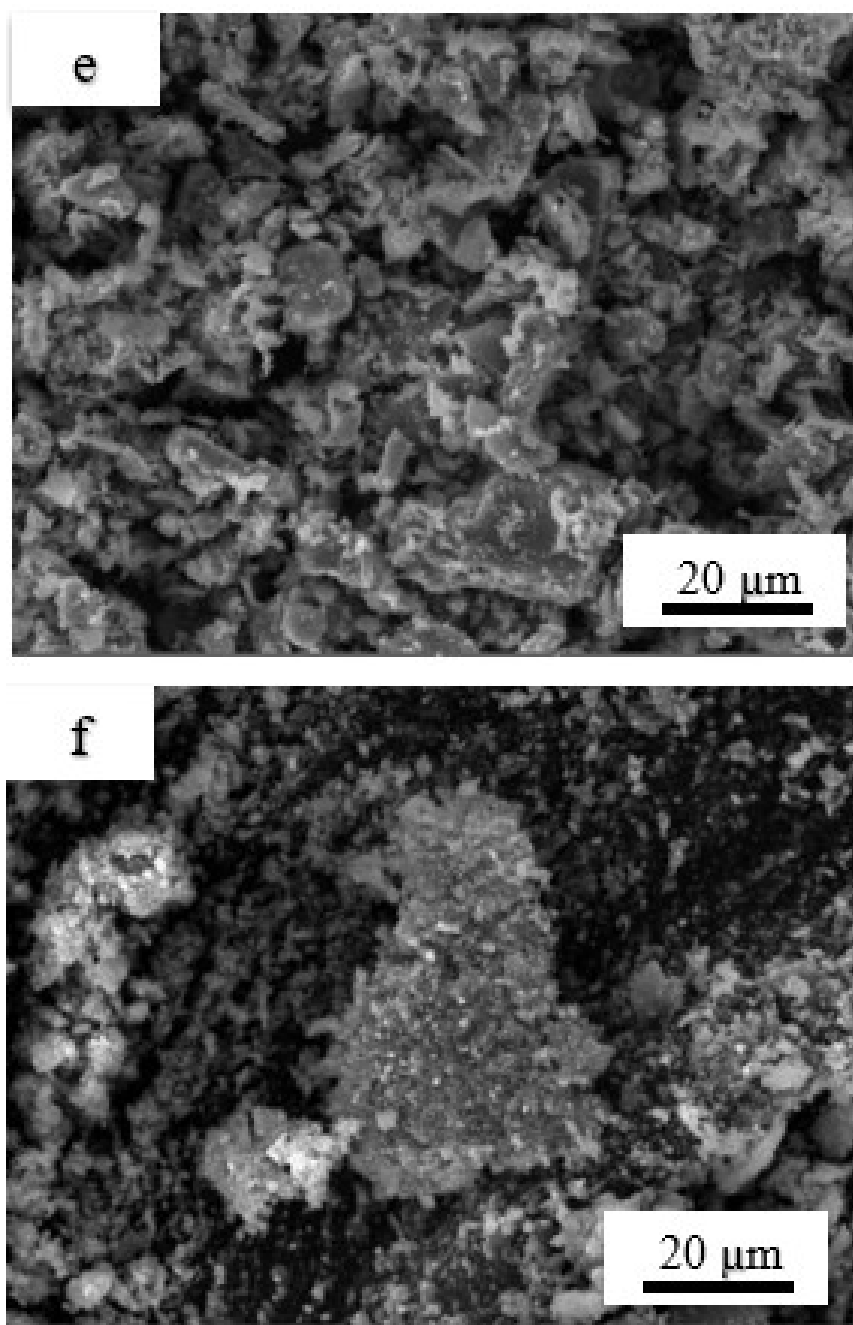
Figure 21 SEM images of the cobalt ferrite nanopowder as-synthesized (a-c-e) and the milled cobalt ferrite nanopowder (b-d-f).
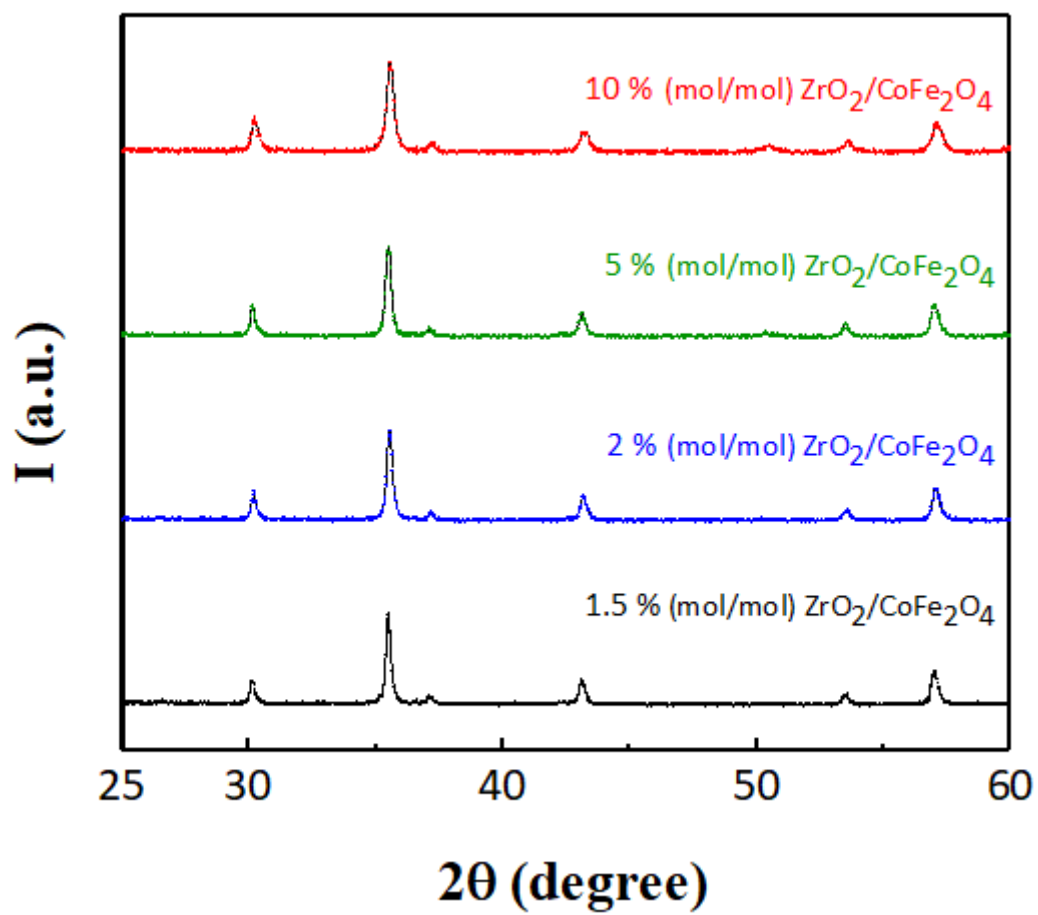
Figure 22 XRD patterns of the composites sintered samples CoFe$_2$O$_4$-ZrO$_2$.
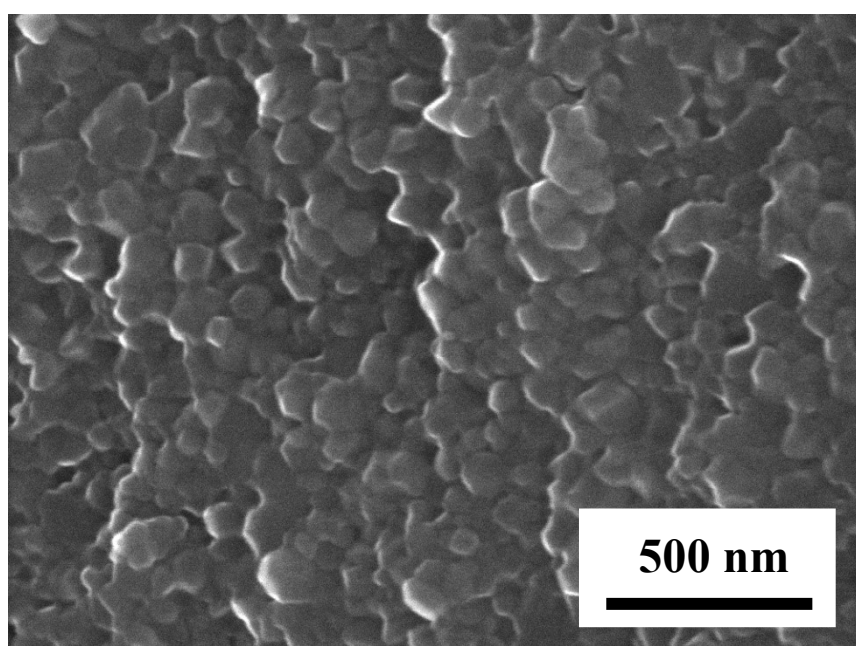
Figure 23 SEM image of the 1.5 % (g/g) ZrO$_2$-CoFe$_2$O$_4$ sintered sample.
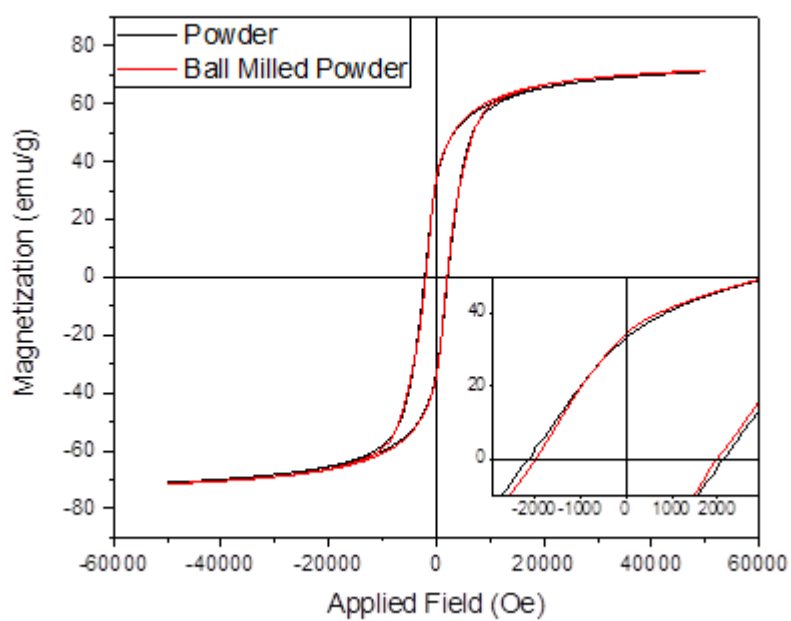
Figure 24 Hysteresis loop of the CoFe$_2$O$_4$ nanopowder.
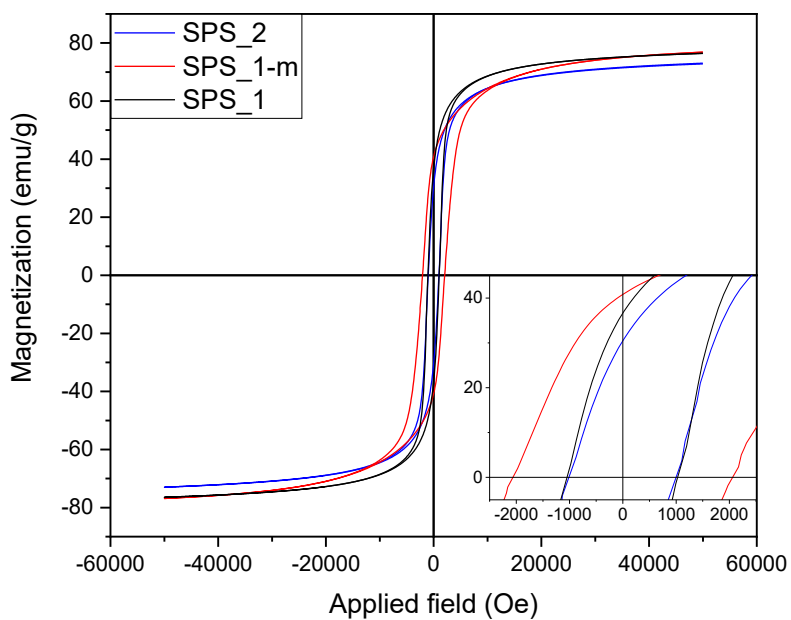
Figure 25 Hysteresis loop of the cobalt ferrite sintered samples SPS_1_575°C, SPS_2_575°C and SPS_1-m_575°C.
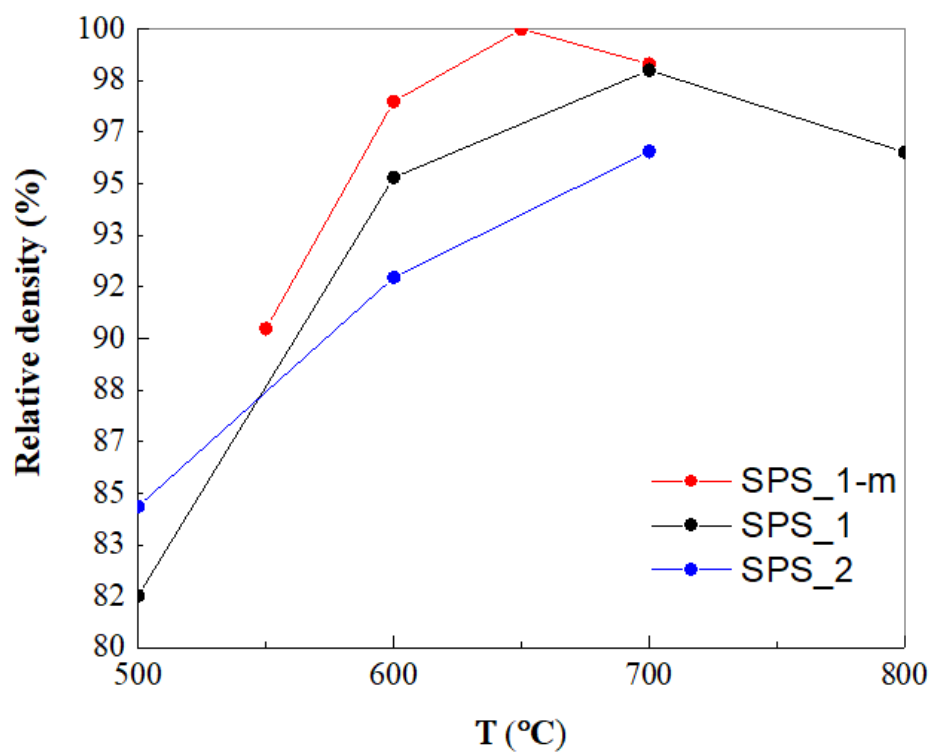
Figure 26 Relative density of the sintered samples SPS_1, SPS_2 and SPS_1-m as a function of the sintering temperature.
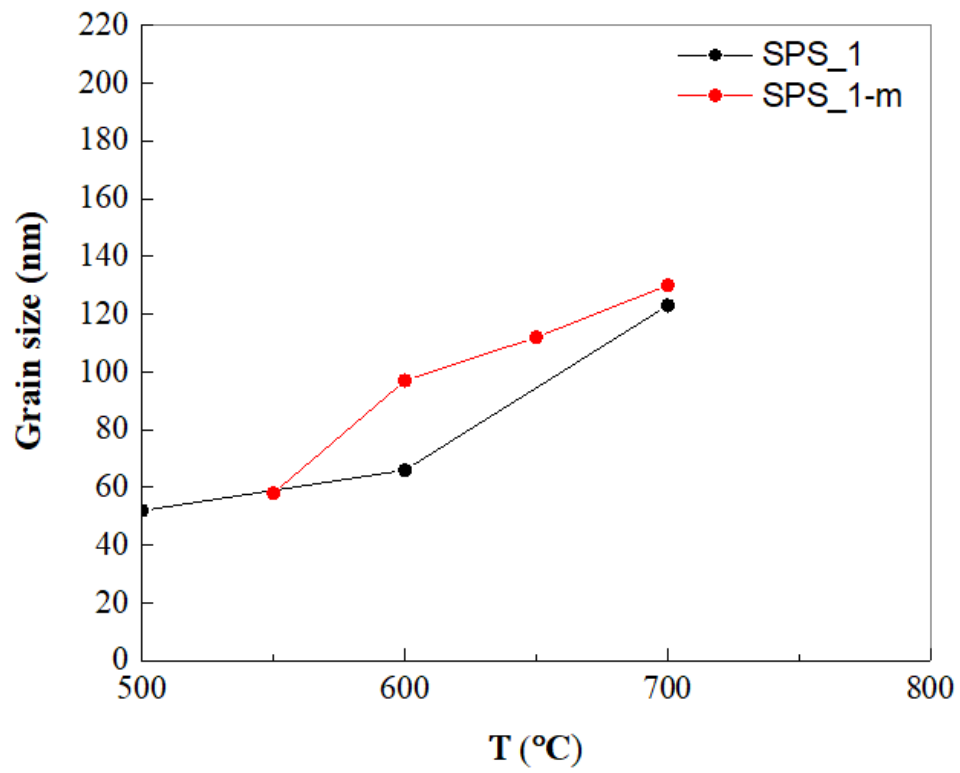
Figure 27 Grain size evaluated with SEM analysis of the sintered samples SPS_1 and SPS_1-m as a function of the sintering temperature.
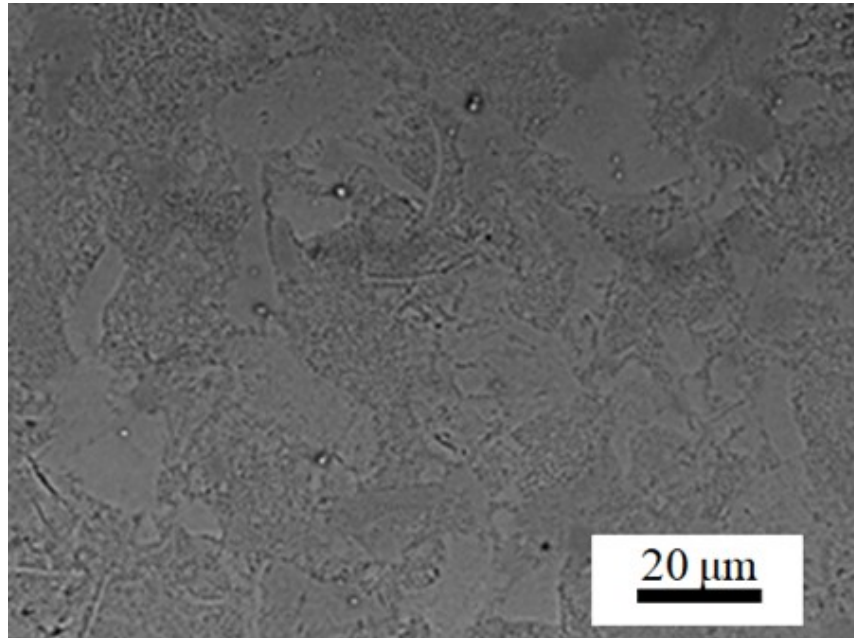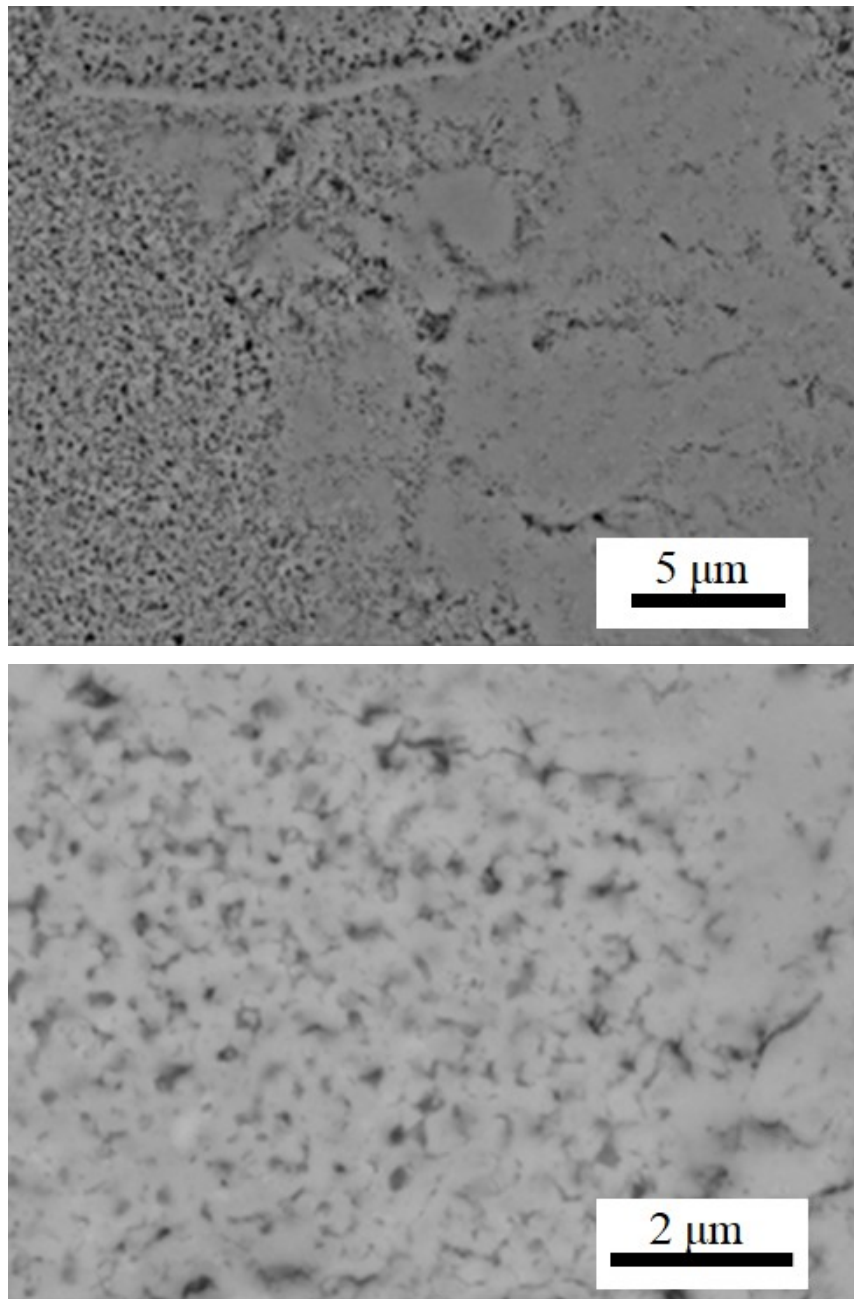
Figure 28 SEM images backscattered of the sintered sample SPS_1_575°C.
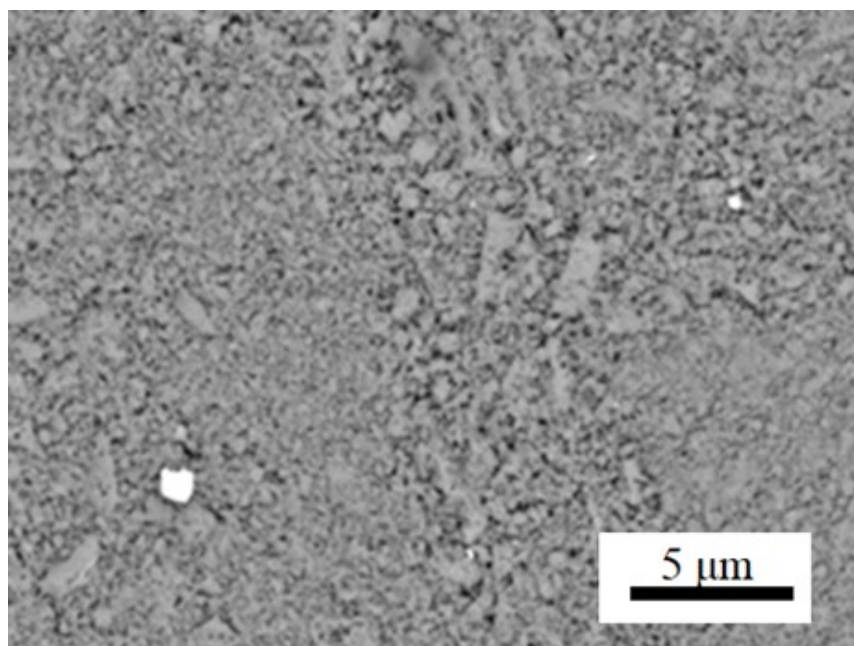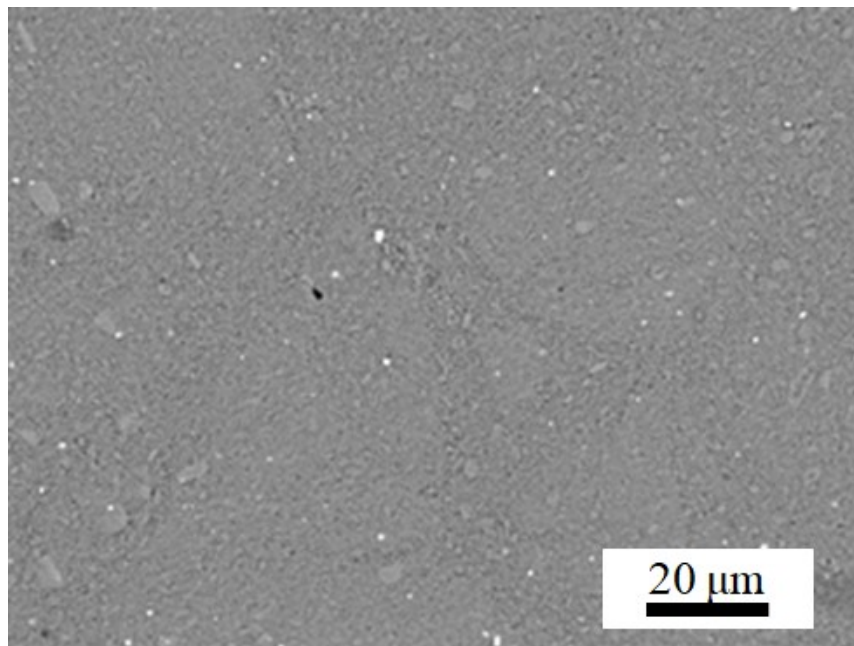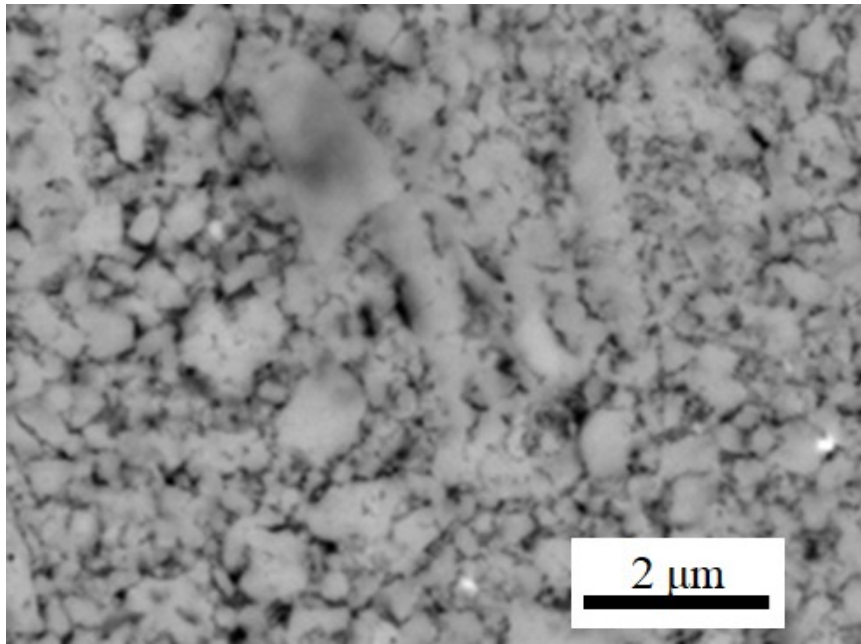
Figure 29 SEM images backscattered of the sintered sample SPS_1-m_575°C.
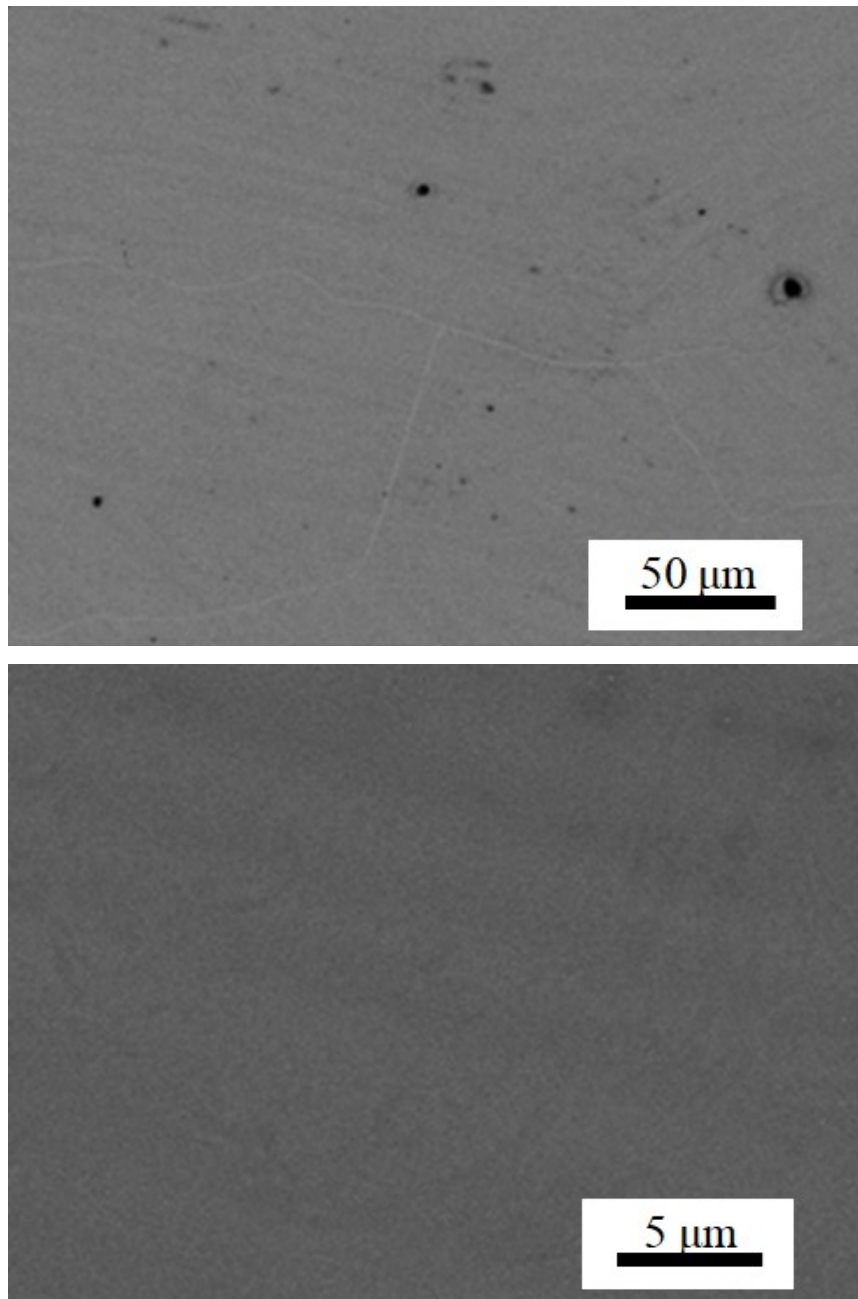
Figure 30 SEM images backscattered of the sintered sample SPS_2_575°C.
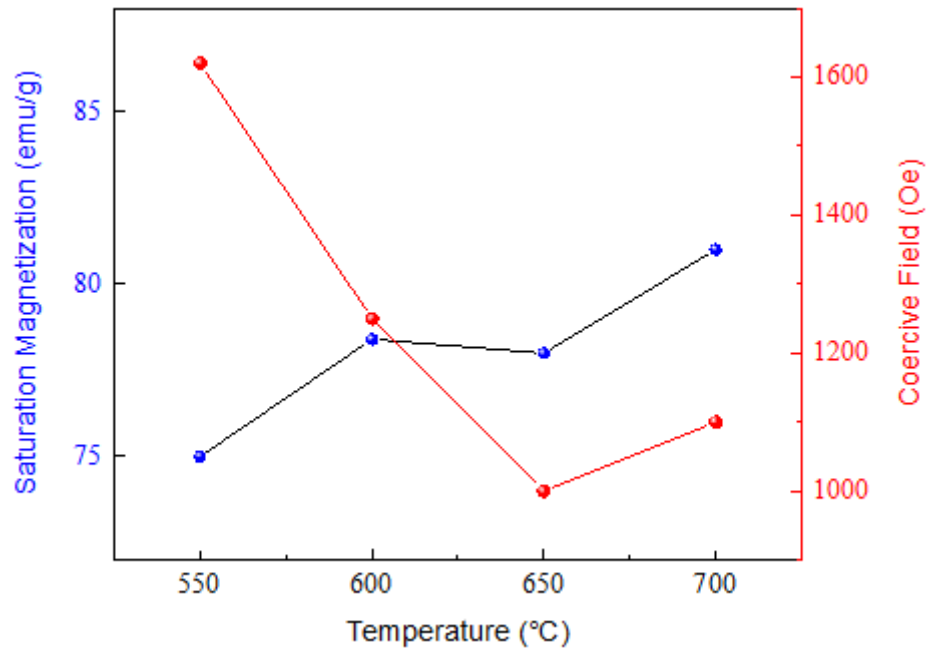
Figure 31 Coercive field and saturation magnetization for the sintered sample of the series SPS_1-m as a function of the sintering temperature.
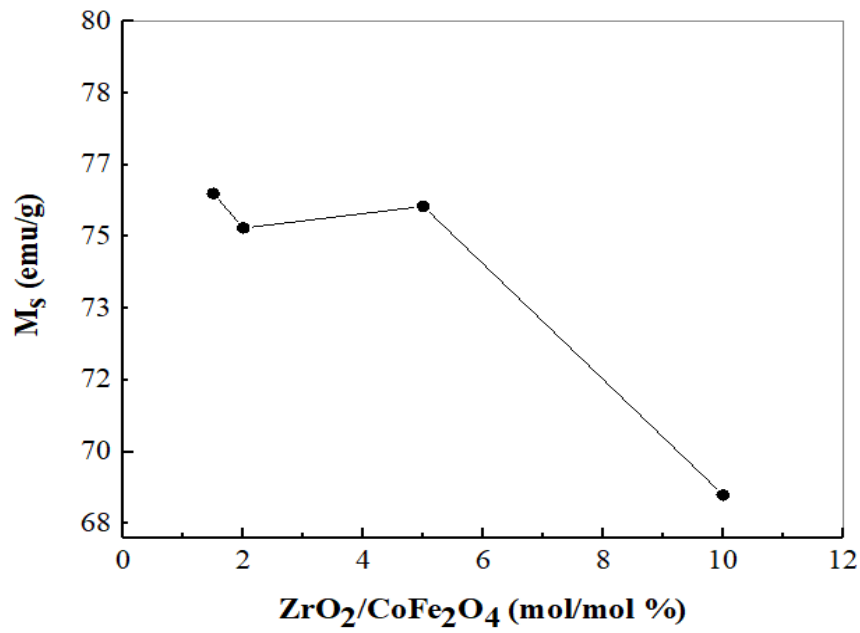
Figure 32 Saturation magnetization as a function of the ZrO₂/CoFe₂O₄ molar ratio.
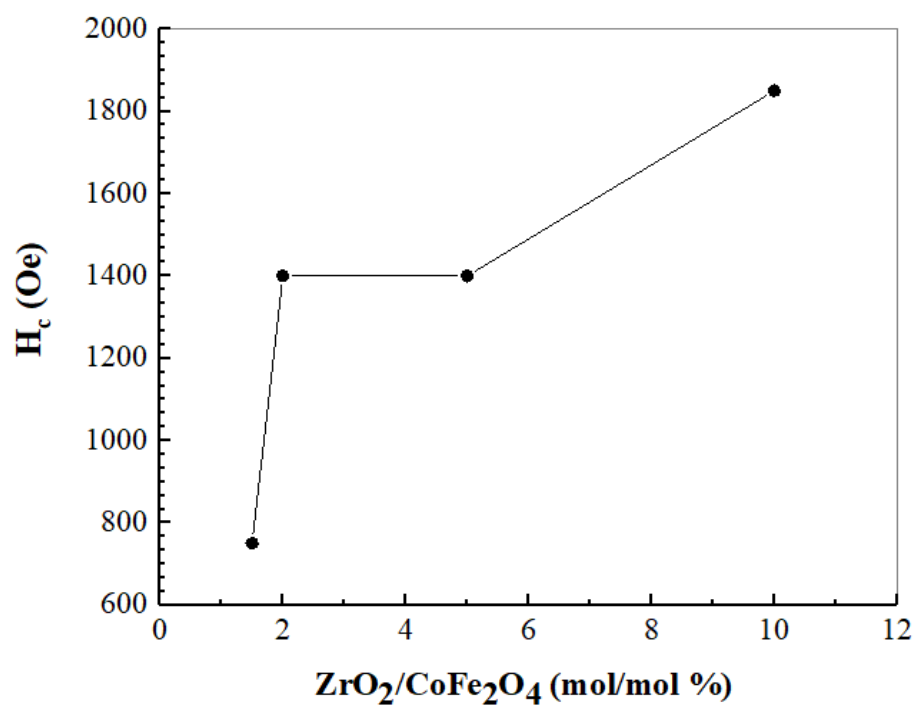
Figure 33 Saturation magnetization as a function of the ZrO$_2$/CoFe$_2$O$_4$ molar ratio.
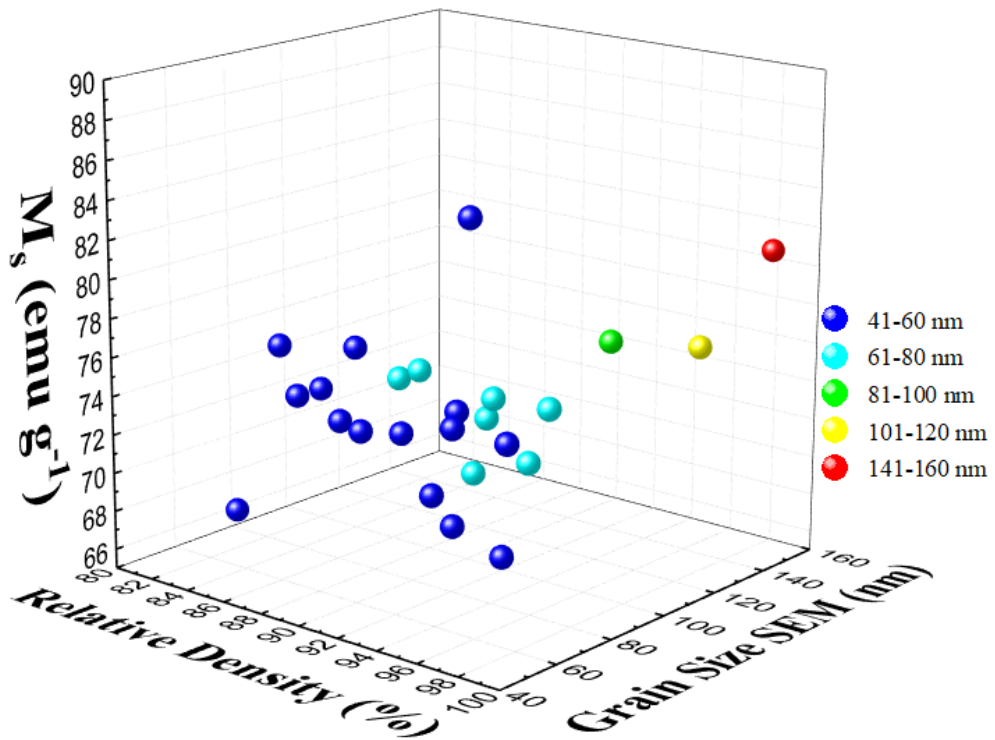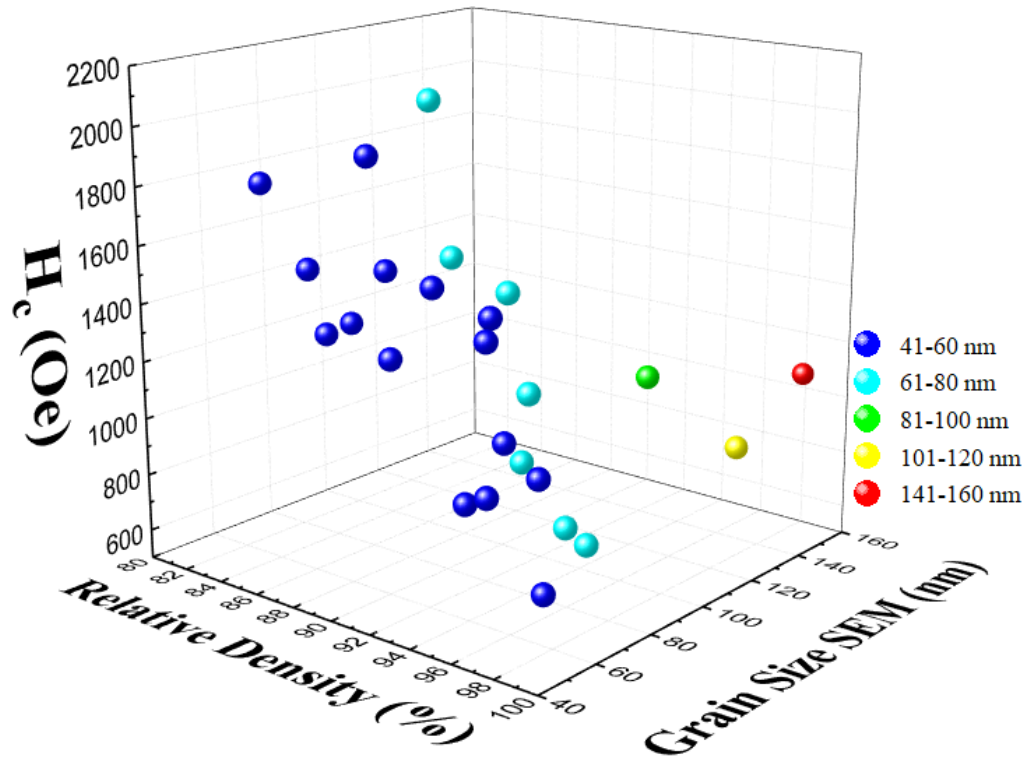
Figure 34 Coercive field and Saturation magnetization for all the sintered samples produced in this work as a function of relative density and grain size.
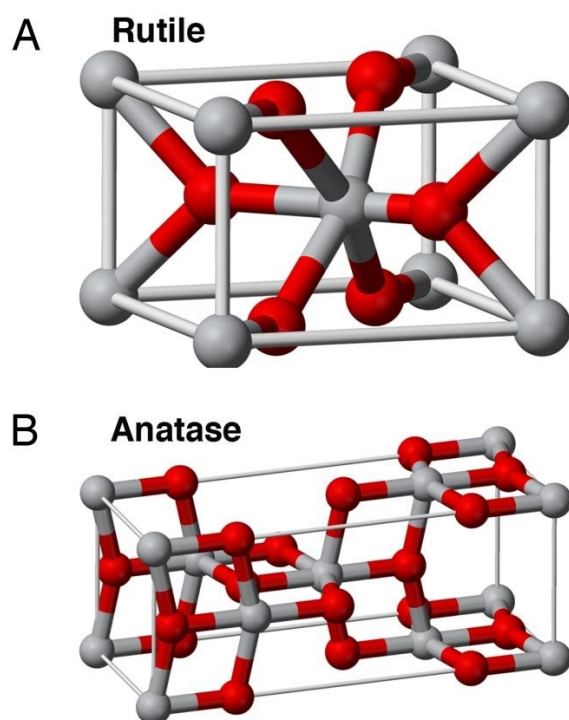
Figure 35 Representation of Rutile and Anatase unit cells.
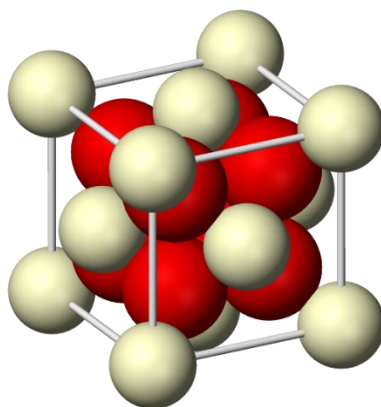
Figure 36 Representation of CeO$_2$ unit cell.
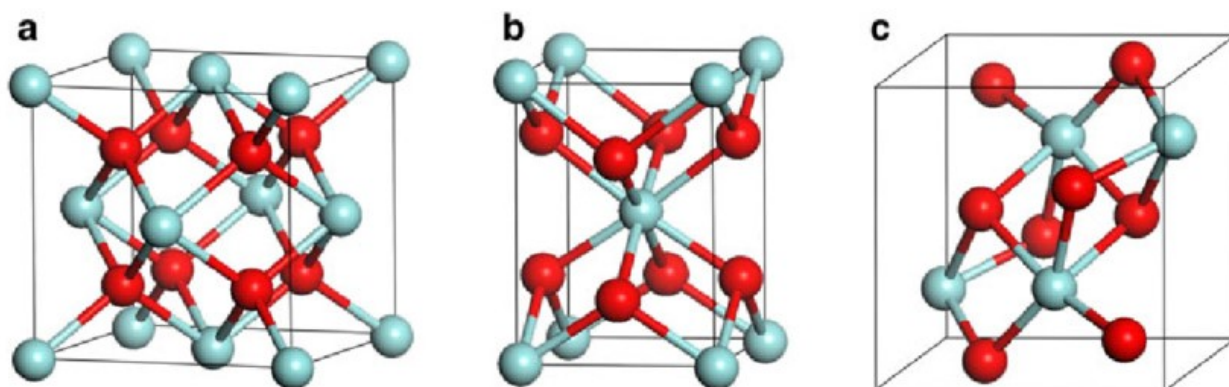
Figure 37 Representation of the unit cells of ZrO$_2$ polymorphs.
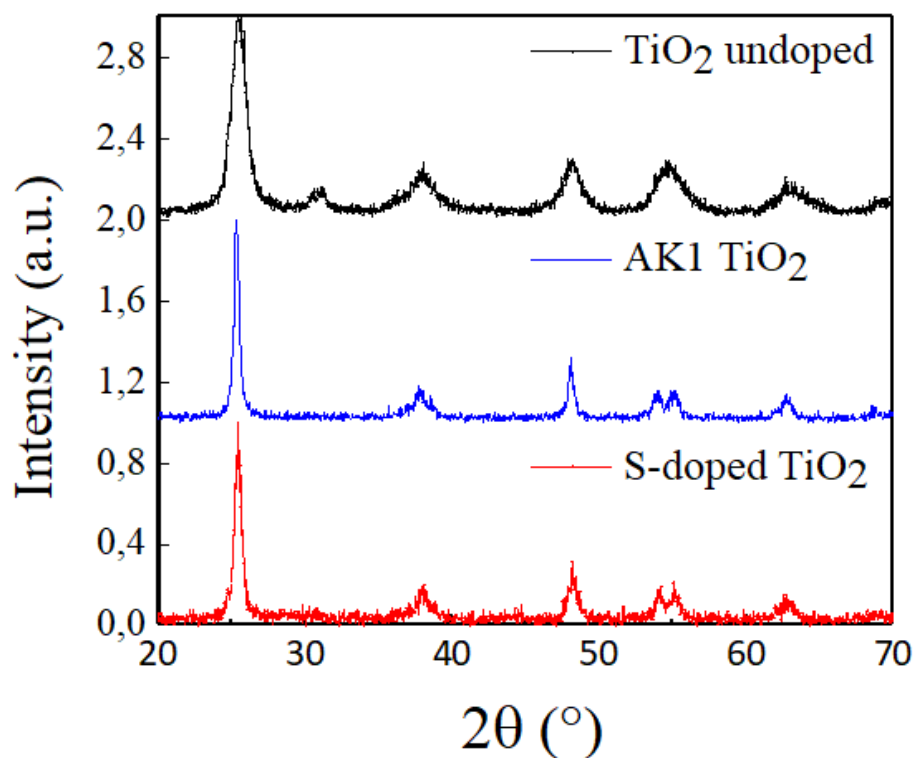
Figure 38 XRD patterns of the TiO₂ undoped powder, AK1 TiO₂ powder and S-doped TiO₂ powder.
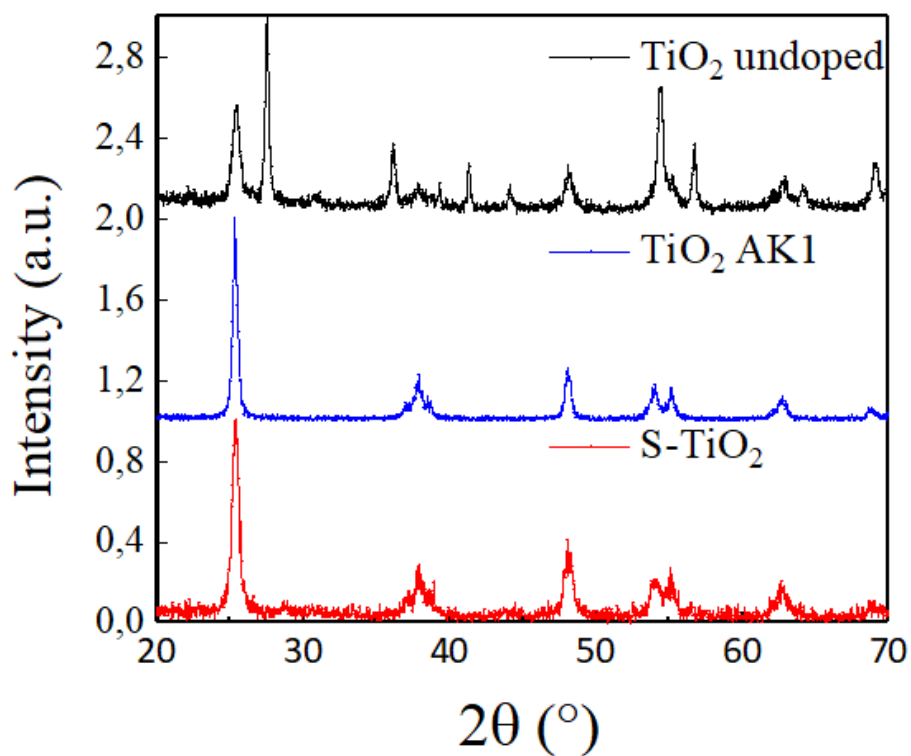
Figure 39 XRD of the TiO₂ undoped sintered sample, the TiO₂ AK1 sintered sample and the S-TiO₂ sintered sample.
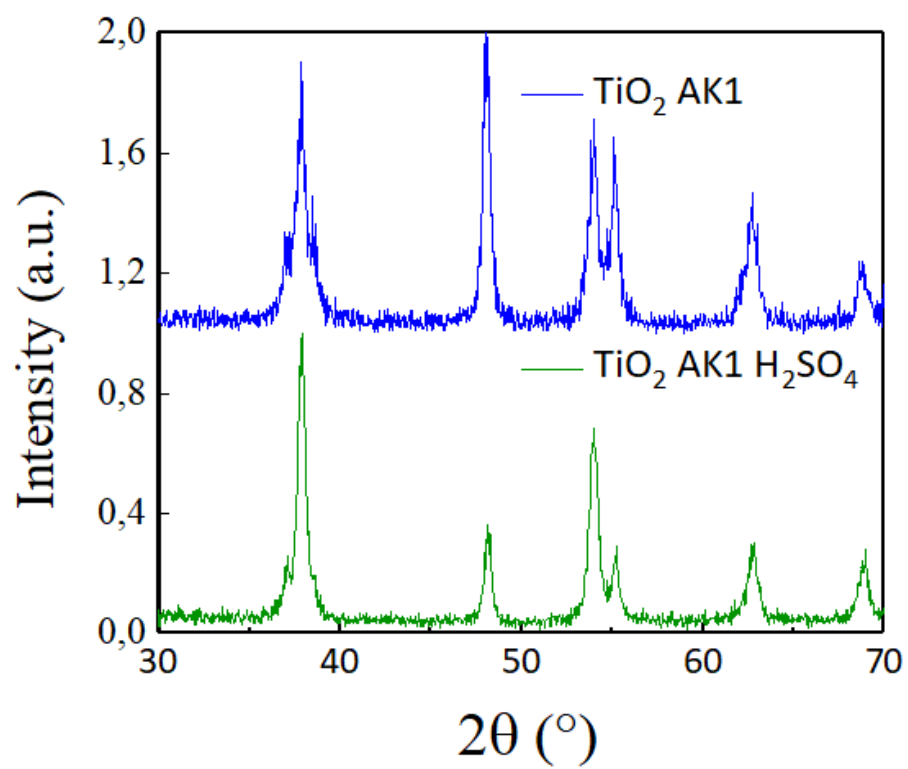
Figure 40 XRD of AK1 not immersed and immersed in H_2SO_4 sintered sample.
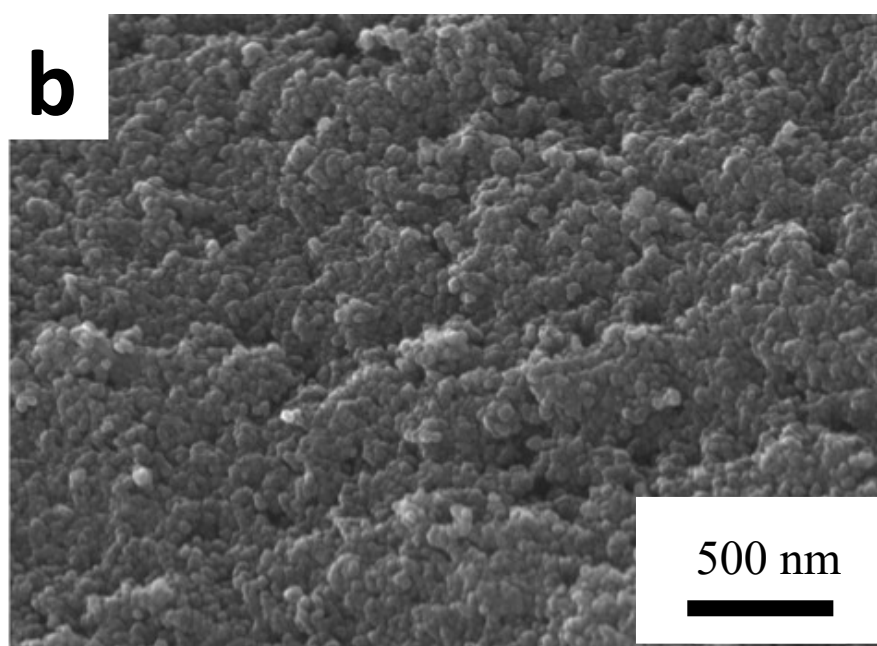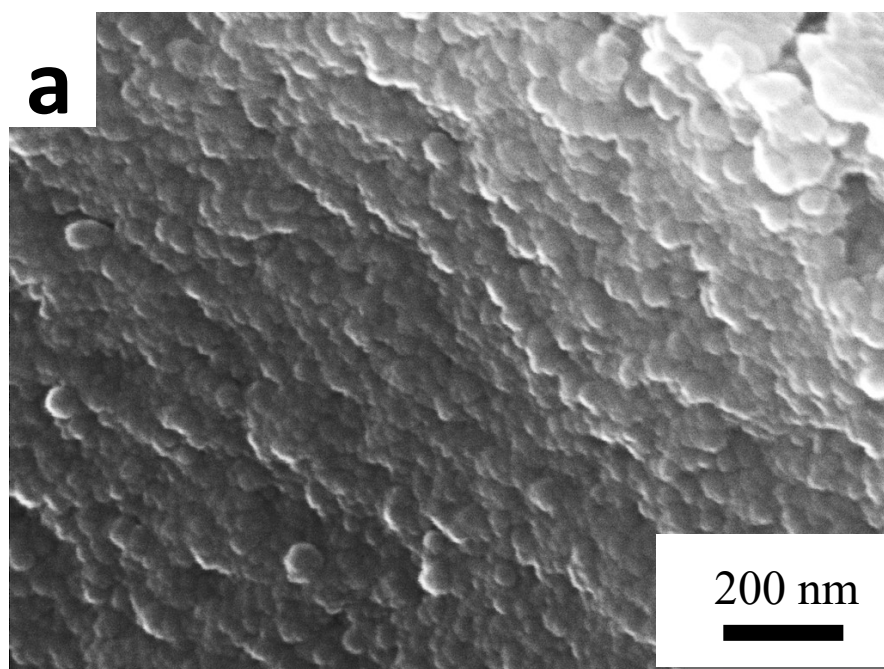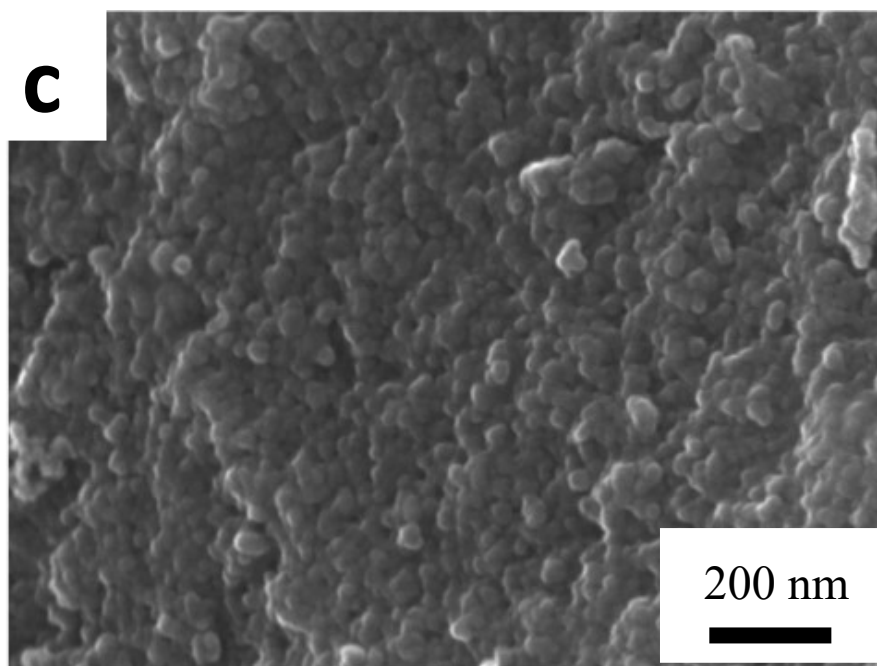
Figure 41 SEM images of S-TiO₂ sintered sample (a), TiO₂ AK1 sintered sample (b) and TiO₂ undoped sintered sample (c).
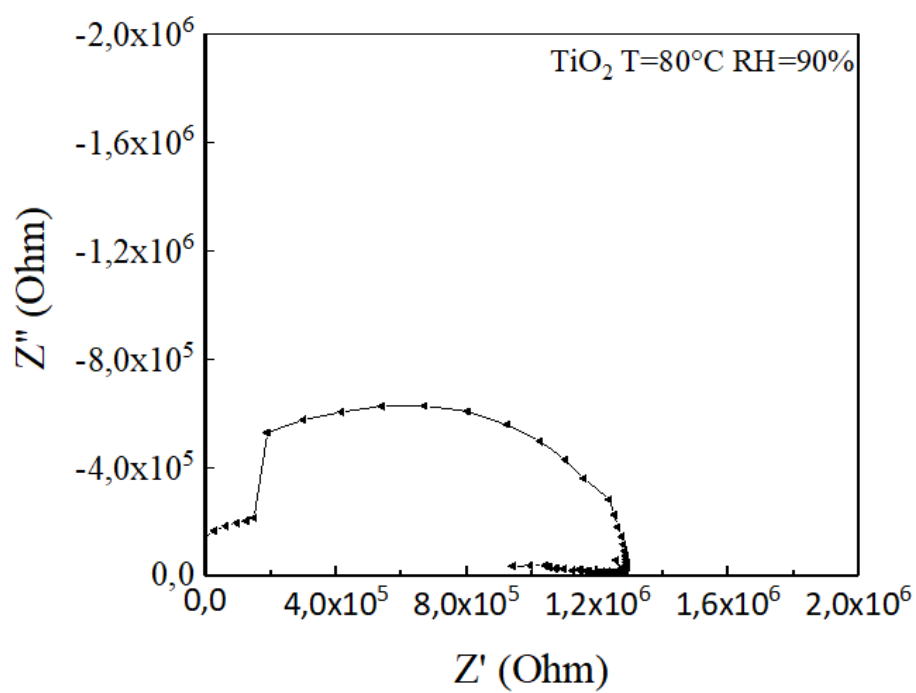
Figure 42 Impedance spectrum of TiO₂ at 80 °C and 90 % of RH.
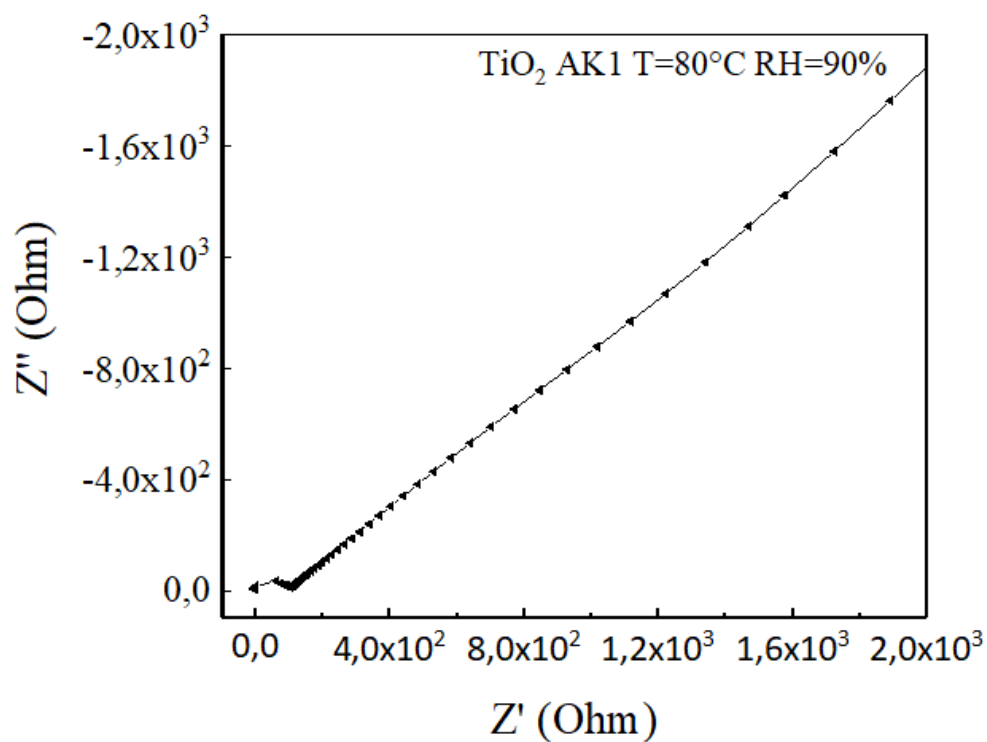
Figure 43 Impedance spectrum of TiO$_2$ AK1 at 80°C and 90% of RH.
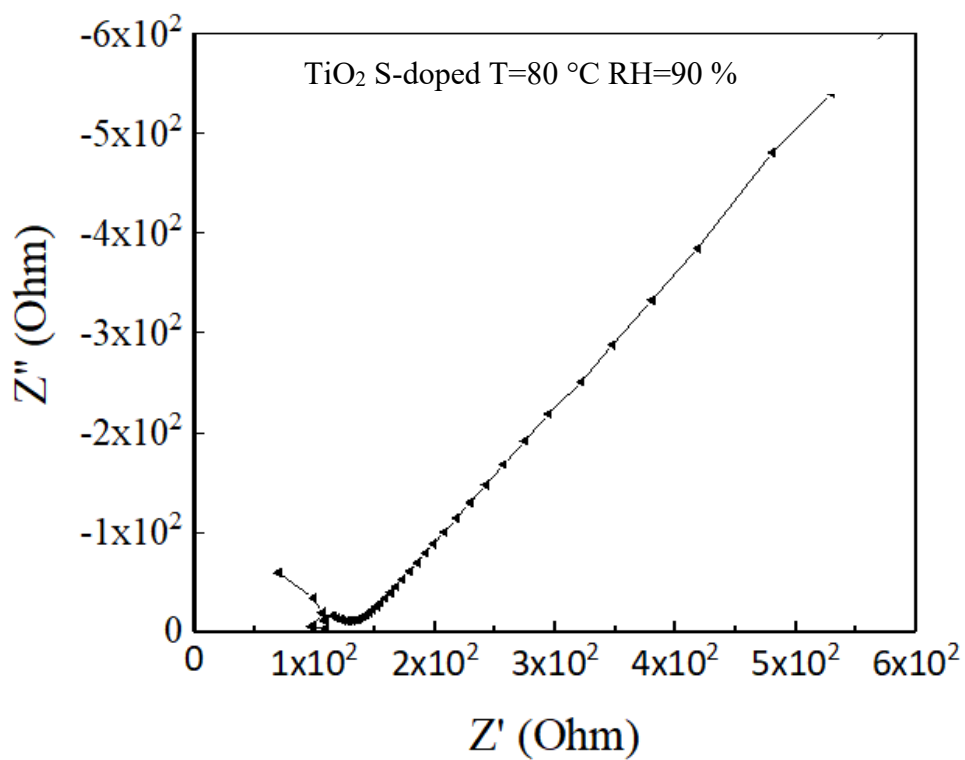
Figure 44 Impedance spectrum of TiO$_2$ S-doped at 80°C and 90 % of RH.
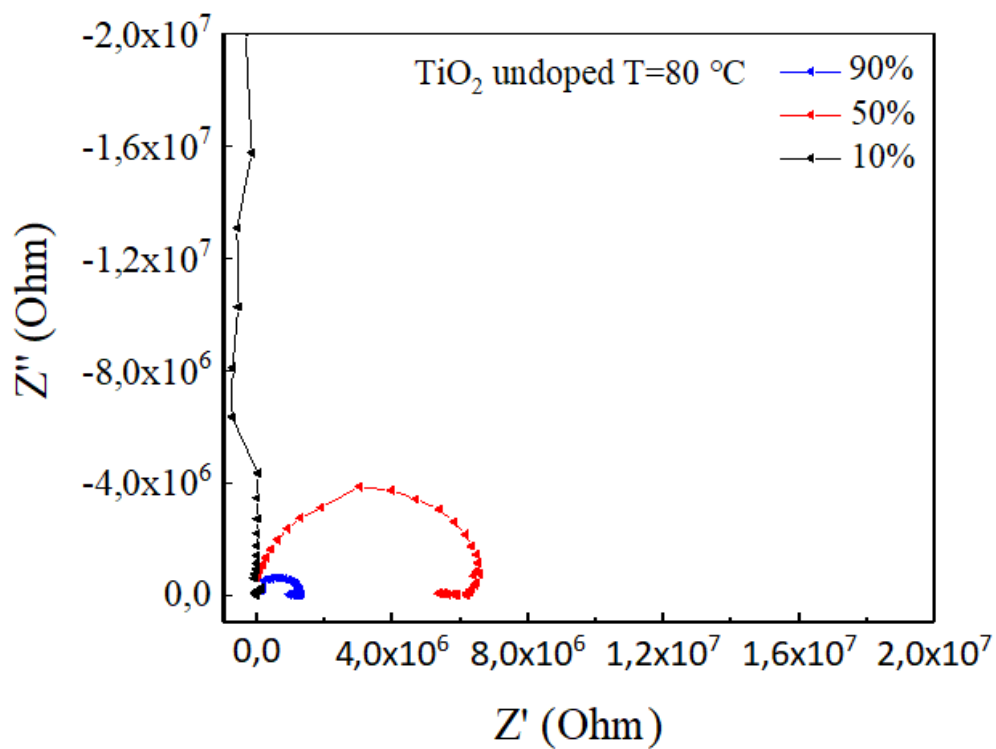
Figure 45 Impedance spectra of TiO₂ at 80 °C and different values of RH%.
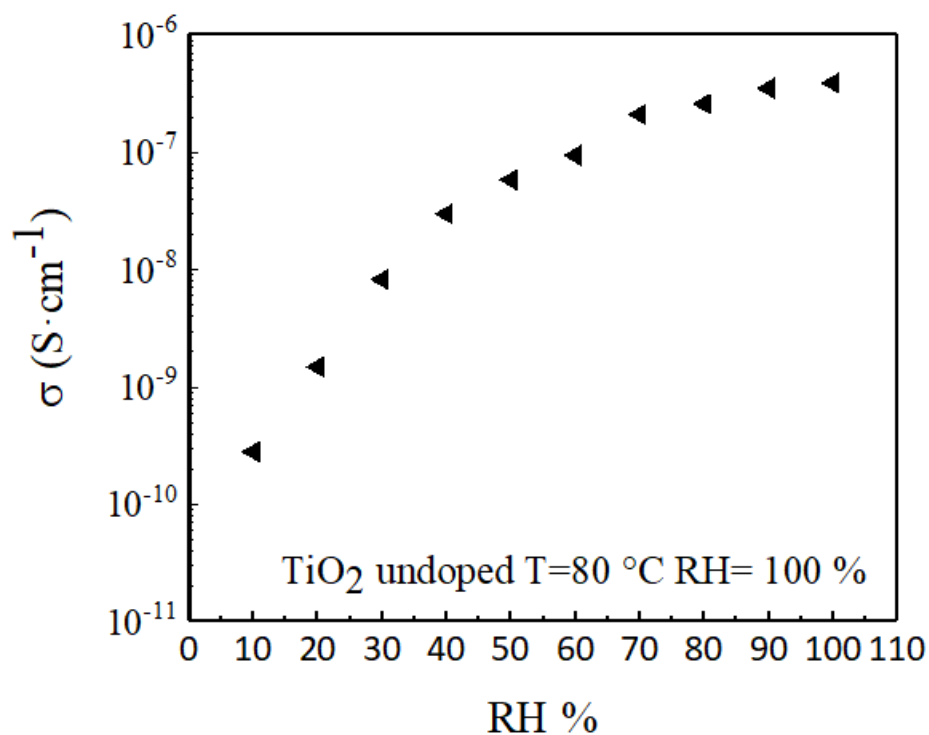
Figure 46 Conductivity in logarithmic scale vs. relative humidity of TiO₂ at 80°C.
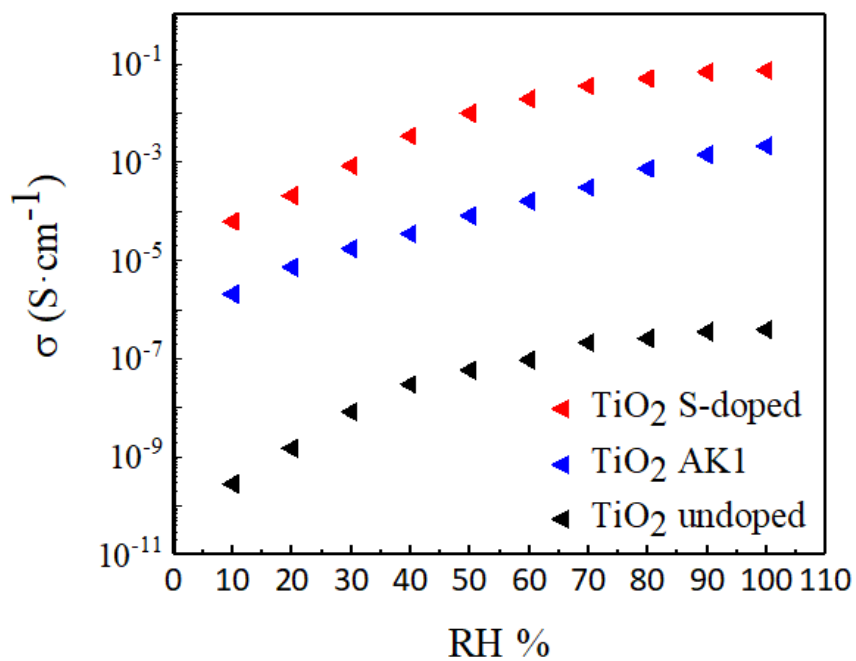
Figure 47 Conductivity in logarithmic scale vs. relative humidity of TiO_2 undoped, TiO_2 AK1 and S-TiO_2 at 80°C.
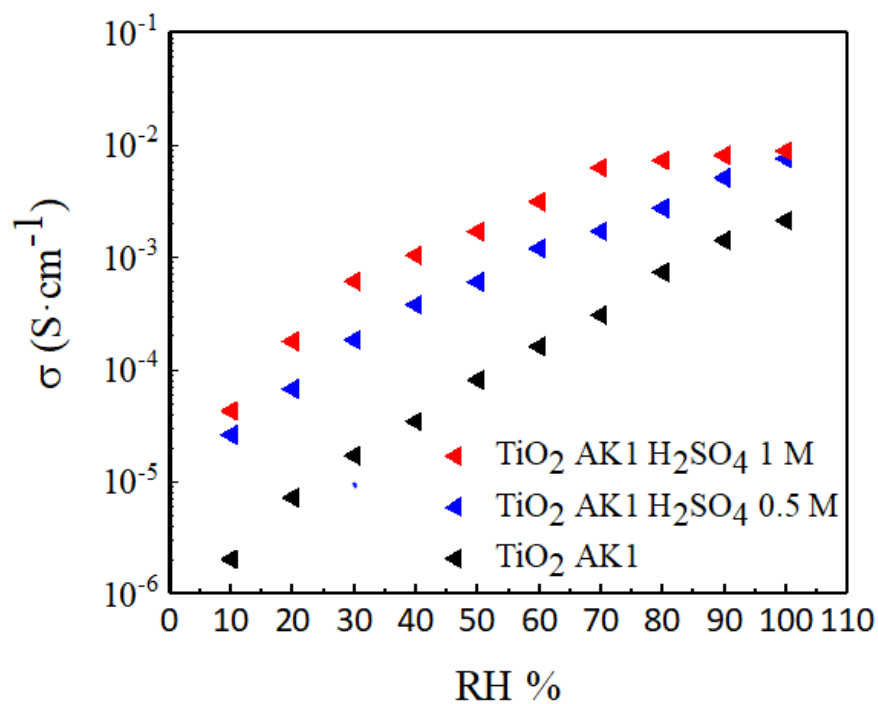
Figure 48 Conductivity in logarithmic scale vs. relative humidity of TiO_2 AK1, TiO_2 AK1 immersed in H_2SO_4 0.5 M and TiO_2 immersed in H_2SO_4 1 M at 80°C.
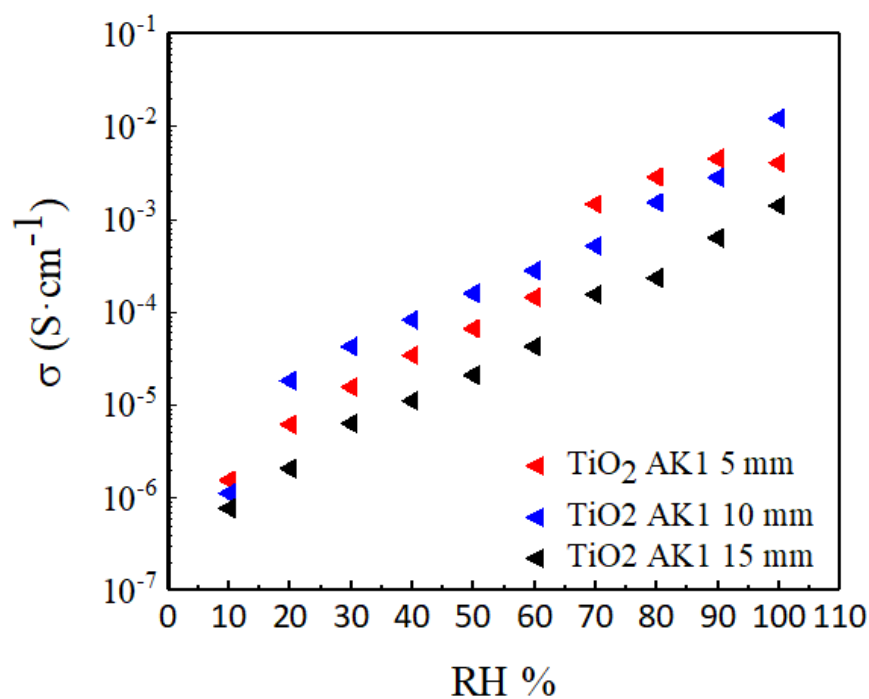
Figure 49 Conductivity in logarithmic scale vs. relative humidity of sintered samples of TiO₂ AK1 of different size at 80°C.
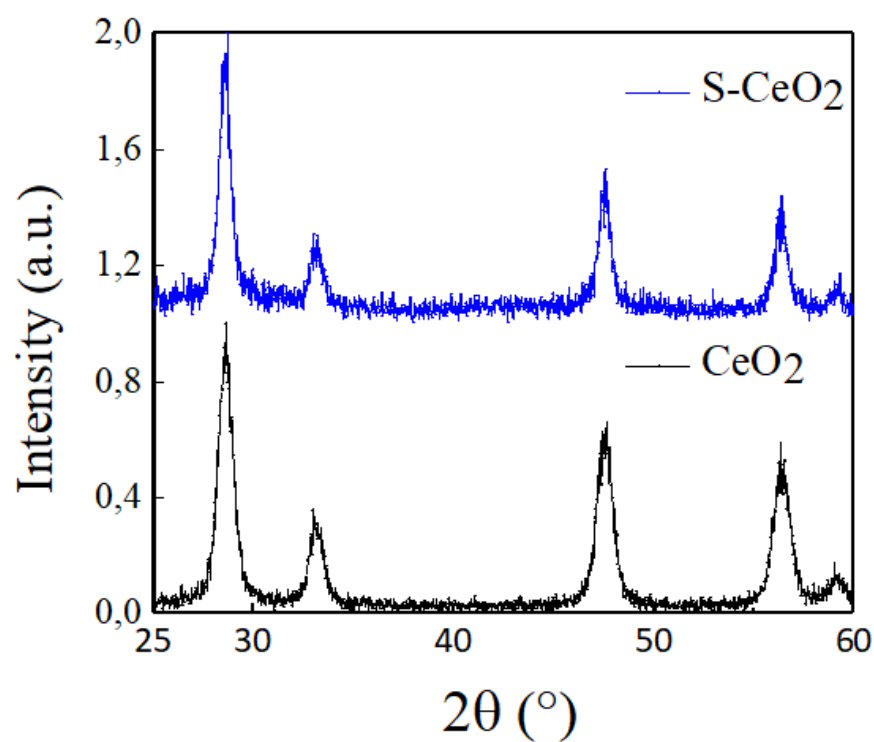
Figure 50 XRD of CeO₂ powder and S-CeO₂ powder.
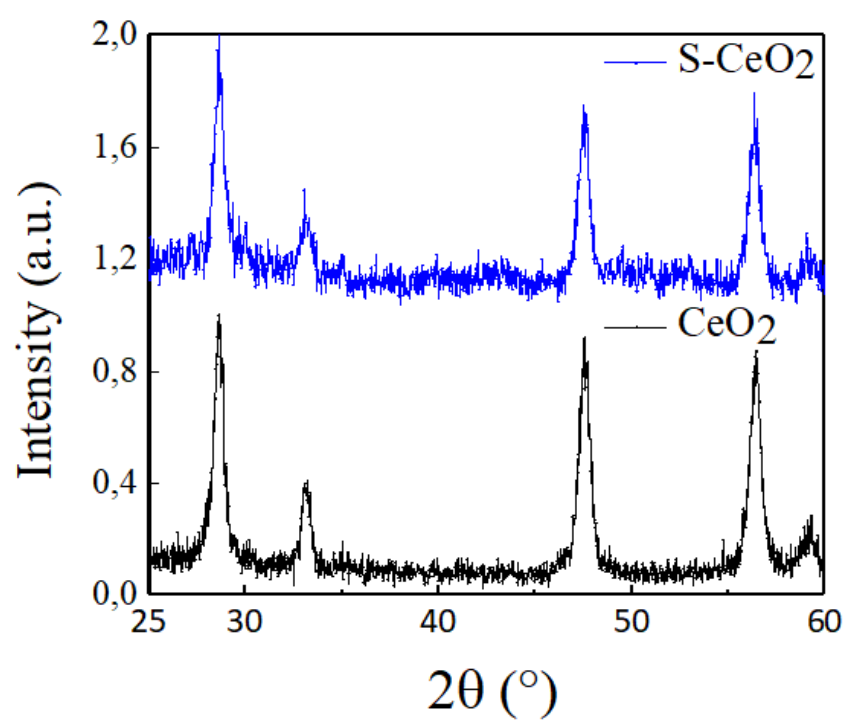
Figure 51 XRD of CeO₂ sintered sample and S-CeO₂ sintered sample.
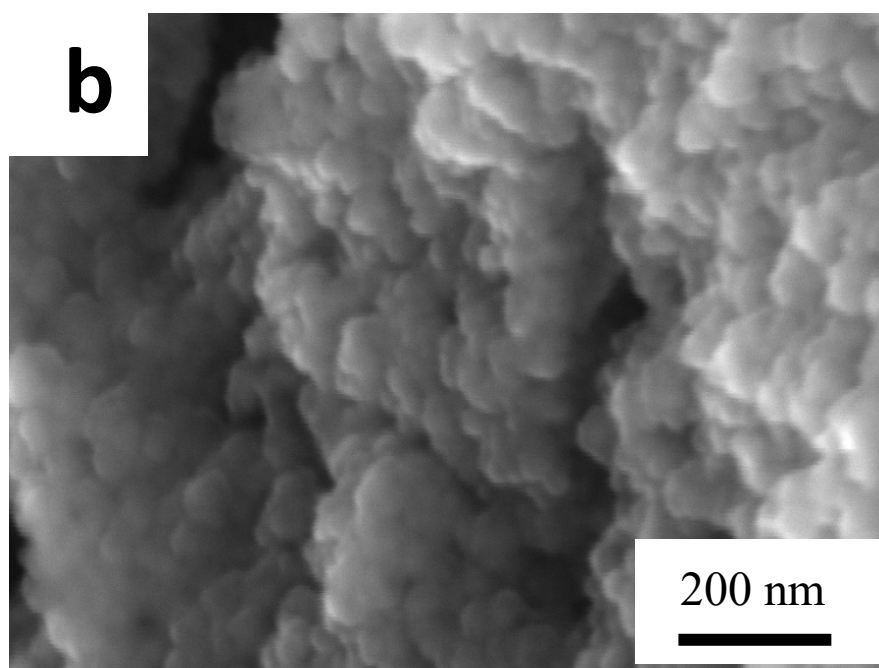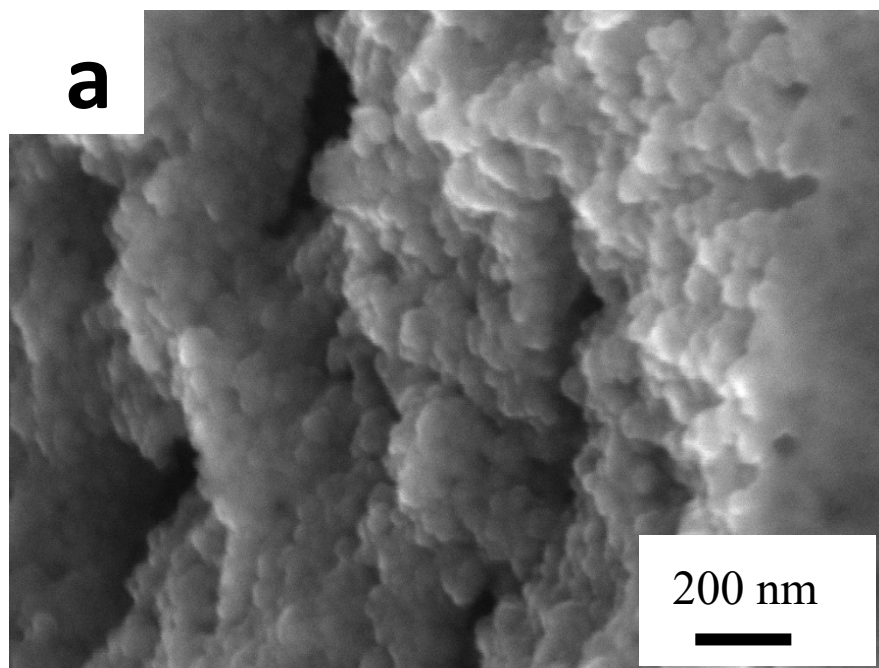
Figure 52 SEM images of the CeO$_2$ undoped powder (a) and CeO$_2$ sulfur doped powder (b).
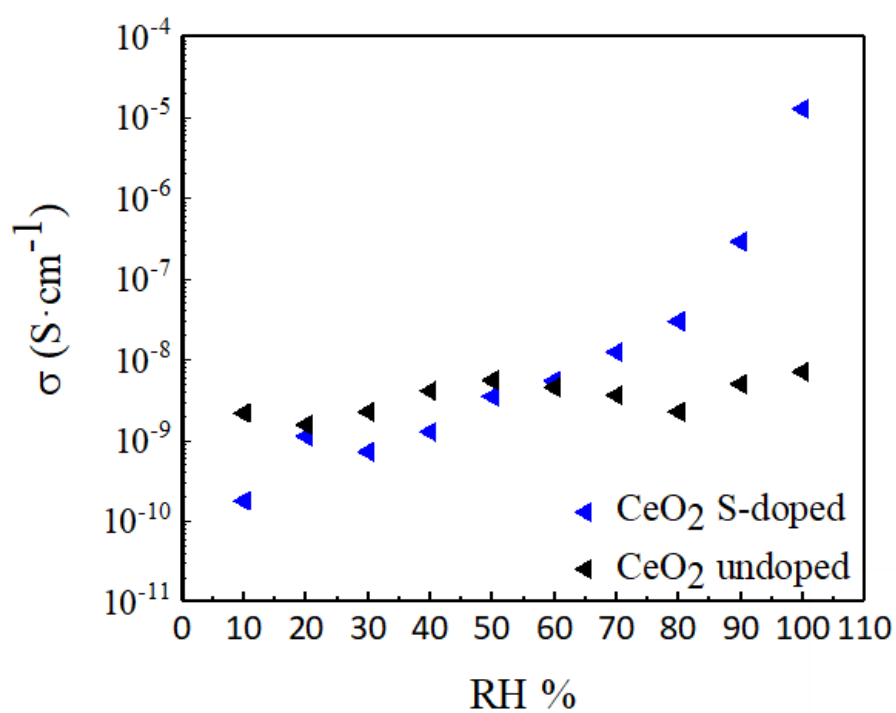
Figure 53 Conductivity in logarithmic scale vs. relative humidity of CeO_2 undoped and $S\text{-}CeO_2$ at 80°C.
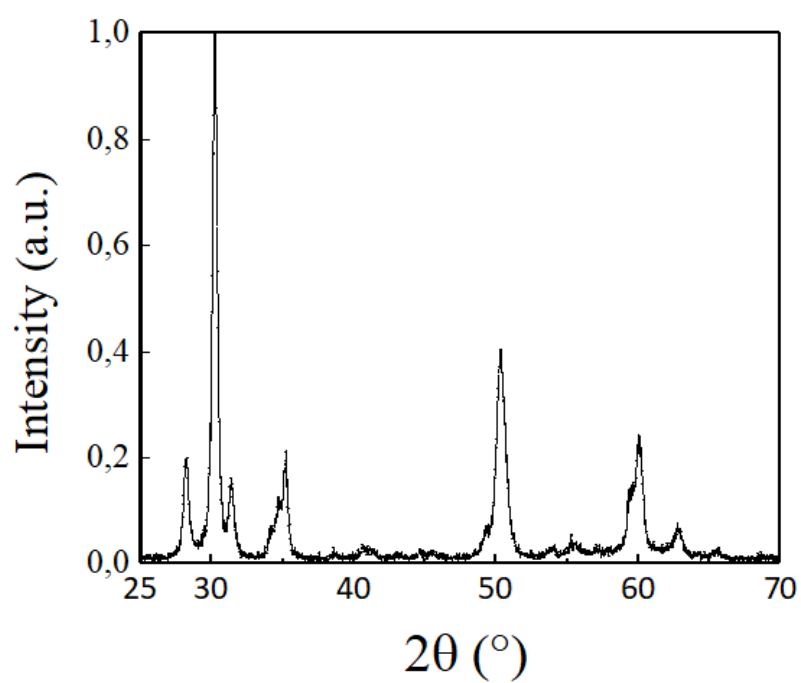
Figure 54 XRD pattern of ZrO_2 TOSOH powder.
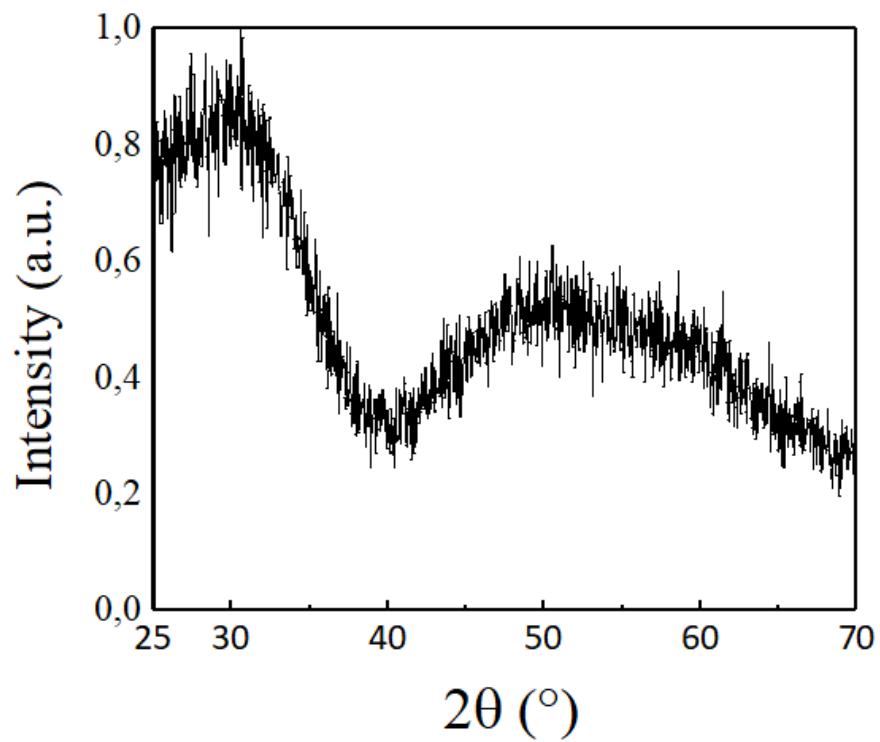
Figure 55 XRD pattern of S-ZrO₂ powder as synthesized at 600 °C for 5h.
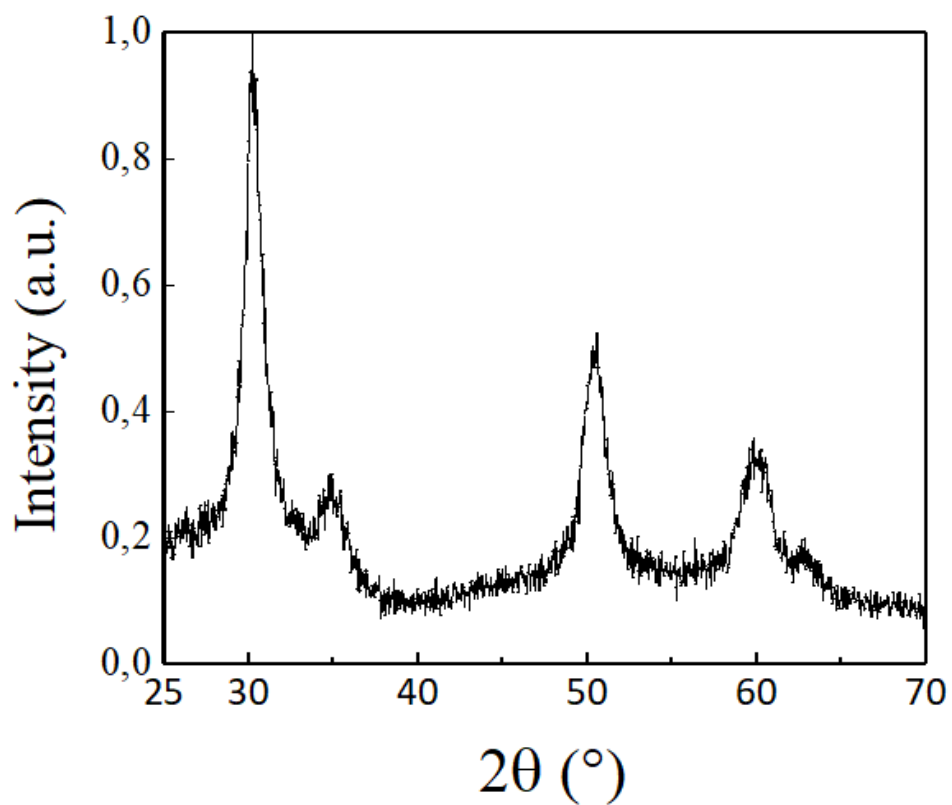
Figure 56 XRD pattern of S-ZrO₂ annealed at 600 °C for 18h.
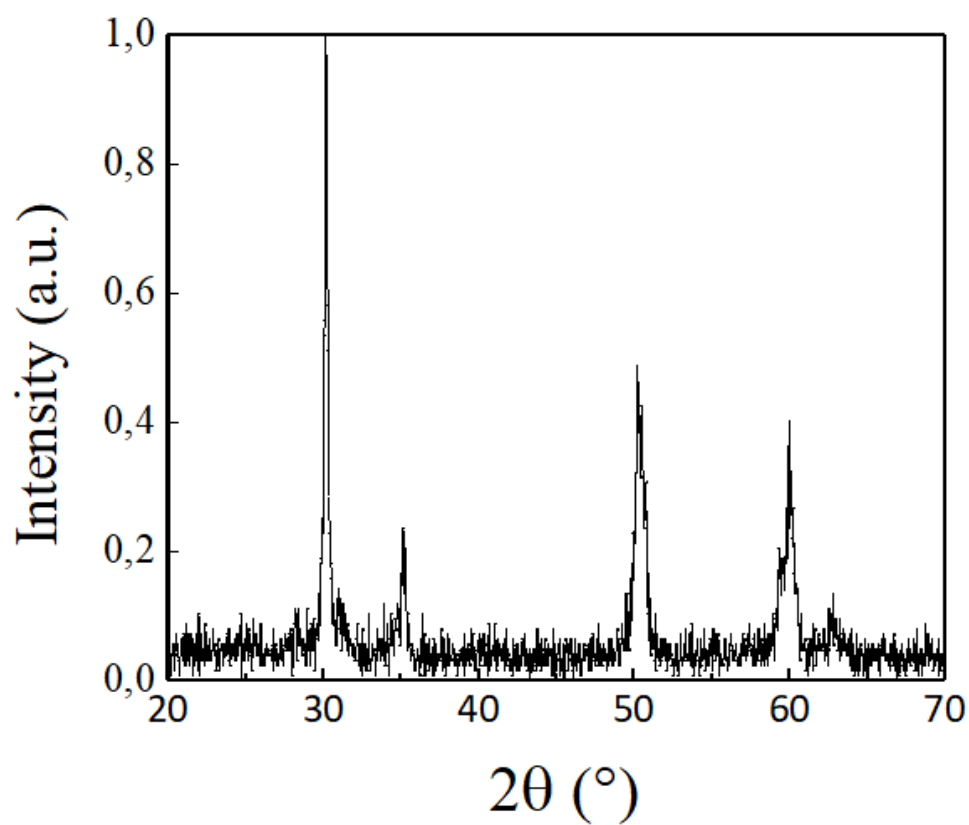
Figure 57 XRD pattern of ZrO$_2$ TOSOH sintered sample.
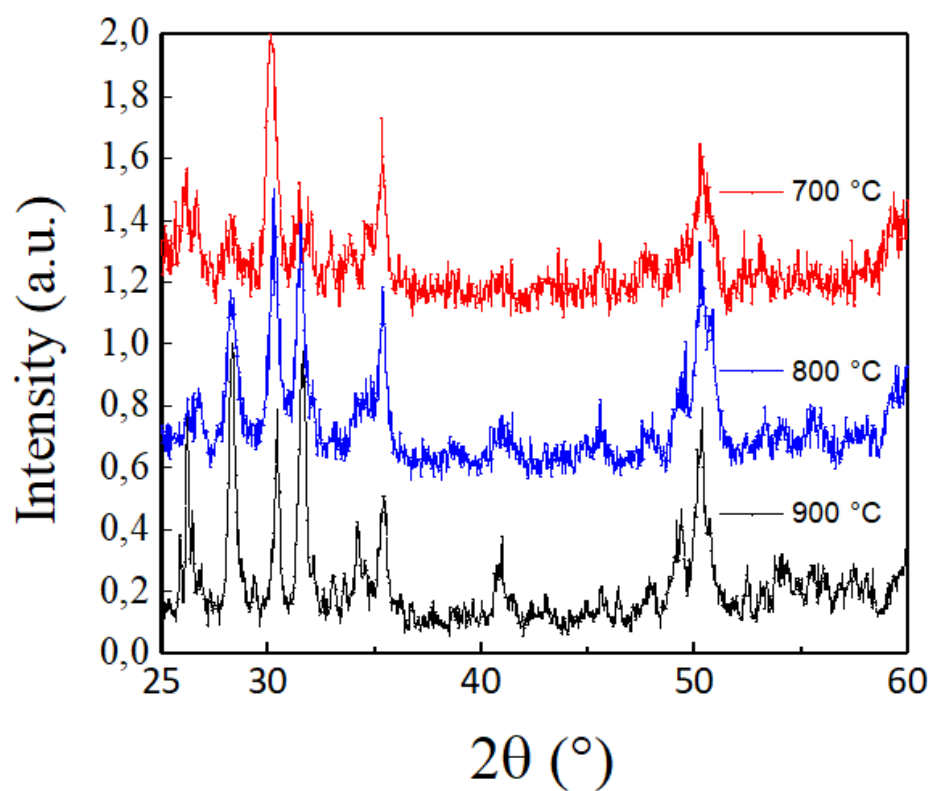
Figure 58 XRD patterns of the S-ZrO$_2$ sintered samples at different sintering temperatures.
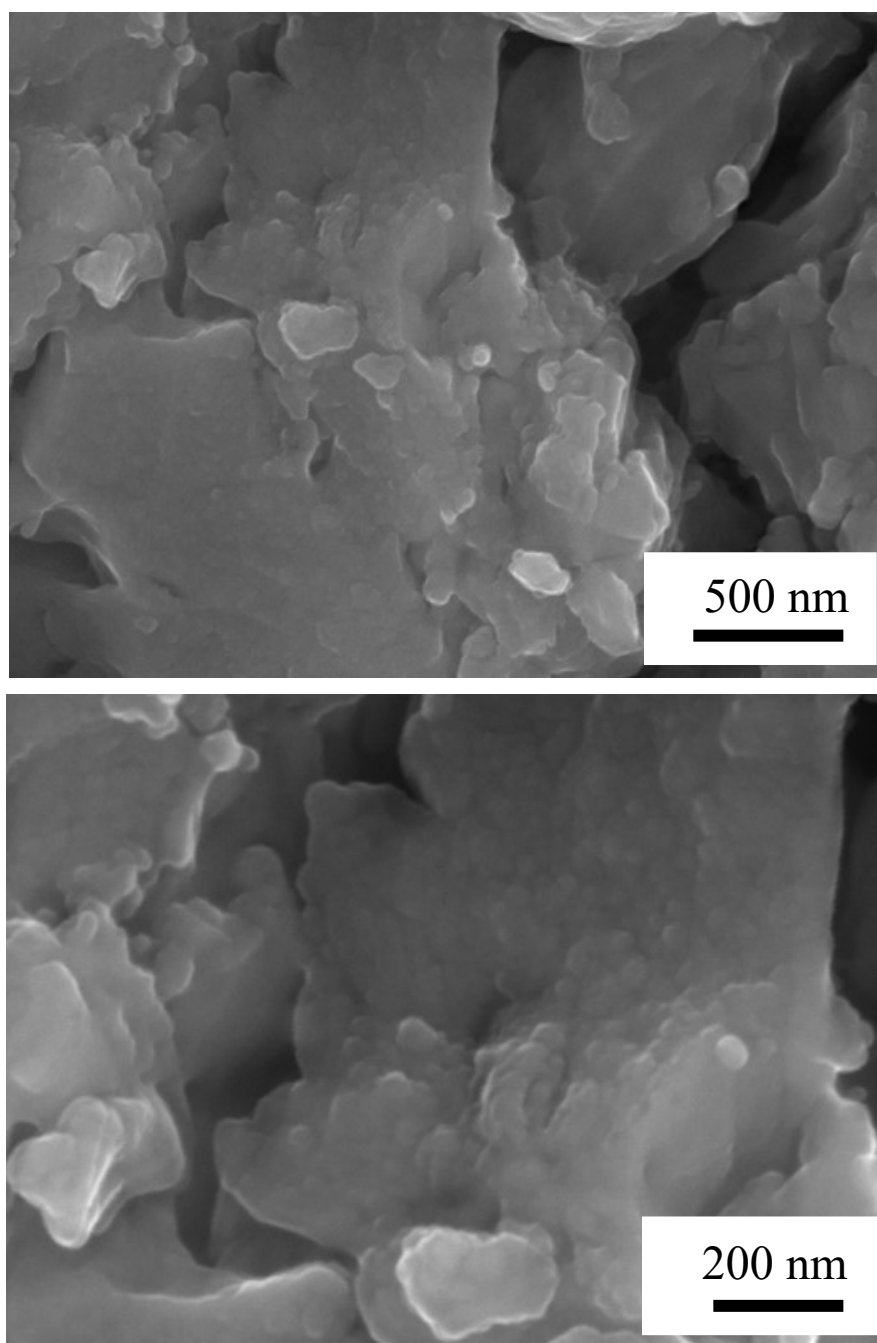
Figure 59 SEM images of S-ZrO$_2$ powder.
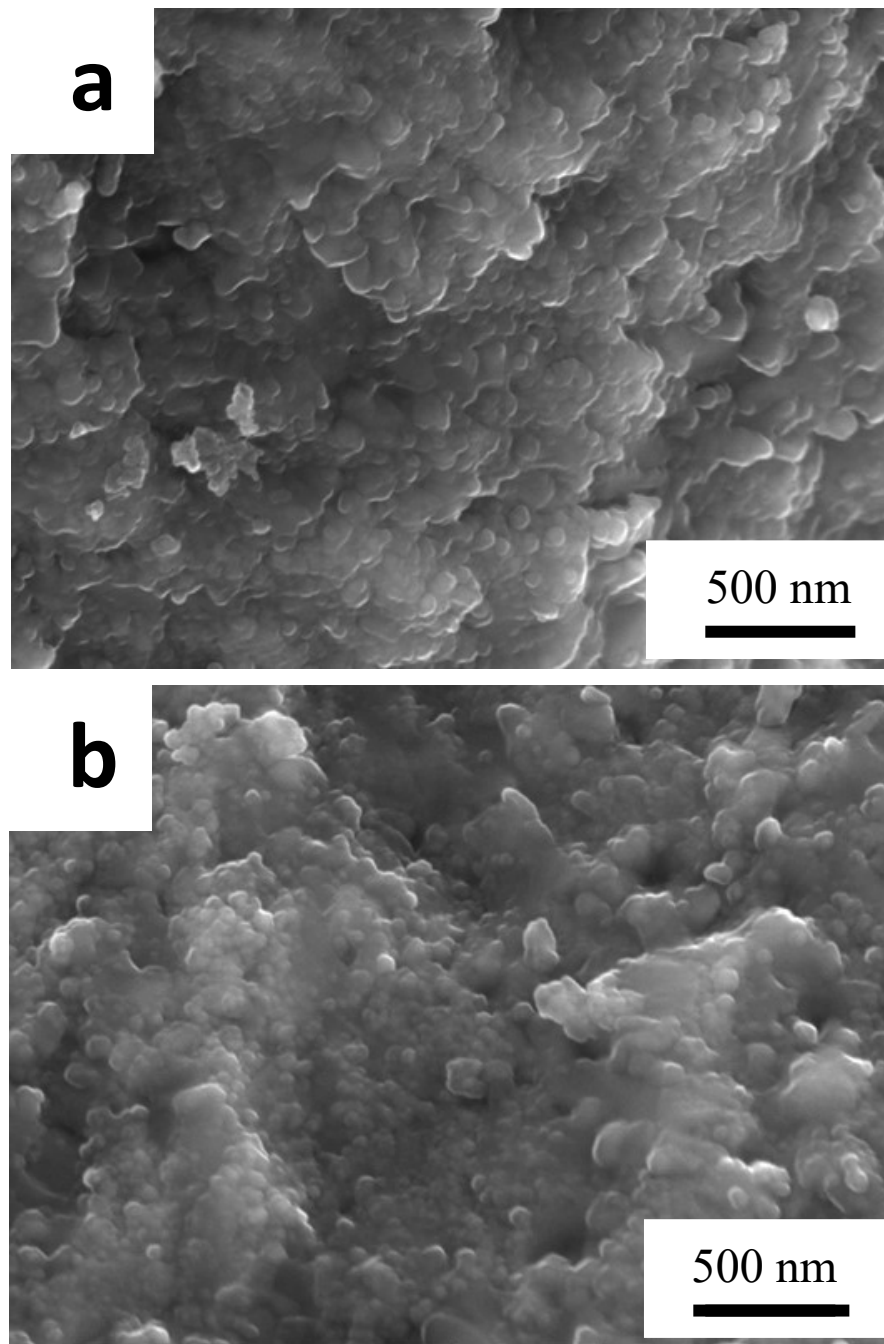
Figure 60 SEM images of S-ZrO$_2$ sintered at 700 °C (a) and sintered at 800 °C (b).
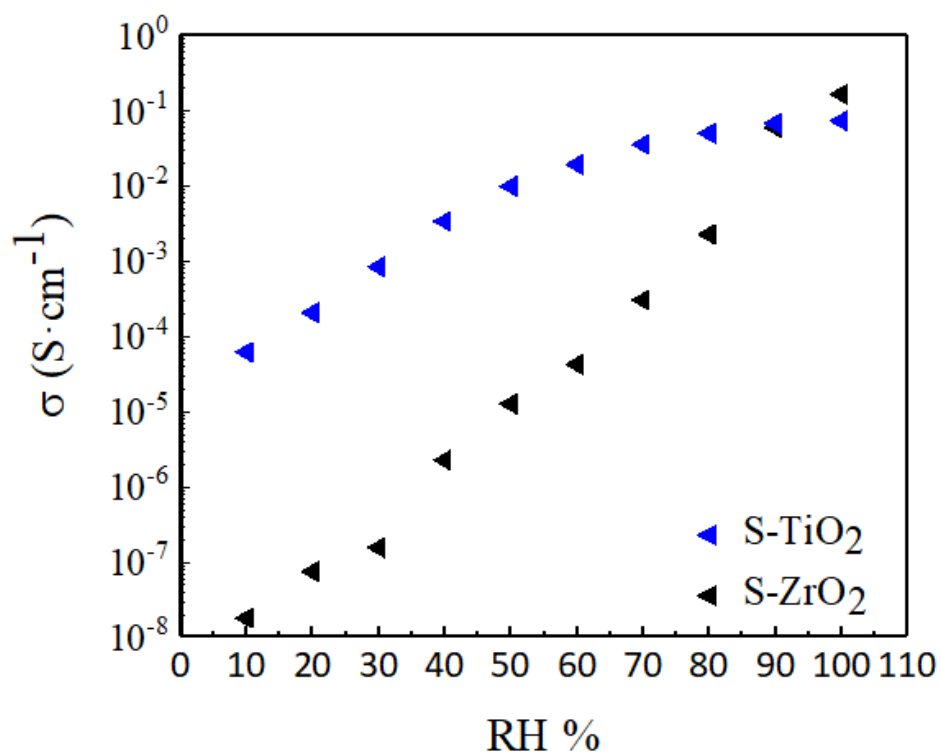
Figure 61 Conductivity in logarithmic scale vs. relative humidity of ZrO_2 undoped and S-ZrO_2 at 80°C.
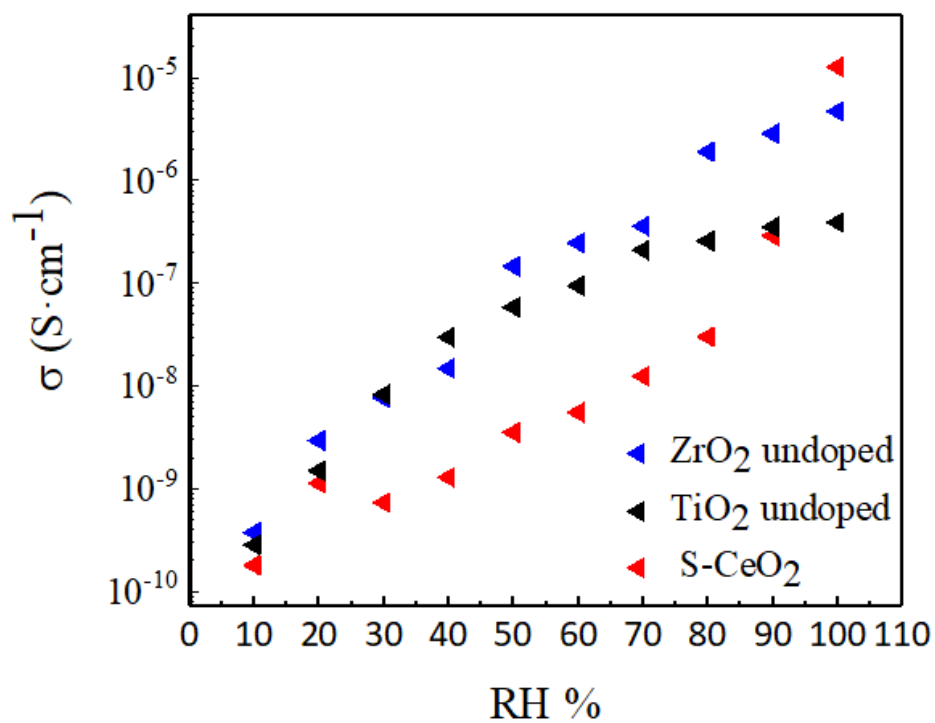
Figure 62 Conductivity in logarithmic scale vs. relative humidity of S-CeO_2, ZrO_2 and TiO_2 at 80°C.
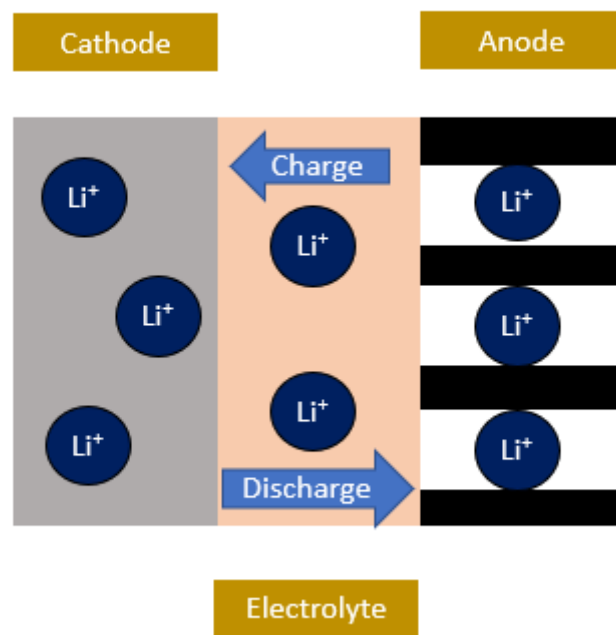
Figure 63 Schematic representation of a Lithium-ion battery.
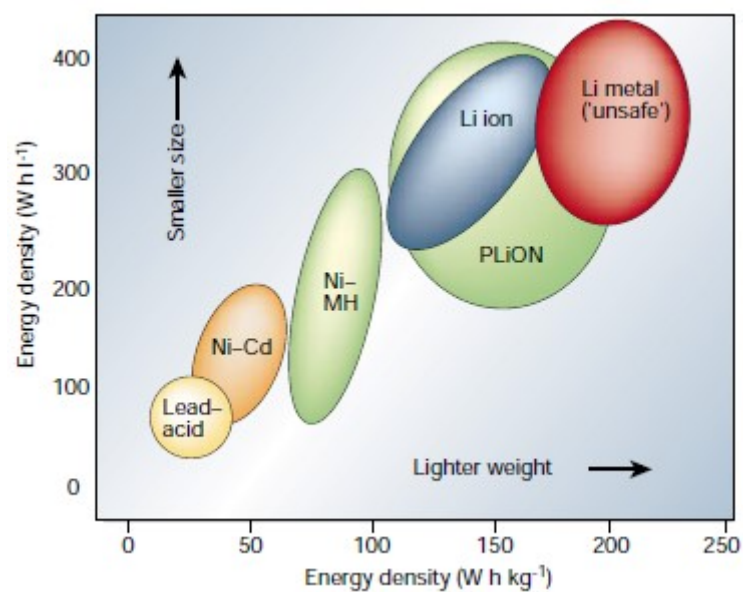
Figure 64 Energy density for unit of mass and volume for different types of rechargeable batteries [109].
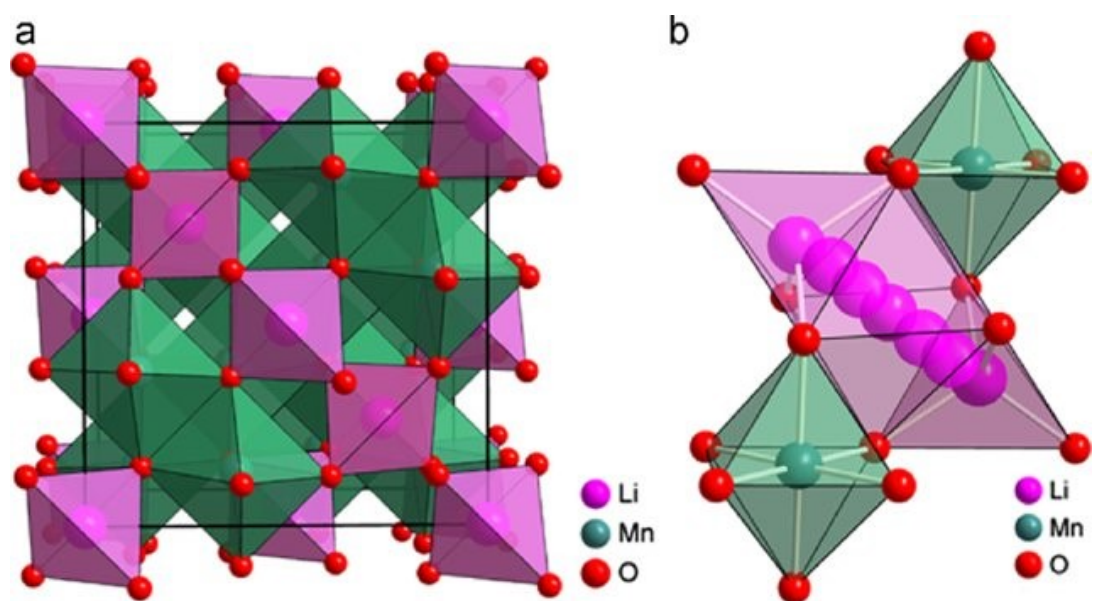
Figure 65 Crystal structure of LiMn$_2$O$_4$ [142].
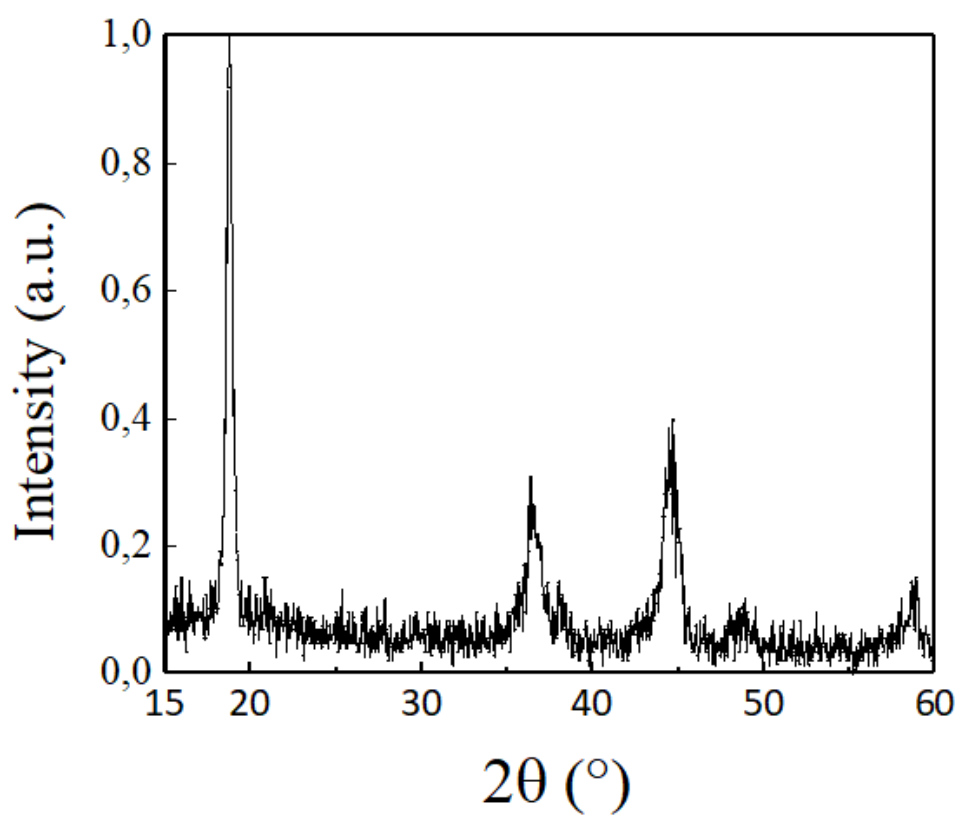
Figure 66 XRD pattern of LiMn$_2$O$_4$ powder.
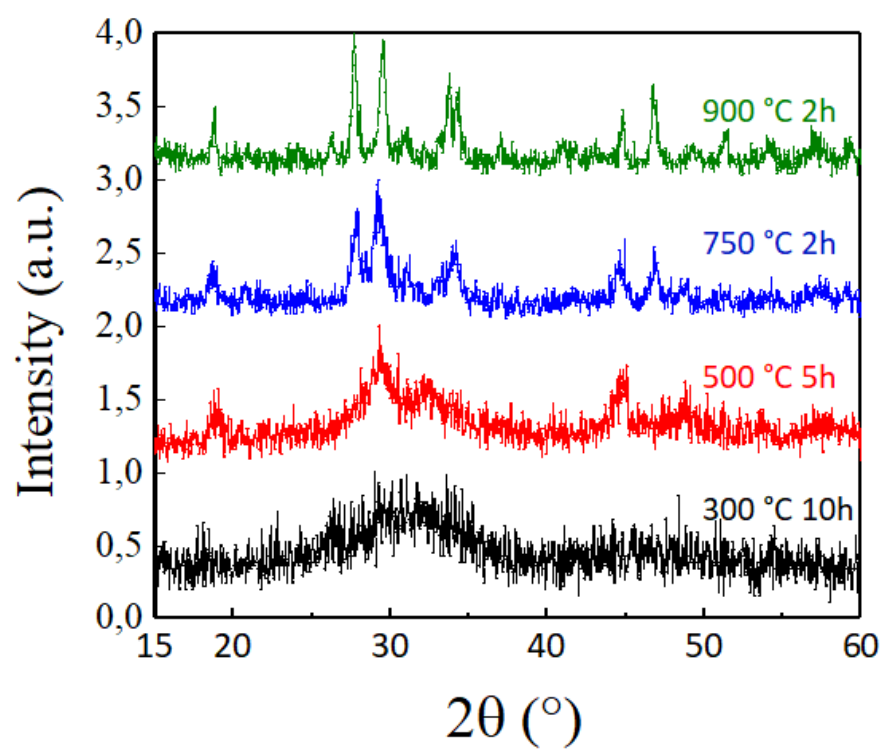
Figure 67 XRD patterns of LiYMnO$_4$ synthesized at different temperature of calcination.
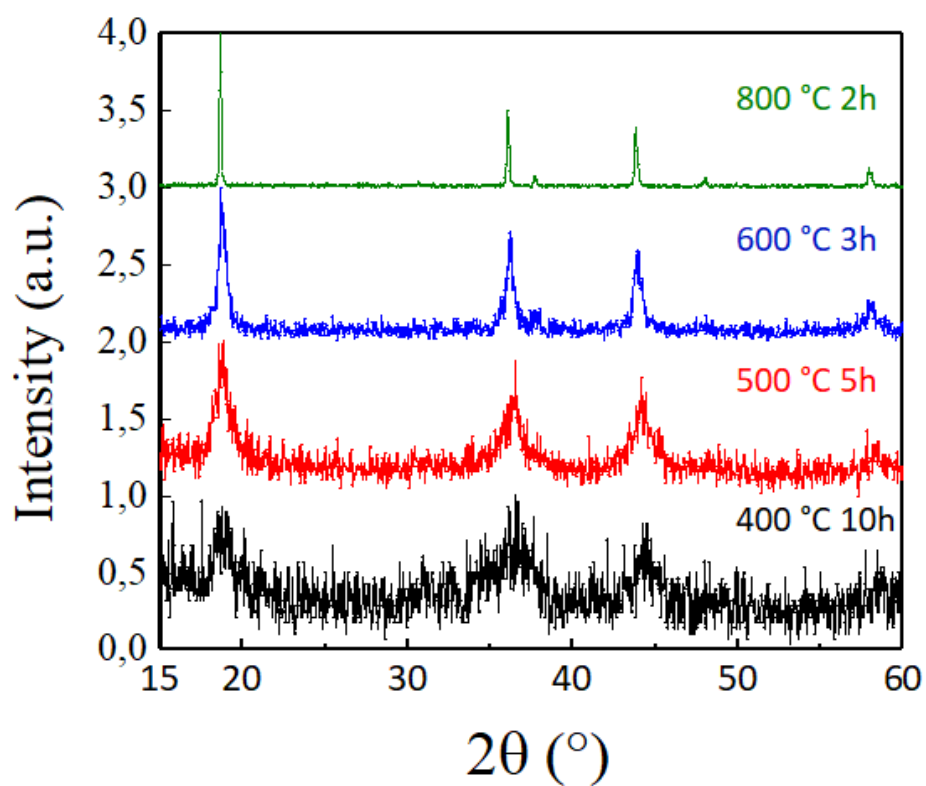
Figure 68 XRD patterns of LiFe$_{0.5}$Ti$_{0.5}$MnO$_4$ synthesized at different temperature of calcination.
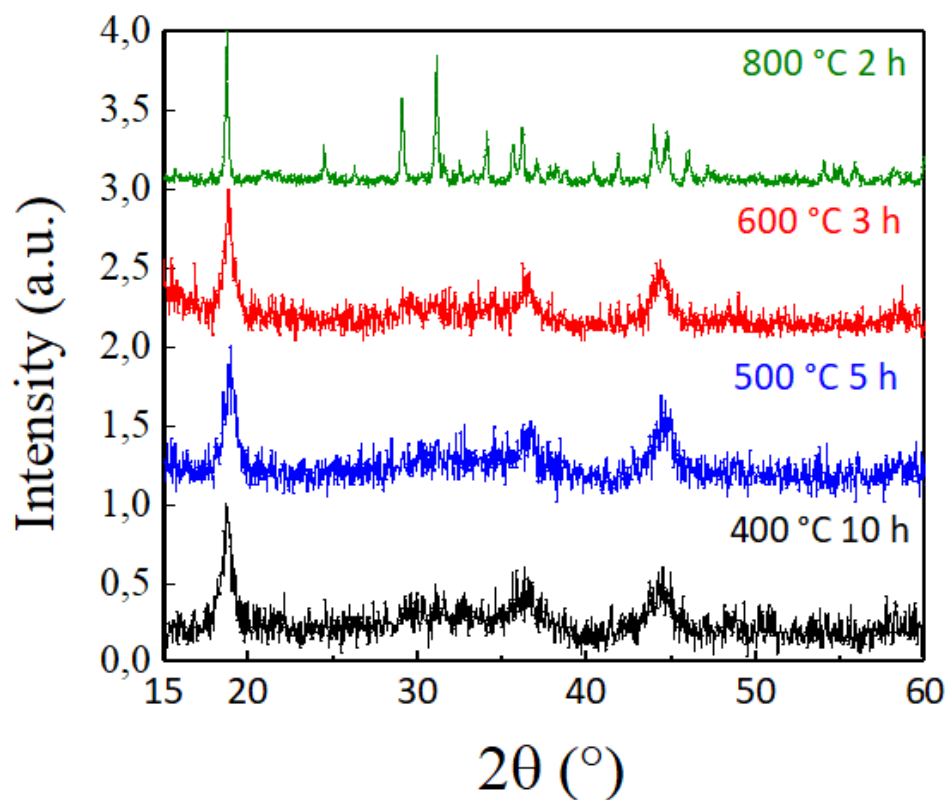
Figure 69 XRD patterns of LiY$_{0.33}$Fe$_{0.33}$Mn$_{1.34}$O$_4$ powders calcinated at different temperatures.
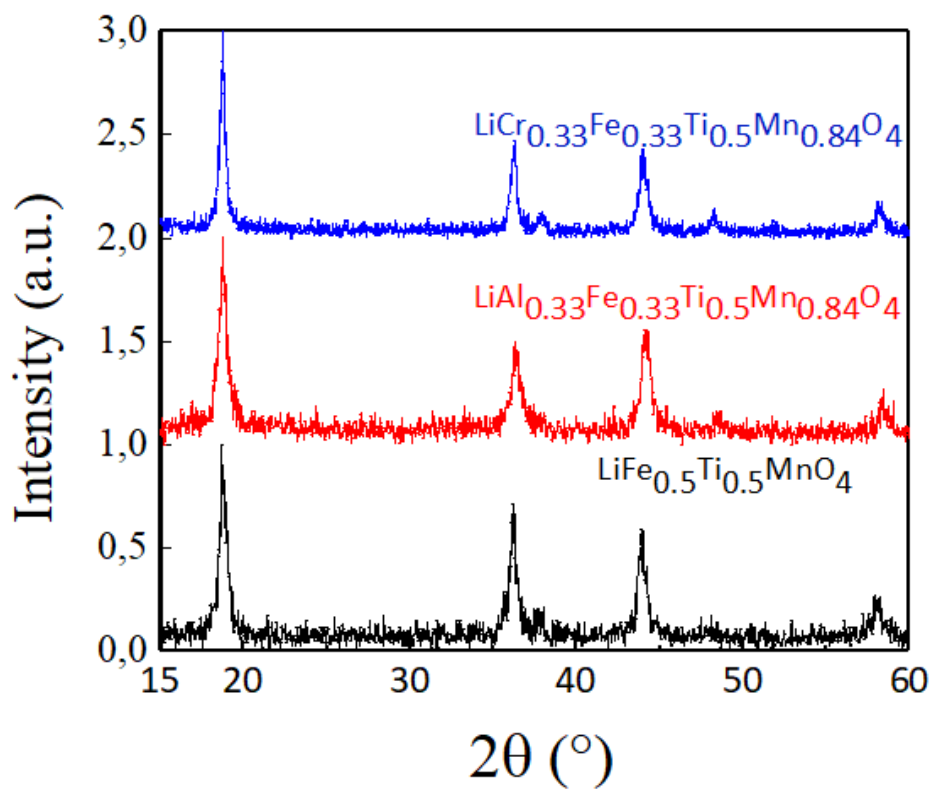
Figure 70 XRD patterns of LiFe$_{0.5}$Ti$_{0.5}$MnO$_4$, LiAl$_{0.33}$Fe$_{0.33}$Ti$_{0.5}$Mn$_{0.84}$O$_4$ and LiCr$_{0.33}$Fe$_{0.33}$Ti$_{0.5}$Mn$_{0.84}$O$_4$ powders calcinated at 600 °C for 3h.
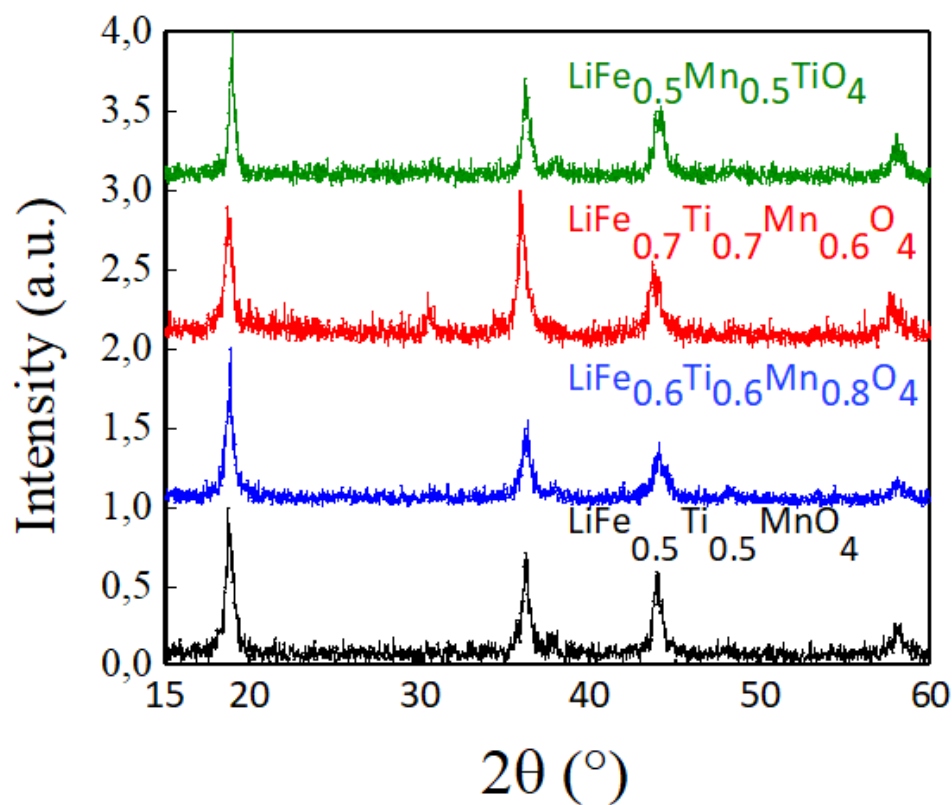
Figure 71 XRD patterns of LiFe$_{0.5}$Ti$_{0.5}$MnO$_4$, of LiFe$_{0.6}$Ti$_{0.6}$Mn$_{0.8}$O$_4$, of LiFe$_{0.7}$Ti$_{0.7}$Mn$_{0.6}$O$_4$ powders calcinated at 600 °C for 3h.

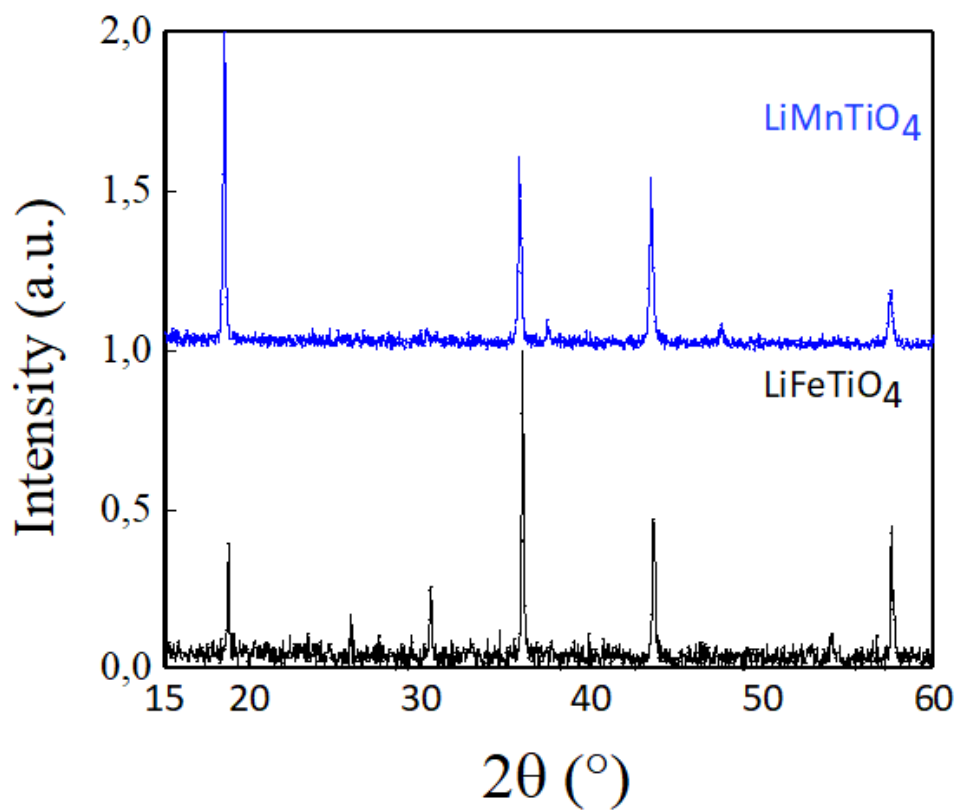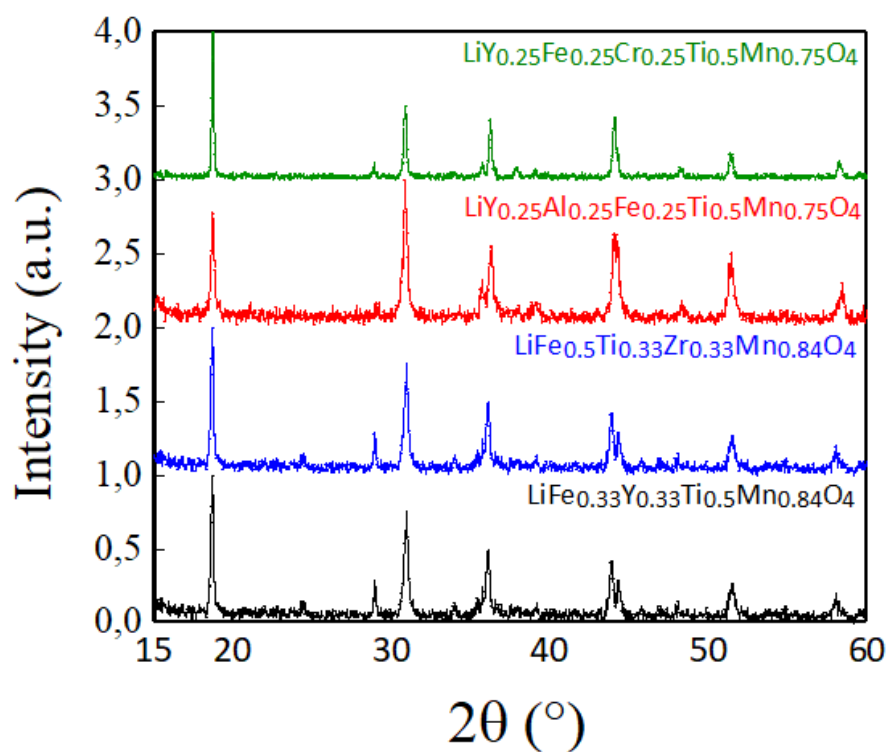*Figure 72 XRD patterns of LiMnTiO$_4$ and LiFeTiO$_4$ calcined at 800 °C for 2h.*

Figure 73 XRD patterns of LiFe$_{0.33}$Y$_{0.33}$Ti$_{0.5}$Mn$_{0.84}$O$_4$, LiFe$_{0.5}$Ti$_{0.33}$Zr$_{0.33}$Mn$_{0.84}$O$_4$, LiY$_{0.25}$Fe$_{0.25}$Cr$_{0.25}$Ti$_{0.5}$Mn$_{0.75}$O$_4$ and LiY$_{0.25}$Al$_{0.25}$Fe$_{0.25}$Ti$_{0.5}$Mn$_{0.75}$O$_4$ calcinated at 800 °C for 2h.
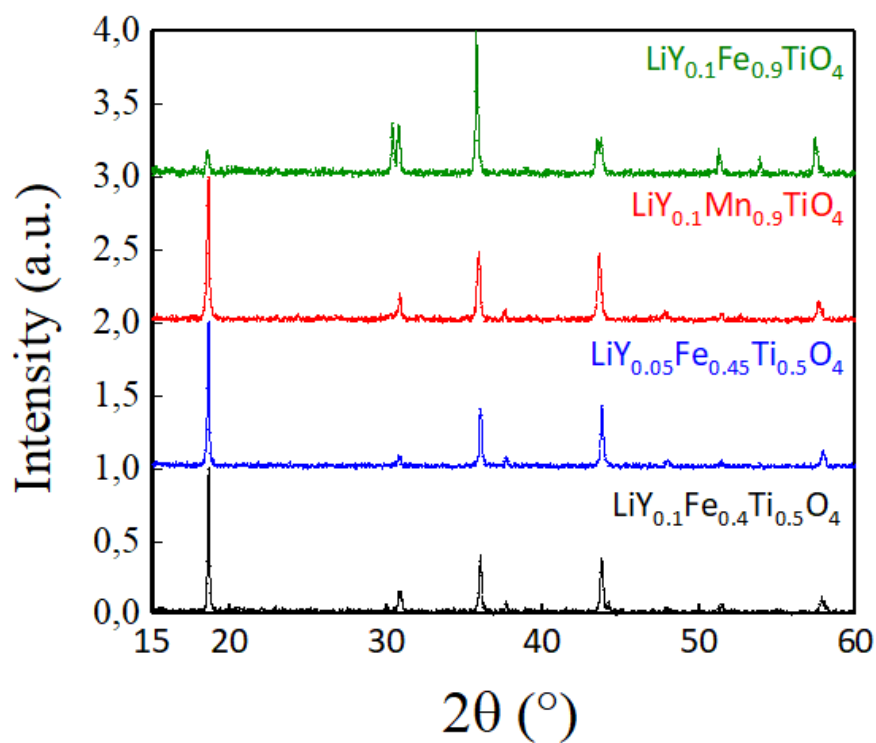
Figure 74 XRD patterns of LiY$_{0.1}$Fe$_{0.4}$Ti$_{0.5}$O$_4$, LiY$_{0.05}$Fe$_{0.45}$Ti$_{0.5}$O$_4$, LiY$_{0.1}$Mn$_{0.9}$TiO$_4$ and LiY$_{0.1}$Fe$_{0.9}$TiO$_4$ calcinated at 800 °C for 2h.
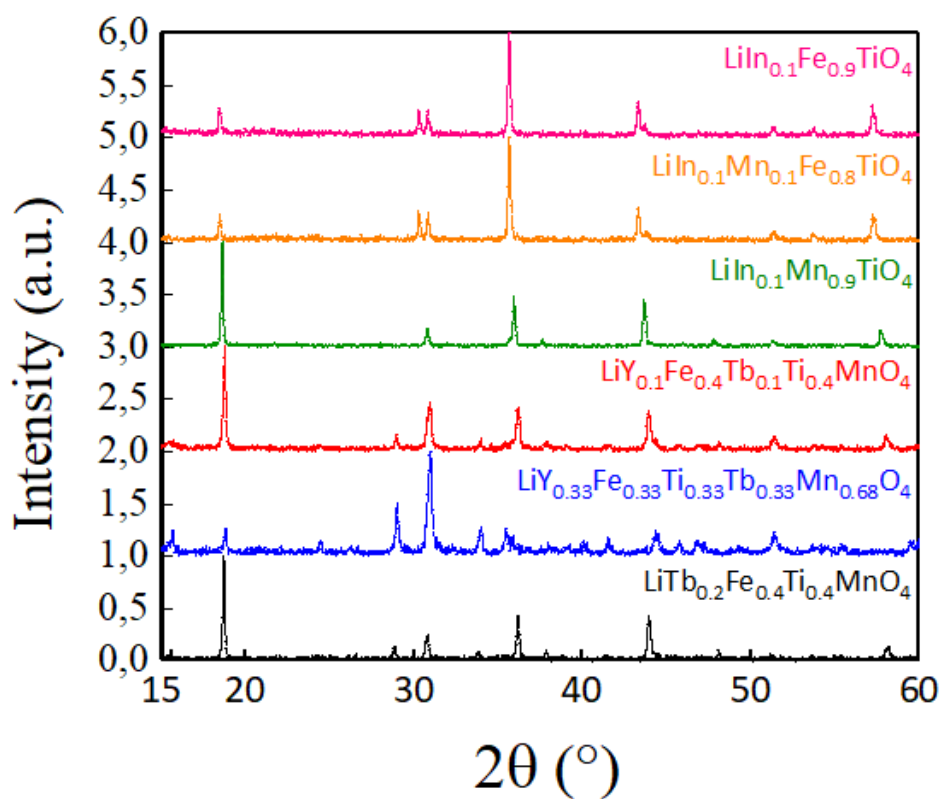
Figure 75 XRD patterns of LiTb$_{0.2}$Fe$_{0.4}$Ti$_{0.4}$MnO$_4$, LiY$_{0.33}$Fe$_{0.33}$Ti$_{0.33}$Tb$_{0.33}$Mn$_{0.68}$O$_4$, LiY$_{0.1}$Fe$_{0.4}$Tb$_{0.1}$Ti$_{0.4}$MnO$_4$, LiIn$_{0.1}$Mn$_{0.9}$TiO$_4$, LiIn$_{0.1}$Mn$_{0.1}$Fe$_{0.8}$TiO$_4$ and LiIn$_{0.1}$Fe$_{0.9}$TiO$_4$ calcinated at 800 °C for 2h.
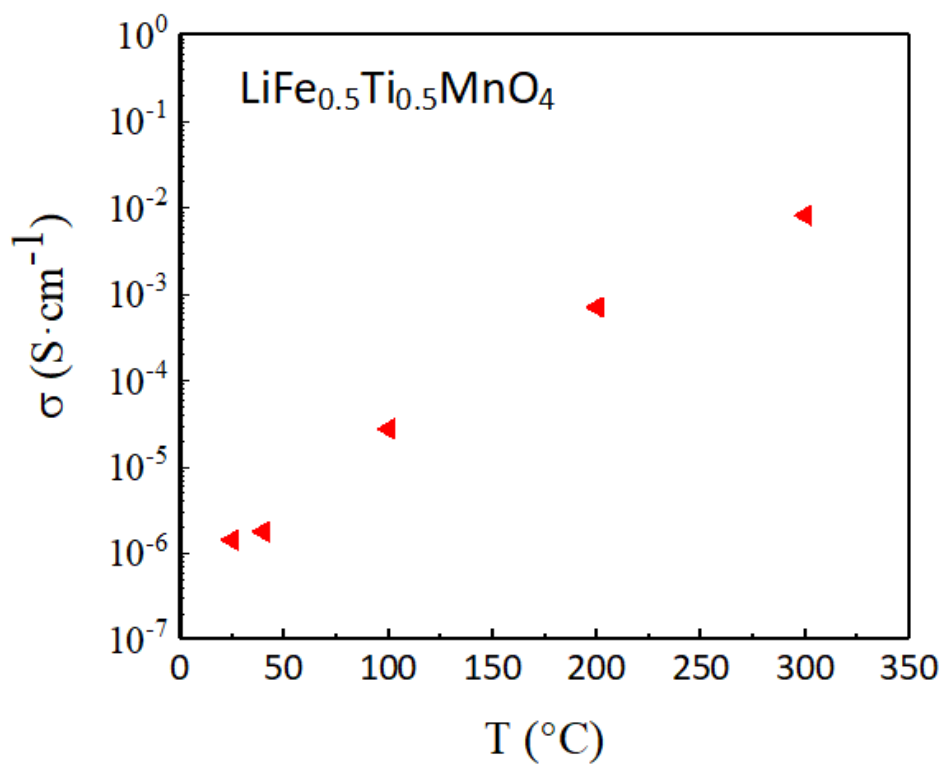
Figure 76 Electrical conductivity in logarithmic scale of LiFe$_{0.5}$Ti$_{0.5}$MnO$_4$ sintered sample with the variation of temperature.
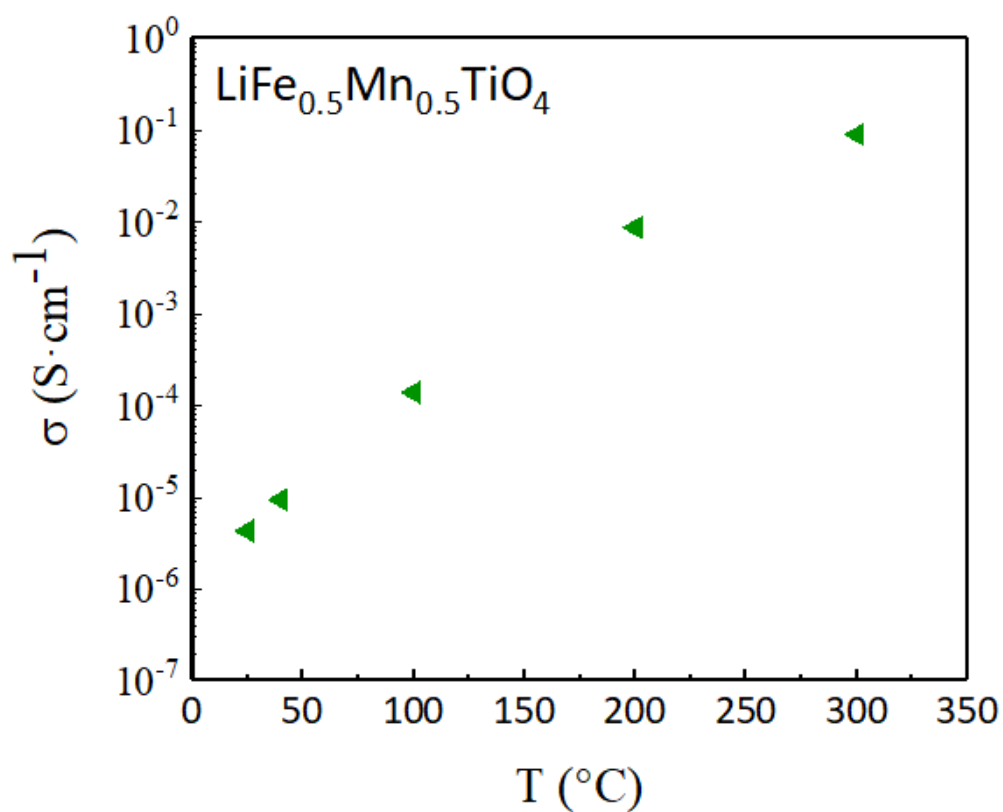
Figure 77 Electrical conductivity in logarithmic scale of LiFe$_{0.5}$Mn$_{0.5}$TiO$_4$ sintered sample with the variation of temperature.
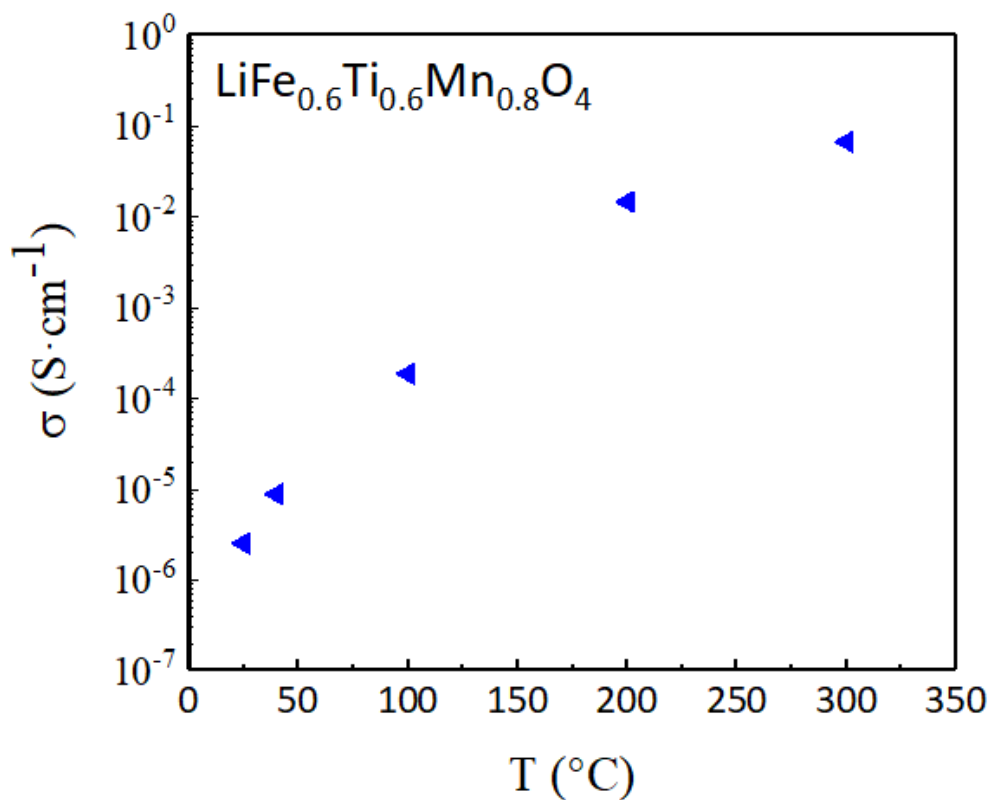
Figure 78 Electrical conductivity in logarithmic scale of LiFe$_{0.6}$Ti$_{0.6}$Mn$_{0.8}$O$_4$ sintered sample with the variation of temperature.
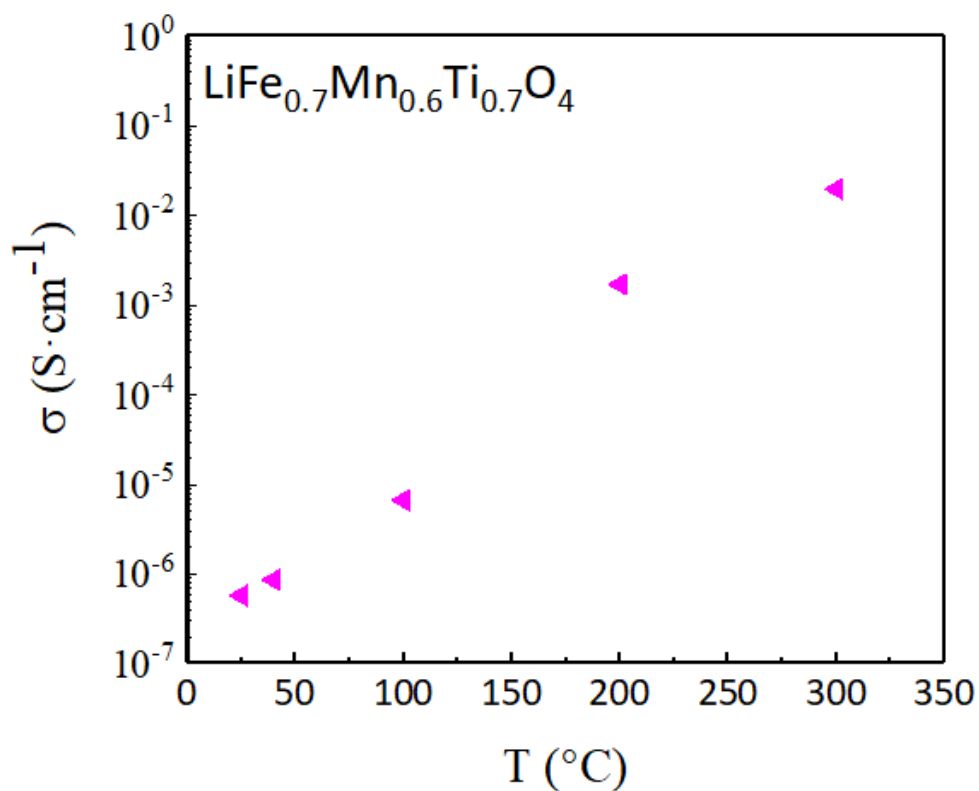
Figure 79 Electrical conductivity in logarithmic scale of LiFe$_{0.7}$ Mn$_{0.6}$Ti$_{0.7}$O$_4$ sintered sample with the variation of temperature.

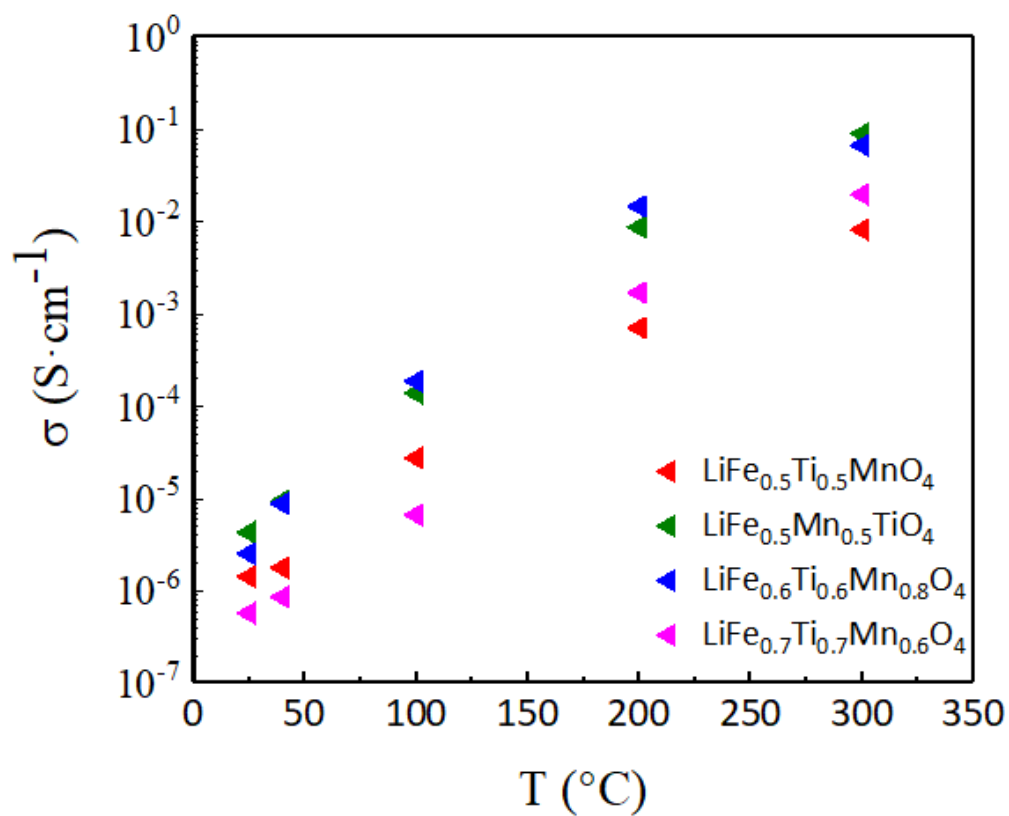*Figure 80 Electrical conductivity in logarithmic scale of LiFe$_{0.5}$Ti$_{0.5}$MnO$_4$, LiFe$_{0.5}$Mn$_{0.5}$TiO$_4$, LiFe$_{0.6}$Ti$_{0.6}$Mn$_{0.8}$O$_4$ and LiFe$_{0.7}$ Mn$_{0.6}$Ti$_{0.7}$O$_4$ sintered sample with the variation of temperature.*

8. Bibliography

1. Philippe Boch & Jean-Claude Nièpce. Ceramic Materials: Processes, Properties, and Applications. (Wiley, 2010).

2. Zboril, R., Mashlan, M. & Petridis, D. Iron(III) Oxides from Thermal Processes Synthesis, Structural and Magnetic Properties, Mössbauer Spectroscopy Characterization, and Applications †. Chem. Mater. 14, 969–982 (2002).

3. Long, R. A., inventor; Posta, J. J., assignee. IMPLANTABLE CERAMIC BONE PROSTHESIS. United States Patent US 3905047A. (1975).

4. Davidson, J. A., inventor, Smith and Nephew Richards Inc, assignee. ZIRCONIUM OXIDE COATED PROSTHESIS FOR WEAR AND CORROSION RESISTANCE. United States Patent US 5037438A. (1989).

5. Duncan W. Bruce, Dermot O'Hare & Richard I. Walton. Functional Oxides. (Wiley, 2010).

6. Fernández-García, M., Martínez-Arias, A., Hanson, J. C. & Rodriguez, J. A. Nanostructured Oxides in Chemistry: Characterization and Properties. Chem. Rev. 104, 4063–4104 (2004).

7. Gleiter, H. Nanostructured materials: basic concepts and microstructure. Acta Mater. 48, 1–29 (2000).

8. Gleiter, H. Nanostructured materials: state of the art and perspectives. Nanostructured Mater. 6, 3-14 (1995).

9. Stephen Blundell. Magnetism in Condensed Matter. (OUP Oxford, 2001).

10. Issa, B., Obaidat, I., Albiss, B. & Haik, Y. Magnetic Nanoparticles: Surface Effects and Properties Related to Biomedicine Applications. Int. J. Mol. Sci. 14, 21266–21305 (2013).

11. Leslie-Pelecky, D. L. & Rieke, R. D. Magnetic Properties of Nanostructured Materials. Chem. Mater. 8, 1770–1783 (1996).

12. Ilya Prigogine & Stuart A. Rice. Advances in Chemical Pysics. vol. 98 (Wiley, 1997).

13. D. Fiorani & G. Sberveglieri. Fundamental Properties of Nanostructured Materials. (WORLD SCIENTIFIC, 1994).

14. Giri, A. K., Kirkpatrick, E. M., Moongkhamklang, P., Majetich, S. A. & Harris, V. G. Photomagnetism and structure in cobalt ferrite nanoparticles. Appl. Phys. Lett. 80, 2341–2343 (2002).

15. Imine, S., Schoenstein, F., Mercone, S., Zaghrioui, M., Bettahar, N. & Jouini, N. Bottom-up and new compaction processes: A way to tunable properties of nanostructured cobalt ferrite ceramics. J. Eur. Ceram. Soc. 31, 2943–2955 (2011).

16. Wagner, W., Van Swygenhoven, H., Höfler, H. J. & Wiedenmann, A. Microstructure and magnetic correlations in nanostructured Fe and Ni, studied by small angle neutron scattering. Nanostructured Mater. 6, 929–932 (1995).

17. Bellino, M. G., Lamas, D. G. & Walsöe de Reca, N. E. A Mechanism for the Fast Ionic Transport in Nanostructured Oxide-Ion Solid Electrolytes. Adv. Mater. 18, 3005–3009 (2006).

18. Guo, Y.-G., Hu, J.-S. & Wan, L.-J. Nanostructured Materials for Electrochemical Energy Conversion and Storage Devices. Adv. Mater. 20, 2878–2887 (2008).

19. Maier, J. Nano-Ionics: Trivial and Non-Trivial Size Effects on Ion Conduction in Solids. Z. Für Phys. Chem. 217, 415–436 (2003).

20. Maier, J. Nanoionics: ion transport and electrochemical storage in confined systems. Nat. Mater. 4, 805–815 (2005).

21. Iwahara, H., Esaka, T., Uchida, H. & Maeda, N. Proton conduction in sintered oxides and its application to steam electrolysis for hydrogen production. Solid State Ion. 3–4, 359–363 (1981).

22. Xia, C., Qiao, Z., Feng, C., Kim, J-S., Wang, B. & Zhu, B. Study on Zinc Oxide-Based Electrolytes in Low-Temperature Solid Oxide Fuel Cells. Materials 11, 40 (2017).

23. Zhang, X., Qiu, Y., Jin, F., Guo, F., Song, Y. & Zhu, B. A highly active anode functional layer for solid oxide fuel cells based on proton-conducting electrolyte $BaZr_{0.1}Ce_{0.7}Y_{0.2}O_{3-\delta}$. J. Power Sources 241, 654–659 (2013).

24. Norby, T. Solid-state protonic conductors: principles, properties, progress and prospects. Solid State Ion. 125, 1–11 (1999).

25. Stub, S. Ø., Vøllestad, E. & Norby, T. Mechanisms of Protonic Surface Transport in Porous Oxides: Example of YSZ. *J. Phys. Chem. C* **121**, 12817–12 (2017).

26. Sides, C. R., Li, N., Patrissi, C. J., Scrosati, B. & Martin, C. R. Nanoscale Materials for Lithium-Ion Batteries. MRS Bull. 27, 604–607 (2002).

27. Wang, Y. & Cao, G. Developments in Nanostructured Cathode Materials for High-Performance Lithium-Ion Batteries. Adv. Mater. 20, 2251–2269 (2008).

28. Ellis, B., Subramanya Herle, P., Rho, Y. H., Nazar, L. F., Dunlap, R., Perry, L. K. & Ryan, D. H. Nanostructured materials for lithium-ion batteries: Surface conductivity vs. bulk ion/electron transport. Faraday Discuss 134, 119–141 (2007).

29. Skundin, A. M. The Problem of Carbon Nanotubes Using in Lithium-Ion Batteries. in Carbon Nanomaterials in Clean Energy Hydrogen Systems (eds. Baranowski, B., Zaginaichenko, S. Yu., Schur, D. V., Skorokhod, V. V. & Veziroglu, A.) 285–290 (Springer Netherlands, 2009).

30. Li, N., Martin, C. R. & Scrosati, B. Nanomaterial-based Li-ion battery electrodes. J. Power Sources 97–98, 240–243 (2001).

31. Curtis, C. J., Wang, J. & Schulz, D. L. Preparation and Characterization of LiMn2O4 Spinel Nanoparticles as Cathode Materials in Secondary Li Batteries. J. Electrochem. Soc. 151, A590 (2004).

32. Jamnik, J. & Maier, J. Nanocrystallinity effects in lithium battery materials. Phys. Chem. Chem. Phys. 5, 5215 (2003).

33. Suarez, M., Fernández, A., Menéndez, J. L., Torrecillas, R., Kessel, H. U., Hennicke, J., Kirchner, R. & Kessel, T. Challenges and Opportunities for Spark Plasma Sintering: A Key Technology for a New Generation of Materials. in Sintering Applications (ed. Ertug, B.) (InTech, 2013).

34. Michele Petrecca. Soft ferrites magnetic nanoparticles: a new strategy to improve the performance of high frequency electronic devices. (2016).

35. Chen, D.-X., Pardo, E. & Sanchez, A. Fluxmetric and magnetometric demagnetizing factors for cylinders. J. Magn. Magn. Mater. 306, 135–146 (2006).

36. McCurrie, R. A. The structure and properties of alnico permanent magnet alloys. Handbook of Ferromagnetic Materials. 3, 107-118 (1982).

37. Koehler, W. C. Magnetic Properties of Rare-Earth Metals and Alloys. J. Appl. Phys. 36, 1078–1087 (1965).

38. Elliott, R. Magnetic Properties of Rare Earth Metals. (Springer Science & Business Media, 2013).

39. Sagawa, M., Fujimura, S., Yamamoto, H. & Hiraga, K. Permanent magnet materials based on the rare earth-iron-boron tetragonal compounds. IEEE Transactions on Magnetics. 20, 1584-1589 (1984).

40. Massari, S. & Ruberti, M. Rare earth elements as critical raw materials: Focus on international markets and future strategies. Resour. Policy 38, 36–43 (2013).

41. Moriarty, P. Nanostructured materials. Rep. Prog. Phys. 64, 297 (2001).

42. Cain, M. & Morrell, R. Nanostructured ceramics: a review of their potential. Appl. Organomet. Chem. 15, 321–330 (2001).

43. Trohidou, K. N. Magnetic Nanoparticle Assemblies. (CRC Press, 2014).

44. Mathew, D. S. & Juang, R.-S. An overview of the structure and magnetism of spinel ferrite nanoparticles and their synthesis in microemulsions. Chem. Eng. J. 129, 51–65 (2007).

45. Pacakova, B., Kubickova, S., Reznickova, A., Niznansky, D. & Vejpravova, J. Spinel Ferrite Nanoparticles: Correlation of Structure and Magnetism. Magn. Spinels - Synth. Prop. Appl. (2017).

46. Carta, D., Casula, M. F., Falqui, A., Loche, D., Mountjoy, G., Sangregorio, C. & Corrias, A. A Structural and Magnetic Investigation of the Inversion Degree in Ferrite Nanocrystals MFe_2O_4 (M = Mn, Co, Ni). J. Phys. Chem. C 113, 8606–8615 (2009).

47. Verwey, E. J. W. & Heilmann, E. L. Physical Properties and Cation Arrangement of Oxides with Spinel Structures I. Cation Arrangement in Spinels. J. Chem. Phys. 15, 174–180 (1947).

48. Pulišová, P., Kováč, J., Voigt, A. & Raschman, P. Structure and magnetic properties of Co and Ni nano-ferrites prepared by a two step direct microemulsions synthesis. J. Magn. Magn. Mater. 341, 93–99 (2013).

49. Rondinone, A. J., Samia, A. C. S. & Zhang, Z. J. Superparamagnetic Relaxation and Magnetic Anisotropy

    Energy Distribution in CoFe2O4 Spinel Ferrite Nanocrystallites. J. Phys. Chem. B 103, 6876–6880 (1999).

50. Baldi, G., Bonacchi, D., Innocenti, C., Lorenzi, G. & Sangregorio, C. Cobalt ferrite nanoparticles: The

    control of the particle size and surface state and their effects on magnetic properties. J. Magn. Magn.

    Mater. 311, 10–16 (2007).

51. Li, D., Wang, F., Xia, A., Zhang, L., Li, T., Jin, C. & Liu, X. A facile way to realize exchange coupling

    interaction in hard/soft magnetic composites. J. Magn. Magn. Mater. 417, 355–358 (2016).

52. Joshi, H. M., Lin, J. P., Aslam, M., Prasad, P. V., Schulz-Sikma, E. A., Edelman, R, Meade, T. & Dravid, V. P.

    Effects of Shape and Size of Cobalt Ferrite Nanostructures on Their MRI Contrast and Thermal Activation.

    J. Phys. Chem. C 113, 17761–17767 (2009).

53. Ayyappan, S., Panneerselvam, G., Antony, M. P. & Philip, J. High temperature stability of surfactant

    capped CoFe2O4 nanoparticles. Mater. Chem. Phys. 130, 1300–1306 (2011).

54. Ayyappan, S., Paneerselvam, G., Antony, M. P. & Philip, J. Structural stability of ZnFe2O4 nanoparticles

    under different annealing conditions. Mater. Chem. Phys. 128, 400–404 (2011).

55. Jang, J-I, Yoo, H.-I., Phase stability and ionic transference number of a ferrite spinel,

    Mn0.54Zn0.35Fe2.11O4. Solid State Ion. 84, 77-88 (1996).

56. Nazario, E., Herrasti, P., Morales, M. P. & Menéndez, N. Synthesis and characterization of CoFe2O4

    ferrite nanoparticles obtained by an electrochemical method. Nanotechnology 23, 355708 (2012).

57. Kim, S., Kim, D. & Lee, C. S. On the conduction pathway for protons in nanocrystalline yttria-stabilized

    zirconia. Phys. Chem. Chem. Phys. 11, 3035–3038 (2009).

58. Cernea, M., Galizia, P., Ciuchi, I. -V., Aldica, G., Mihalache, V., Diamandescu & L. CoFe2O4 magnetic

    ceramic derived from gel and densified by spark plasma sintering. J. Alloys Compd. 656, 854–862 (2016).

59. Imine, S., Shoenstein, F., Mercone, S., Zaghrioui, M., Bettahar, N. & Jouini, N. Bottom-up and new

    compaction processes: A way to tunable properties of nanostructured cobalt ferrite ceramics. J. Eur.

    Ceram. Soc. 31, 2943–2955 (2011).

60. Aubert, A., Loyau, V., Mazaleyrat, F. & LoBue, M. Uniaxial anisotropy and enhanced magnetostriction of $CoFe_2O_4$ induced by reaction under uniaxial pressure with SPS. J. Eur. Ceram. Soc. 37, 3101–3105 (2017).

61. Millot, N., Le Gallet, S., Aymes, D., Bernard, F. & Grin, Y. Spark plasma sintering of cobalt ferrite nanopowders prepared by coprecipitation and hydrothermal synthesis. J. Eur. Ceram. Soc. 27, 921–926 (2007).

62. Wu, L. N., Jiang, L. Z. & Hong, F. Y. Dielectric and Magnetic Properties of Sintered Cobalt Ferrite Derived from Nanocrystalline Powders. Adv. Mater. Res. 476–478, 726–729 (2012).

63. Munir, Z. A., Anselmi-Tamburini, U. & Ohyanagi, M. The effect of electric field and pressure on the synthesis and consolidation of materials: A review of the spark plasma sintering method. J. Mater. Sci. 41, 763–777 (2006).

64. Maglia, F., Tredici, I. G. & Anselmi-Tamburini, U. Densification and properties of bulk nanocrystalline functional ceramics with grain size below 50nm. J. Eur. Ceram. Soc. 33, 1045–1066 (2013).

65. Anselmi-Tamburini, U., Garay, J. E. & Munir, Z. A. Fast low-temperature consolidation of bulk nanometric ceramic materials. Scr. Mater. 54, 823–828 (2006).

66. Song, Q. & Zhang, Z. J. Shape Control and Associated Magnetic Properties of Spinel Cobalt Ferrite Nanocrystals. J. Am. Chem. Soc. 126, 6164–6168 (2004).

67. Lu, L. T., Dung, N. T., Tung ì, L. D., Thanh C. T., Qui, O. K., Chuck, N. V., Maenosono, S. & Thanh, N. T. K. et al. Synthesis of magnetic cobalt ferrite nanoparticles with controlled morphology, monodispersity and composition: the influence of solvent, surfactant, reductant and synthetic conditions. Nanoscale 7, 19596–19610 (2015).

68. Cullity, B. D. & Graham, C. D. Introduction to Magnetic Materials. (John Wiley & Sons, 2011).

69. Toksha, B. G., Shirsath, S. E., Patange, S. M. & Jadhav, K. M. Structural investigations and magnetic properties of cobalt ferrite nanoparticles prepared by sol–gel auto combustion method. Solid State Commun. 147, 479–483 (2008).

70. Maaz, K., Mumtaz, A., Hasanain, S. K. & Ceylan, A. Synthesis and magnetic properties of cobalt ferrite ($CoFe_2O_4$) nanoparticles prepared by wet chemical route. J. Magn. Magn. Mater. 308, 289–295 (2007).

71. Fariñas, J. C., Moreno, R., Pèrez, A., Garcìa, M. A., Garcìa-Hernàndez, M., Salvador, M. D. & Borrell, A. et al. Microwave-assisted solution synthesis, microwave sintering and magnetic properties of cobalt ferrite. J. Eur. Ceram. Soc. 38, 2360–2368 (2018).

72. Wang, Y., Chen, K. S., Mishler, J., Cho, S. C. & Adroher, X. C. A review of polymer electrolyte membrane fuel cells: Technology, applications, and needs on fundamental research. Appl. Energy 88, 981–1007 (2011).

73. Anselmi-Tamburini, U., Maglia, F., Chiodelli, G., Riello, P., Bucella, S. & Munir, Z. A. Enhanced low-temperature protonic conductivity in fully dense nanometric cubic zirconia. Appl. Phys. Lett. 89, 163116 (2006).

74. Traversa, E., Gur, T., Kreller, C. & Thangadurai, V. Ionic Conducting Oxide Thin Films. (The Electrochemical Society, 2015).

75. Maglia, F., Tredici, I. G., Spinolo, G. & Anselmi-Tamburini, U. Low temperature proton conduction in bulk nanometric TiO2 prepared by high-pressure field assisted sintering. J. Mater. Res. 27, 1975–1981 (2012).

76. Tredici, I. G., Maglia, F., Ferrara, C., Mustarelli, P. & Anselmi-Tamburini, U. Mechanism of Low-Temperature Protonic Conductivity in Bulk, High-Density, Nanometric Titanium Oxide. Adv. Funct. Mater. 24, 5137–5146 (2014).

77. Colomer, M. T. Nanoporous Anatase Thin Films as Fast Proton-Conducting Materials. Adv. Mater. 18, 371–374 (2006).

78. Scherrer, B., Schlupp, M. V. F., Stender, D., Wildenhues, J., Grolig, J. G., Ma, H., Kocher, P., Prestat, M., Lippert, T. & Gauckler, L. J. On Proton Conductivity in Porous and Dense Yttria Stabilized Zirconia at Low Temperature. Adv. Funct. Mater. 23, 1957–1964 (2013).

79. Shirpour, M., Gregori, G., Merkle, R. & Maier, J. On the proton conductivity in pure and gadolinium doped nanocrystalline cerium oxide. Phys. Chem. Chem. Phys. 13, 937–940 (2010).

80. Meng, Y., Gao, J., Zhao, Z., Amoroso, J., Tong, J., & Brinkman K. S. Review: recent progress in low-temperature proton-conducting ceramics. J. Mater. Sci. 54, 9291–9312 (2019).

81. Dawson, J. A. & Tanaka, I. Significant Reduction in Hydration Energy for Yttria Stabilized Zirconia Grain Boundaries and the Consequences for Proton Conduction. Langmuir 30, 10456–10464 (2014).

82. Tominaka, S., Akiyama, N., Croce, F., Momma, T., Scrosati, B. & Osaka, T. Sulfated zirconia nanoparticles as a proton conductor for fuel cell electrodes. J. Power Sources 185, 656–663 (2008).

83. Tandé, C., Pérez-Coll, D. & Mather, G. C. Surface proton conductivity of dense nanocrystalline YSZ. J. Mater. Chem. 22, 11208–11213 (2012).

84. Kim, S., Anselmi-Tamburini, U., Park, H. J., Martin, M. & Munir, Z. A. Unprecedented Room-Temperature Electrical Power Generation Using Nanoscale Fluorite-Structured Oxide Electrolytes. Adv. Mater. 20, 556–559 (2008).

85. Stub, S. Ø., Vøllestad, E. & Norby, T. Mechanisms of Protonic Surface Transport in Porous Oxides: Example of YSZ. J. Phys. Chem. C 121, 12817–12825 (2017).

86. Sato, R., Ohkuma, S., Shibuta, Y., Shimojo, F. & Yamaguchi, S. Proton Migration on Hydrated Surface of Cubic ZrO_2 : Ab initio Molecular Dynamics Simulation. J. Phys. Chem. C 119, 28925–28933 (2015).

87. Scherrer, B., Schlupp, M. V. F., Stender, D., Wildenhues, J., Grolig, J. G., Ma, H., Kocher, P., Prestat, M., Lippert, T. & Gauckler, L. J. On Proton Conductivity in Porous and Dense Yttria Stabilized Zirconia at Low Temperature. Adv. Funct. Mater. 23, 1957–1964 (2013).

88. Agosta, L., Brandt, E. G. & Lyubartsev, A. P. Diffusion and reaction pathways of water near fully hydrated TiO2 surfaces from ab initio molecular dynamics. J. Chem. Phys. 2, 147 (2017)

89. Giffin, G. A., Piga, M., Lavina, S., Navarra, M. A., D'Epifanio, A., Scrosati, B. & Di Noto V. Characterization of sulfated-zirconia/Nafion® composite membranes for proton exchange membrane fuel cells. J. Power Sources 198, 66–75 (2012).

90. Herring, A. M. Inorganic–Polymer Composite Membranes for Proton Exchange Membrane Fuel Cells. J. Macromol. Sci. Part C 46, 245–296 (2006).

91. Matos, B. R. et al. Thermal properties of Nafion–TiO2 composite electrolytes for PEM fuel cell. J. Therm. Anal. Calorim. 97, 591 (2009).

92. Tomaszewski, P. E. Structural phase transitions in crystals. I. Database. Phase Transit. 38, 127–220 (1992).

93. Pârvulescu, V., Coman, S., Grange, P. & Pârvulescu, V. I. Preparation and characterization of sulfated zirconia catalysts obtained via various procedures. Appl. Catal. Gen. 176, 27–43 (1999).

94. Faˌrcasˌiu, D., Li, J. Q. & Cameron, S. Preparation of sulfated zirconia catalysts with improved control of sulfur content II. Effect of sulfur content on physical properties and catalytic activity. Appl. Catal. Gen. 154, 173–184 (1997).

95. Sun, Y., Ma, S., Du, Y., Yuan, L., Wang, S., Yang, J., Deng, F., Xiao & F.-S. Solvent-Free Preparation of Nanosized Sulfated Zirconia with Brønsted Acidic Sites from a Simple Calcination. J. Phys. Chem. B 109, 2567–2572 (2005).

96. C. Morterra, F.Pinna & M.Signoretto. Journal of catalysis. Crystal Phase, Spectral Features, and Catalytic Activity of Sulfated-doped Zirconia Systems 109–123 (1995).

97. Yadav, G. D. & Nair, J. J. Sulfated zirconia and its modified versions as promising catalysts for industrial processes. Microporous Mesoporous Mater. 33, 1–48 (1999).

98. Peighambardoust, S. J., Rowshanzamir, S. & Amjadi, M. Review of the proton exchange membranes for fuel cell applications. Int. J. Hydrog. Energy 35, 9349–9384 (2010).

99. Chen, H., Cong, T., N., Yang, W., Tan, C., Li, Y. & Ding, Y. Progress in electrical energy storage system: A critical review. Prog. Nat. Sci. 19, 291–312 (2009).

100. Salameh, Z. M., Casacca, M. A. & Lynch, W. A. A mathematical model for lead-acid batteries. IEEE Trans. Energy Convers. 7, 93–98 (1992).

101. McDowall, J. Conventional battery technologies-present and future. in 2000 Power Engineering Society Summer Meeting (Cat. No.00CH37134) vol. 3 1538–1540 (IEEE, 2000).

102. Powers, R. A. Batteries for low power electronics. Proc. IEEE 83, 687–693 (1995).

103. Shen, Y. & Kordesch, K. The mechanism of capacity fade of rechargeable alkaline manganese dioxide zinc cells. 5 (2000).

104. Mundra, T. & Kumar, A. An Innovative Battery Charger for Safe Charging of NiMH/NiCd Batteries. IEEE Trans. Consum. Electron. 53, 1044–1052 (2007).

105. Feng, F. Electrochemical behaviour of intermetallic-based metal hydrides used in Ni/metal hydride (MH) batteries: a review. Int. J. Hydrog. Energy 26, 725–734 (2001).

106. Zubi, G., Dufo-López, R., Carvalho, M. & Pasaoglu, G. The lithium-ion battery: State of the art and future perspectives. Renew. Sustain. Energy Rev. 89, 292–308 (2018).

107. Chayambuka, K., Mulder, G., Danilov, D. L. & Notten, P. H. L. Sodium-Ion Battery Materials and Electrochemical Properties Reviewed. Adv. Energy Mater. 8, 1800079 (2018).

108. Kim, H., Kim, J. C., Bianchini, M., Seo, D.-H., Rodriguez-Garcia, J. & Ceder, G. Recent Progress and Perspective in Electrode Materials for K-Ion Batteries. Adv. Energy Mater. 8, 1702384 (2018).

109. Tarascon, J.-M. & Armand, M. Issues and challenges facing rechargeable lithium batteries. Nature 414, 359–367 (2001).

110. Bazito, F. F. C. & Torresi, R. M. Cathodes for lithium ion batteries: the benefits of using nanostructured materials. J. Braz. Chem. Soc. 17, 627–642 (2006).

111. Scrosati, B. Recent advances in lithium ion battery materials. Electrochimica Acta 45, 2461–2466 (2000).

112. Myung, S.-T., Komaba, S. & Kumagai, N. Enhanced Structural Stability and Cyclability of Al-Doped $LiMn_2O_4$ Spinel Synthesized by the Emulsion Drying Method. J. Electrochem. Soc. 148, A482 (2001).

113. Nakayama, M., Kaneko, M., Uchimoto, Y., Wakihara, M. & Kawamura, K. Molecular Dynamics Simulations of LiCoyMn2-yO4 Cathode Materials for Rechargeable Li Ion Batteries. J. Phys. Chem. B. 108, 3754–3759 (2004)

114. Lee, J. H., Hong, J. K. & Jang, D. H. Degradation mechanisms in doped spinels of LiM0.05Mn1.95O4 (M=Li, B, Al, Co, and Ni) for Li secondary batteries. 8, 7-14 (2000).

115. Amine, K., Tukamoto, H., Yasuda, H. & Fujita, Y. Preparation and electrochemical investigation of $LiMn_{2-x}Me_xO_4$ (Me: Ni, Fe, and x = 0.5, 1) cathode materials for secondary lithium batteries. J. Power Sources 68, 604–608 (1997).

116. Banov, B., Todorov, Y., Trifonova, A., Momchilov, A. & Manev, V. LiMn2 − xCoxO4 cathode with enhanced cyclability. J. Power Sources 68, 578–581 (1997).

117. Mokhtar, N. & Idris, N. H. Comparison on Electrochemical Performances of LiNi0.5Mn1.5O4 Cathode Materials Synthesized Using Different Precursors. Mater. Today Proc. 3, 129–135 (2016).

118. Bérardan, D., Franger, S., Meena, A. K. & Dragoe, N. Room temperature lithium superionic conductivity in high entropy oxides. J. Mater. Chem. A 4, 9536–9541 (2016).

119. Dąbrowa, J., Stygar, M., Mikuła, A., Knapik, A., Mroczka, K., Tejchman, W., Marek, D. & Martin, M. Synthesis and microstructure of the (Co,Cr,Fe,Mn,Ni)3O4 high entropy oxide characterized by spinel structure. Mater. Lett. 216, 32–36 (2018).

120. Djenadic, R., Sarkar, A., Clemens, O., Loho, C., Botros, M. & Chakravadhanula, V. S. K. Multicomponent equiatomic rare earth oxides. Mater. Res. Lett. 5, 102–109 (2017).

121. Gild, J., Samiee, M., Braun, J. L., Harrington, T., Vega, H., Hopkins, P. E., Vecchio, K. & Luo, J. High-entropy fluorite oxides. J. Eur. Ceram. Soc. 38, 3578–3584 (2018).

122. Jiang, S., Hu, T., Gild, J., Zhou, N., Nie, J., Qin, M., Harrington, T., Vecchio, K. & Luo, J. A new class of high-entropy perovskite oxides. Scr. Mater. 142, 116–120 (2018).

123. Oses, C., Toher, C. & Curtarolo, S. High-entropy ceramics. Nat. Rev. Mater. 5, 295–309 (2020).

124. Rost, C. M., Sachet, E., Borman, T., Moballegh, A., Dickey, E. C., Hou, D., Jones, J. L., Curtarolo, S. & Maria, J. P. Entropy-stabilized oxides. Nat. Commun. 6, (2015).

125. Sarkar, A., Djenadic, R, Nandhini, J. U., Sanghvi K. P., Chakravadhanula, V. S. K., Gandhi, A. S., Hahn, H. & Bhattacharya, S. Nanocrystalline multicomponent entropy stabilized transition metal oxides. J. Eur. Ceram. Soc. 37, 747–754 (2017).

126. Sarkar, A., Djenadic, R., Wang, D., Hein, C., Kautenburger, R., Clemens, O. & Hahn, H. Rare earth and transition metal based entropy stabilized perovskite type oxides. J. Eur. Ceram. Soc. 38, 2318–2327 (2018).

127. Sarkar, A., Velasco, L., Wang, D., Wang, Q., Talasila, G., De Biasi, L., Kübel, C., Brezesinski, T., Bhattacharya, S. S., Hahn, H. & Breitung, B. High entropy oxides for reversible energy storage. Nat. Commun. 9, (2018).

128. Yan, X., Constantin, L., Lu, Y., Silvain, J.-F., Nastasi, M. & Cui, B. $(Hf_{0.2}Zr_{0.2}Ta_{0.2}Nb_{0.2}Ti_{0.2})C$ high-entropy ceramics with low thermal conductivity. J. Am. Ceram. Soc. 101, 4486–4491 (2018).

129. Ishizawa, N. & Tateishi, K. Diffusion of Li atoms in LiMn2O4 - A structural point of view -. J. Ceram. Soc. Jpn. 117, 6–14 (2009).

130. Pechini, M. P. Method of preparing lead and alkaline earth titanates and niobates and coating method using the same to form a capacitor. (1967).

131. H. Takeda & Y. Kudoh. Physica B and C. in vol. 139 333–336 (1986).

132. J. Delville & C. Legrand. Golden book of phase transitions. vol. 1 (Wroclaw, 2002).

133. Coduri, M., Masala, P., Allieta, M., Peral, I., Brunelli, M., Biffi, C. A. & Scavini, M. Phase transformations in the CeO2 - Sm2O3 system: a multiscale powder diffraction investigation. Inorg. Chem. 57, 879-891 (2018)

134. Lamas, D. G., Rosso, A. M., Anzorena, M. S., Fernández, A., Bellino, M. G., Cabezas, M. D., Walsöe de Reca, N. E. & Craievich, A. F. Crystal structure of pure ZrO2 nanopowders. Scr. Mater. 55, 553–556 (2006).

135. K. Tao, K.-M Liang, Y.-Q Guo & D.-N Wang. Phase Transition. in vol. 38 127–220 (1992).

136. Bouvier, P., Djurado, E., Lucazeau, G. & Le Bihan, T. High-pressure structural evolution of undoped tetragonal nanocrystalline zirconia. Phys. Rev. B 62, 8731–8737 (2000).

137. Akimoto, J., Takahashi, Y., Gotoh, Y. & Mizuta, S. Single crystal growth of the spinel-type LiMn2O4. J. Cryst. Growth 229, 405–408 (2001).

138. Shannon, R. D. Revised Effective Ionic Radii and Systematic Studies of Interatomic Distances in Halides and Chaleogenides. Acta Crystallographica A 751–767 (1976).

139. Smith, W. F., Hashemi, J. Materiali magnetici dolci in Scienza e Tecnologia dei Materiali. (McGraw-Hill Education 2016).

140. Munir, Z. A., Anselmi-Tamburini, U. & Ohyanagi, M. The effect of electric field and pressure on the synthesis and consolidation of materials: A review of the spark plasma sintering method. J. Mater. Sci. 41, 763–777 (2006).

141. http://cisric.unipv.it/.

142. Zhang, T., Li, D., Tao, Z. & Chen, J. Understanding electrode materials of rechargeable lithium batteries via DFT calculations. Prog. Nat. Sci. Mater. Int. 23, 256–272 (2013).